Master's thesis

NTNU
Norwegian University of Science and Technology
Faculty of Natural Sciences
Department of Physics

Ida Cathrine Skogvoll

Tunable anisotropic quantum Rabi model via magnon|spin-qubit ensemble

Master's thesis in Nanotechnology
Supervisor: Akashdeep Kamra
Co-supervisor: Jeroen Danon
June 2021

NTNU
Norwegian University of
Science and Technology

Ida Cathrine Skogvoll

Tunable anisotropic quantum Rabi model via magnon|spin-qubit ensemble

Master's thesis in Nanotechnology
Supervisor: Akashdeep Kamra
Co-supervisor: Jeroen Danon
June 2021

Norwegian University of Science and Technology
Faculty of Natural Sciences
Department of Physics

NTNU
Norwegian University of
Science and Technology

Preface

This master's thesis concludes a 5-year Master's Degree Programme in Nanotechnology at the Norwegian University of Science and Technology (NTNU), specializing in nanoelectronics. The work was conducted from January to June of this year, at the Center for Quantum Spintronics (QuSpin) in the Department of Physics.

I would like to express my deepest gratitude to my supervisors, Akashdeep Kamra and Jeroen Danon. Thank you for the opportunity to be a part of this project, for your patience and for the invaluable discussions and feedback during our meetings. I also wish to especially thank Akashdeep Kamra for always taking the time out of a busy schedule to help me, providing your insights not only on this particular project but also on life in general. Thank you for always encouraging me whenever I needed some extra motivation. Thank you to Jonas Lidal for never failing to answer my seemingly endless amount of questions.

This thesis work builds on a specialization project performed in the previous fall semester of 2020, concerning the theoretical and numerical study of the quantum Rabi model in various parameter regimes. As a result, parts of chapters 1 and 2 have been revised and reused with modifications. The work also involved a great deal of programming for the numerical analysis of the anisotropic quantum Rabi model, using Python and the Quantum Toolbox in Python library (QuTiP). The programs employed in the numerical calculations have not been appended herewith, but are available on reasonable request.

The work carried out as part of this thesis led to a research article authored by Ida C. Skogvoll, Jonas Lidal, Jeroen Danon and Akashdeep Kamra. This is under review at the time of this writing and the manuscript and supplemental materials can be found in appendices A and B.

Ida Cathrine Skogvoll
Trondheim, June 23, 2021

Abstract

The ongoing evolution in the field of quantum information technologies faces a multitude of challenges in developing platforms for the realization of quantum computation and communication. It is contingent on implementing qubit systems designed for highly specific tasks, while addressing such critical issues as decoherence, error-correction and state manipulation. In addition, these systems need to still be successfully scaled up into large quantum circuits. Several qubit platforms have been realized thus far, where each physical realization has its distinct advantages and disadvantages. The current progress in quantum information therefore relies on designing new hybrid platforms, engineered to combine the desired elements of each respective discipline.

The aim of this thesis is to provide a detailed description of such a hybrid platform, with the objective of addressing the challenges encountered by emerging quantum technologies. The hybrid platform in question is a ferromagnet exchange-coupled to a spin-qubit, which properties can be described in terms of the paradigmatic quantum Rabi model (QRM). This model describes the light-matter interaction between any two-level system and a bosonic mode and in this study, the two-level system will be embodied by the spin-qubit, while the ferromagnetic normal modes will act as the bosonic mode.

Through our investigation, we find that the ensuing magnon|spin-qubit ensemble exhibits various novel features that make it a promising platform for addressing some of the challenges mentioned above. It is shown that with an isotropic ferromagnet, the system realizes an ideal Jaynes-Cummings model, where the excitation number non-conserving counter-rotating terms are forbidden. Alternatively, when anisotropy is introduced into the magnet, the ferromagnetic normal mode is that of a magnon with a controllable degree of intrinsic squeezing. The squeezed magnon yields non-zero counter-rotating terms, where the coupling strengths for excitation number conserving and non-conserving terms can be individually tuned. Furthermore, this leads to a considerable coupling enhancement without requiring a non-equilibrium drive. Considering the case of three spin-qubits, we demonstrate the simultaneous resonant excitation of these qubits by a single squeezed magnon mode. This shows that our platform enables robust generation of the Greenberger-Horne-Zeilinger (GHZ) states of Shor's error correction code. The magnon|spin-qubit ensemble is therefore an optimal platform for the implementation of fault-tolerant quantum computing protocols.

Sammendrag

Den pågående utviklingen innenfor kvanteinformasjonteknologi står ovenfor en rekke utfordringer i forbindelse med å konstruere fysiske plattformer som vil kunne være med på å realisere kvanteberegning og kvantekommunikasjon. Utviklingen er blant annet fullstendig avhengig av implementering av kvantebit-systemer spesielt designet for høyst spesifikke oppgaver, samtidig som disse må adressere kritiske problemer som dekoherens, feilkorrigering og manipulering av kvantetilstander. Flere ulike kvantebit-systemer har blitt foreslått så langt, hvor hver fysiske realisering har sine fordeler og ulemper. Fremgangen i kvanteinformasjon belager seg derfor på utvikling av nye hybridplattformer som kombinerer de ønskede egenskapene fra hver respektive disiplin.

Formålet med denne mastergradsavhandlingen er å utarbeide en detaljert teoretisk beskrivelse av et slikt hybridsystem, med sikte på å ta for seg utfordringene som ny kvanteteknologi står ovenfor. Denne hybridplattformen består av en ferromagnet som vekselvirker med en spinnkvantebit, hvis egenskaper kan beskrives av den paradigmatiske kvantemekaniske Rabi-modellen. Denne modellen beskriver interaksjonen mellom et to-nivå system og en harmonisk oscillator, og i denne avhandlingen vil kvantebiten representere to-nivå systemet og de ferromagnetiske egentilstandene representerer bosontilstanden.

Det blir funnet at det påfølgende magnon|kvantebit-systemet utviser flere unike egenskaper som gjør det til en lovende plattform for å takle noen av utfordringene nevnt ovenfor. Vi viser at for en isotropisk ferromagnet realiserer systemet en ideell Jaynes-Cummings modell, hvor overganger som ikke bevarer det totale antallet eksitasjoner er forbudt. Alternativt, når vi introduserer anisotropi i ferromagneten, så viser det seg at egentilstandene er magnoner med redusert kvantestøy og at styrken for eksitasjonsbevarende og ikke-eksitasjonsbevarende overganger kan kontrolleres individuelt. Dette medfører og en forsterket interaksjonsstyrke, som er en grunnleggende effekt med opprinnelse i Heisenbergs usikkerhetsrelasjon. Ved å analysere tilfellet for tre kvantebits i stedet for en, viser vi at systemet muliggjør robust generasjon av sammenfiltrede GHZ tilstander for implementasjon av Shors feilkorrigerende kode for kvanteberegning, gjennom reversible Rabi-svingninger.

Table of Contents

List of Figures

1 Introduction

One of the most fundamental and omnipresent physical phenomena in nature is the interaction between light and matter. In quantum systems this involves the complex interplay of charged particles and photons, of which character may only be captured by approximative physical models. Arguably one of the most elementary ways of modelling light-matter interaction is through a two-level system coupled coherently to a single-mode quantum field. This is known as the quantum Rabi model (QRM), the quantized version of its semi-classical counterpart, developed by I. I. Rabi in the middle of the 1930's [1, 2]. The two-level system is a standard approximation for any system that can be interpreted as a dichotomic quantity, such as electron spin pointing up or down and horizontal or vertical polarization of light [3]. This approximation is also widely used when the dynamics are limited to two energy levels in an artificial or natural atom. The essence of the physical system is kept, while rendering it analytically tractable [4]. Despite its simplicity the QRM has far reaching implications and accurately describes the static and dynamical behavior of physical systems in a wide range of fields, such as quantum optics and condensed matter [5]. It has garnered a major focus both in theoretical and experimental studies over the past several decades, with its integrability recently discovered by D. Braak [6].

Historically, the investigation of manipulating matter by light began within the field of cavity quantum electrodynamics, the study of atoms coupled to a limited number of electromagnetic field modes. This is achieved by placing an effectively two-level system in a resonant microwave cavity [7]. The degree of control one has in manipulating the state of the two-level system is governed by the coupling strength of the interaction, and the main driving force behind cavity quantum electrodynamics and related fields has therefore been the technological developments towards attaining higher coupling regimes. Cavity quantum electrodynamics was initially constrained by coupling strengths smaller than the decay rates of the cavity and the two-level system, leading to spontaneous emission events and thus ultimately destroying any coherent phenomena [4]. Nonetheless, it experienced a fresh impetus when reaching the strong-coupling (SC) regime, where the coupling strength is larger than any decoherence rates. This results in the reversible and coherent exchange of single photons through so-called Rabi oscillations, allowing for a high degree of precision in preparing and manipulating quantum states.

In recent years, coupling strengths that are a significant fraction of the natural frequencies of the system have been reached. When the interaction between the two-level system and the cavity is this strongly coupled, the number of excitations is not conserved and virtual transitions give rise to novel phenomena not present in the SC regime, for instance strongly entangled and non-classical eigenstates [8]. Such an ultra-strong coupling has been successfully implemented in various solid-state systems where the artificial atom is embedded in the resonator medium, including superconducting flux qubits [9–13], semiconductor quantum wells [14] and trapped ions setups [15]. A property

of the ultra-strong coupling (USC) regime under recent investigation is that by tuning the frequency of the two-level system one achieves higher-order resonant transitions, stemming from the non-conserving nature of transitions in this regime. This enables coherent and reversible Rabi-type multi-photon exchanges between states with a different number of excitations [16–18].

A field of research where the QRM has sparked a surging interest during the past years, is in quantum information theory. This is naturally because the building block of quantum information is a two-level system, the quantum bit, the levels represented by the states $|0\rangle$ and $|1\rangle$. No matter what kind of physical representation a qubit has, the light-matter interaction described by the QRM addresses how one might prepare, manipulate and measure the state of a qubit interacting with a quantum field [19]. Thus, the current revolution in quantum information and other novel quantum technologies capitalizes heavily on both the detailed theoretical understanding of the QRM and of its physical realization, in higher coupling regimes [20, 21]. The QRM plays a key role in implementing protocols essential to the realization of quantum computing, for instance in ultra-fast gate operations, quantum error correction and remote entanglement [10, 22–24]. In these applications, it is particularly important to achieve a high coupling strength both for high fidelity response, faster gate operations and a high level of state controllability, racing against imminent decoherence of fragile qubit states. Several schemes for coupling enhancement have been proposed so far, for instance methods featuring modulation by periodic driving fields [25, 26].

The successful realization of quantum computing is contingent on addressing a multitude of challenges, not only the issue of how to achieve high precision state manipulation and robust quantum algorithms, but also on implementing qubit systems that allow for scaling up into large quantum networks. In contrast to contemporary digital electronics, which are entirely based on the same large-scale integration of silicon-based circuits, the implementation of a quantum computer necessitates multiple physical realizations of qubits designed for specific tasks. Thus far, potential qubit platforms based on a variety of different physical disciplines have been proposed, ranging from atomic and optical physics to solid-state devices, all posing advantages and disadvantages. A guiding principle is that systems utilizing separated subsystems, such as external optical or microwave cavities, are close realizations of isolated atoms, granting a high degree of precision. Meanwhile, qubits in embedded solid-state platforms offer scalability and implementation in quantum circuits [27]. Currently, spin-qubits based on semiconductor quantum dots are one of the most promising contenders for large-scale implementation. Due to its silicon-based nature, the spin-qubit has the advantage of utilizing an already well-established fabrication technology [28].

On the path to fault-tolerant quantum computing, it is widely recognized that one of the most critical aspects is to avoid the inevitable decoherence of large numbers of interacting qubits. This can be done either via less error prone qubits, for example in topological quantum computation [29], or through quantum error correction codes. Quantum error correction is based on encoding logical qubits so that they are resilient against the effects of noise, and such that their original state can be recovered if an error has been introduced [19]. A paradigmatic and powerful error correction code developed by P. W. Shor, involves the encoding of one logical qubit into nine physical qubits for redundancy [30]. This is achieved by generating maximally entangled three-qubit Greenberger-Horne-Zeilinger (GHZ)

states [31]. An adaptation of this correction scheme utilizing entanglement of nine optical beams, featuring squeezed states of light, has been experimentally demonstrated [32]. This not only proves that error correction protocols can be encoded in continuous-variables, but also that bosonic modes can serve as integral parts of quantum circuits, as opposed to mere interconnects for qubits.

Owing to their non-classical characteristics, squeezed states of light have been intensively studied in quantum optics and have important applications, for instance in quantum teleportation [33] and in metrology due to their reduced quantum noise [34]. Generation of squeezed light in the bosonic mode via parametric amplification has also been employed to achieve a non-equilibrium enhanced coupling strength [7, 35, 36]. However, very recently the squeezing of bosonic normal modes in ferromagnets - magnons - has been demonstrated [37]. Although care is required when making comparisons between the two, these squeezed magnon modes inherit many of the same features of the squeezed states of light, such as entanglement and coupling enhancement, but with the key difference that these properties are protected against decay by originating from energy minimization [38]. Accordingly, this calls for examining means of exploiting the robust equilibrium nature of squeezed magnons as a potential resource for processing quantum information.

In this thesis, we study a ferromagnet exchange-coupled to a spin-qubit, a hybrid platform combining two complimentary physical systems. This magnon|spin-qubit ensemble both profits from the already well-established framework of squeezed states of light in quantum optics and the scalability of a solid-state platform, thus offering a promising approach to address some of the challenges facing emerging quantum technologies. To investigate the advantages of this platform, we conduct a thorough theoretical analysis of the case of a ferromagnetic normal mode coupled to a single spin-qubit described by a QRM with novel capabilities. We then utilize these insights to consider the case of a squeezed magnon mode coupled to three spin-qubits, exploring the potential of generating entangled three-qubit GHZ states fundamental to Shor's 9-qubit error correction code. This is done using methodology consistent with previous studies of joint photon absorption [16, 18], to investigate a resonant transition where a single squeezed magnon synchronously excites three qubits. A perturbative derivation of the system's effective Hamiltonian is conducted, supplemented by a numerical analysis of the static and dynamic properties of the transition.

1.1 Structure of the master's thesis

The contents of this thesis can be summarized as follows. Firstly, in the second chapter, the preliminary concepts, theory and tools that are used throughout the thesis are presented. In section 2.1, the quantum harmonic oscillator along with the Fock states are briefly discussed. Moving on to section 2.2, the basic concepts of single-mode squeezed states, two-mode squeezed states and quadrature fluctuations are introduced. Section 2.4 reviews standard spin-wave theory and the special case of the isotropic ferromagnet. Furthermore, section 2.5 looks into the spin-qubit in terms of current technological advancements. As our findings are discussed in the context of quantum error correction, a brief background on this subject

is given in section 2.6.

The next three chapters serve as a combined results and discussion. Chapter 3 focuses on a theoretical investigation of the magnon|spin-qubit ensemble. The system Hamiltonian is derived by first considering the isolated subsystems and then the interaction between them. This is then discussed in terms of the squeezed light framework of quantum optics, establishing an intuitive physical picture of equilibrium magnon squeezing specifically for our system. Finally, the novel capabilities of these findings are treated in connection to the celebrated QRM.

Chapters 4 and 5, go into the theoretical and numerical analysis of concurrent three-qubit excitation by a single squeezed magnon. The fourth chapter focuses on a perturbative analysis of the transition in question, deriving the effective Hamiltonian and determining an expression for the overall transition amplitude in terms of the coupling strength. In the fifth chapter, a numerical investigation of the static and dynamic properties of the magnon|spin-qubit ensemble is given. Firstly, by evaluating the diagonalized Hamiltonian in terms of resonant couplings, and then by a quantitative analysis of the transition dynamics by a time evolution from the initial state with one squeezed magnon and three relaxed qubits. The final chapter, chapter 6, concludes our findings and proposes further work. A manuscript and supplemental materials culminating from the work carried out in this thesis, authored by Ida C. Skogvoll, Jonas Lidal, Jeroen Danon and Akashdeep Kamra, is currently under review and can be found in appendices A and B.

2 Preliminary concepts

This chapter presents the central concepts and tools that will be used in the remaining parts of this thesis. It begins with a brief discussion on the quantum harmonic oscillator model and review of the Fock states, followed by an introduction to the non-classical squeezed states of light. The QRM is presented along with a discussion of its integrability in various parameter regimes. Furthermore, standard spin-wave theory for the case of the isotropic ferromagnet is discussed, succeeded by a review of the spin-qubit, quantum error correction and Shor's nine-qubit code. As this thesis' activities are related to the work done in the preceding specialization project, parts of the theory has been directly reused from the previous project report [39]. This applies specifically to Sec. 2.1 and 2.3, apart from a few alterations.

2.1 The quantum harmonic oscillator

The Hamiltonian of the single-mode quantum harmonic oscillator is

$$\hat{H} = \frac{\hat{p}^2}{2m} + \frac{m}{2}\omega^2\hat{q}^2, \tag{2.1}$$

where $\hat{q}$ and $\hat{p}$ represent the Hermitian position and momentum operators [40]. The oscillator will be considered to be of unit mass for the remainder of this thesis, such that $m = 1$. A convenient algebraic alternative to solving the Schrödinger equation of the harmonic oscillator is to introduce the creation and annihilation operators in terms of position and momentum,

$$\hat{a} = \sqrt{\frac{\omega}{2\hbar}}\hat{q} + \frac{i}{\sqrt{2\hbar\omega}}\hat{p}, \qquad \hat{a}^\dagger = \sqrt{\frac{\omega}{2\hbar}}\hat{q} - \frac{i}{\sqrt{2\hbar\omega}}\hat{p}. \tag{2.2}$$

Here, $\hat{a}$ and $\hat{a}^\dagger$ satisfy the commutation relation

$$[\hat{a}, \hat{a}^\dagger] = 1. \tag{2.3}$$

It then follows directly that the Hamiltonian in Eq. (2.1) can be rewritten in terms of the creation and annihilation operators as

$$\hat{H} = \hbar\omega\big(\hat{a}^\dagger\hat{a} + \frac{1}{2}\big). \tag{2.4}$$

It is sometimes convenient to express operators by their time dependence. We can determine the time dependency of the annihilation and creation operators by using Heisenberg's equation, where the time-dependence of an arbitrary operator $\hat{O}$ reads

$$\frac{d\hat{O}}{dt} = \frac{i}{\hbar}[\hat{H}, \hat{O}]. \tag{2.5}$$

Using the commutation relation of Eq. (2.3), the time-dependence of $\hat{a}$ is found to be

$$\frac{d\hat{a}}{dt} = -i\omega\hat{a}, \tag{2.6}$$

which is a standard differential equation with solution

$$\hat{a}(t) = \hat{a}(0)e^{-i\omega t}. \tag{2.7}$$

Using the exact same procedure, the time dependence of $\hat{a}^\dagger$ is found to be

$$\hat{a}^\dagger(t) = \hat{a}^\dagger(0)e^{i\omega t}. \tag{2.8}$$

2.1.1 Fock states

Finding the eigenstates of Eq. (2.4) proceeds by determining the eigenstates of the operator $\hat{a}^\dagger\hat{a} = \hat{n}$. It can be shown that the eigenvalues of $\hat{n}$, also known as the number operator, are positive integers satisfying the relation

$$\hat{n}|n\rangle = n|n\rangle, \tag{2.9}$$

where $|n\rangle$ are the so-called Fock states. We then immediately see that the eigenvalues of Eq. (2.4) are

$$E_n = \hbar\omega\big(n + \frac{1}{2}\big). \tag{2.10}$$

Since commuting observables share an eigenbasis and $[\hat{H}, \hat{n}] = 0$, the Fock states are also eigenstates of the harmonic oscillator. Thus, n denotes the number of energy quanta that the harmonic oscillator exceeds the zero-point energy, $E_0 = \hbar\omega/2$ [41]. When the Hamiltonian in Eq. (2.4) represents a quantized electromagnetic mode, each quantum is a photon of energy $\hbar\omega$, where the zero-point energy corresponds to the vacuum state $|0\rangle$ [7].

The creation and annihilation operators act on the Fock states according to

$$\hat{a}^\dagger|n\rangle = \sqrt{n+1}|n+1\rangle \quad \text{and} \quad \hat{a}|n\rangle = \sqrt{n}|n-1\rangle, \tag{2.11}$$

which emphasizes the role of $\hat{a}$ and $\hat{a}^\dagger$ as ladder operators generating lower and higher levels of the harmonic oscillator. Hence, $\hat{a}$ destroys a photon of energy $\hbar\omega$ while $\hat{a}^\dagger$ creates a photon of energy $\hbar\omega$. From these relations, the central result follows that any Fock state $|n\rangle$ can be related to the vacuum state by the expression

$$|n\rangle = \frac{(\hat{a}^\dagger)^n}{\sqrt{n!}}|0\rangle. \tag{2.12}$$

With each state representing a level in the harmonic oscillator, the Fock states also form a complete orthonormal basis with completeness relation

$$\sum_{n=0}^{\infty} |n\rangle\langle n| = 1. \tag{2.13}$$

Any arbitrary field state $|\psi\rangle$ may then be expanded in terms of the Fock states as

$$|\psi\rangle = \sum_{n=0}^{\infty} C_n |n\rangle. \tag{2.14}$$

Performing a measurement on $|\psi\rangle$ for the number of photons, the probability of detecting n numbers of photons can be calculated as

$$P_n = |\langle n|\psi\rangle|^2 = |C_n|^2. \tag{2.15}$$

2.2 Squeezed states

One of the most important non-classical states of light are the squeezed states. The notion of squeezing in a system originates from the Heisenberg uncertainty principle, stating that given two operators $\hat{A}$ and $\hat{B}$, if they satisfy the commutation relation

$$[\hat{A}, \hat{B}] = i\hat{C}, \tag{2.16}$$

then the fluctuations, otherwise known as noise, in $\hat{A}$ and $\hat{B}$ are constrained by the relation

$$\Delta A \Delta B \geq \frac{1}{2}\left|\langle \hat{C} \rangle\right|. \tag{2.17}$$

Given this restriction, by definition, the system exhibits squeezing if either

$$\langle (\Delta \hat{A})^2 \rangle < \frac{1}{2}\left|\langle \hat{C} \rangle\right| \quad \text{or} \quad \langle (\Delta \hat{B})^2 \rangle < \frac{1}{2}\left|\langle \hat{C} \rangle\right|. \tag{2.18}$$

Thus, the decrease of noise in $\hat{A}$ comes at the expense of an increase of noise in $\hat{B}$. In terms of non-classical states of light, squeezing is determined through the quadrature operators,

$$\hat{X}_1 = \frac{1}{2}(\hat{a} + \hat{a}^\dagger), \quad \hat{X}_2 = \frac{1}{2i}(\hat{a} - \hat{a}^\dagger). \tag{2.19}$$

These are originally related to the quadrature of amplitudes of an electromagnetic field, but can be translated to the harmonic oscillator by recapitulating that they are equal to the position and momentum operators in Eq. (2.2), scaled to be dimensionless [7]. The quadrature operators also provide a convenient way of visualising various quantum states in phase space.

Using Eq. (2.3), the commutation relation of the quadrature operators is

$$[\hat{X}_1, \hat{X}_2] = \frac{i}{2}, \tag{2.20}$$

from which it follows that the system exhibits quadrature squeezing if either

$$\langle (\Delta \hat{X}_1)^2 \rangle < \frac{1}{4} \quad \text{or} \quad \langle (\Delta \hat{X}_2)^2 \rangle < \frac{1}{4}. \tag{2.21}$$

Incidentally, the fluctuations in each quadrature for the vacuum is equal to $\langle (\Delta \hat{X}_1)^2 \rangle = \langle (\Delta \hat{X}_2)^2 \rangle = \frac{1}{4}$. In other words, a state is squeezed if it has less noise in one quadrature than the vacuum state.

Mathematically, squeezed states are generated acting on a state with the squeezing operator,

$$\hat{S}(\xi) = e^{\frac{1}{2}(\xi^* \hat{a}^2 - \xi \hat{a}^{\dagger 2})}. \tag{2.22}$$

Here $\xi = re^{i\theta}$, in which $0 \leq r < \infty$ is the squeezing operator and $0 \leq \theta \leq 2\pi$ is the angle that the determines the direction of the squeezing. Additionally, it is a unitary operator and obeys

$$\hat{S}^\dagger(\xi)\hat{S}(\xi) = \hat{S}(\xi)\hat{S}^\dagger(\xi) = 1, \tag{2.23}$$

as well as $\hat{S}^\dagger(\xi) = \hat{S}(-\xi)$. The squeezing operator can act on any state, but in the specific case that it acts on the vacuum, the resulting state is called the squeezed vacuum state,

$$|\xi\rangle = \hat{S}(\xi)|0\rangle. \tag{2.24}$$

In the following, the squeezed vacuum state $|\xi\rangle$ will simply be referred to as the squeezed state. To determine the quadrature squeezing of this state, it is advantageous to first calculate the elements $\hat{S}^\dagger(\xi)\hat{a}\hat{S}(\xi)$ and $\hat{S}^\dagger(\xi)\hat{a}^\dagger\hat{S}(\xi)$, which can be interpreted as the squeezing transformation of the ladder operators. This is aided by employing the Baker-Hausdorff lemma [42],

$$e^{i\lambda\hat{A}}\hat{B}e^{-i\lambda\hat{A}} = \hat{B} + i\lambda[\hat{A},\hat{B}] + \frac{(i\lambda)^2}{2!}[\hat{A},[\hat{A},\hat{B}]] + ... \tag{2.25}$$

Setting $\hat{A} = \frac{1}{2}(\xi\hat{a}^{\dagger 2} - \xi^*\hat{a}^2)$ and $\hat{B} = \hat{a}, \hat{a}^\dagger$ and applying Eq. (2.3) twice, we obtain for the commutation relations

$$\begin{aligned}
[\frac{1}{2}(\xi\hat{a}^{\dagger 2} - \xi^*\hat{a}^2), \hat{a}] &= -\xi\hat{a}^\dagger \\
[\frac{1}{2}(\xi\hat{a}^{\dagger 2} - \xi^*\hat{a}^2), \hat{a}^\dagger] &= -\xi^*\hat{a},
\end{aligned} \tag{2.26}$$

giving for the first element

$$\begin{aligned}
\hat{S}^\dagger(\xi)\hat{a}\hat{S}(\xi) &= \hat{a} - \xi\hat{a}^\dagger + \frac{|\xi|^2}{2!}\hat{a} - \frac{\xi|\xi|^2}{3!}\hat{a}^\dagger + \frac{|\xi|^4}{4!}\hat{a} - \frac{\xi|\xi|^4}{5!}\hat{a}^\dagger ... \\
&= \hat{a} \times \sum_{n=0} \frac{r^{2n}}{(2n)!} - \hat{a}^\dagger \times re^{i\theta} \sum_{n=0} \frac{r^{2n}}{(2n+1)!} \\
&= \cosh r\,\hat{a} - e^{i\theta}\sinh r\,\hat{a}^\dagger.
\end{aligned} \tag{2.27}$$

By a corresponding calculation for the second element, $\hat{S}^\dagger(\xi)\hat{a}^\dagger\hat{S}(\xi)$,we obtain the final relations

$$\begin{aligned}
\hat{S}^\dagger(\xi)\hat{a}\hat{S}(\xi) &= \cosh r\,\hat{a} - e^{i\theta}\sinh r\,\hat{a}^\dagger, \\
\hat{S}^\dagger(\xi)\hat{a}^\dagger\hat{S}(\xi) &= \cosh r\,\hat{a}^\dagger - e^{-i\theta}\sinh r\,\hat{a}.
\end{aligned} \tag{2.28}$$

It is easily observed that both the elements, $\langle\xi|\hat{X}_1|\xi\rangle$ and $\langle\xi|\hat{X}_2|\xi\rangle$, vanish. We then obtain for the fluctuations in the first quadrature,

$$\langle(\Delta\hat{X}_1)^2\rangle = \langle\xi|\hat{X}_1^2|\xi\rangle = \frac{1}{4}\langle 0|\hat{S}^\dagger(\xi)(\hat{a}^2 + \hat{a}^\dagger\hat{a} + \hat{a}\hat{a}^\dagger + \hat{a}^{\dagger 2})\hat{S}(\xi)|0\rangle. \tag{2.29}$$

Initially focusing on the first expectation value, employing the unitarity of $\hat{S}(\xi)$ and Eq. (2.28), we obtain the expression

$$\begin{aligned}\langle 0|\hat{S}^\dagger(\xi)\hat{a}\hat{S}(\xi)\hat{S}^\dagger(\xi)\hat{a}\hat{S}(\xi)|0\rangle &= \langle 0|(\cosh r\,\hat{a} - e^{i\theta}\sinh r\,\hat{a}^\dagger)^2|0\rangle \\ &= -e^{i\theta}\sinh r\cosh r\end{aligned} \tag{2.30}$$

Executing the corresponding calculations for each of the three remaining terms in Eq. (2.29) and then analogously for $\langle\xi|\hat{X}_2^2|\xi\rangle$, we eventually acquire the final fluctuations in the squeezed state,

$$\langle(\Delta\hat{X}_{1,2})^2\rangle = \frac{1}{4}(\cosh^2 r + \sinh^2 r \pm 2\sinh r\cosh r\cos\theta). \tag{2.31}$$

For $\theta = 0$, this reduces to

$$\langle(\Delta\hat{X}_{1,2})^2\rangle = \frac{1}{4}e^{\mp 2r}, \tag{2.32}$$

where the effect of the squeezing is prominent. The larger the squeeze parameter is, the greater is the squeezing in the first quadrature, while the fluctuations in the second quadrature are subsequently exponentially increasing. The quantum fluctuations in squeezed states possess a robustness as a consequence of the geometrical constraint bestowed by the Heisenberg uncertainty principle. In phase space, this constraint can be illustrated as an ellipse with its minor axis aligned with the direction of squeezing, θ, as depicted in Fig. 2.1. Alternatively, if $\theta = \pi$, the direction of squeezing will be in the $\hat{X}_2$ quadrature.

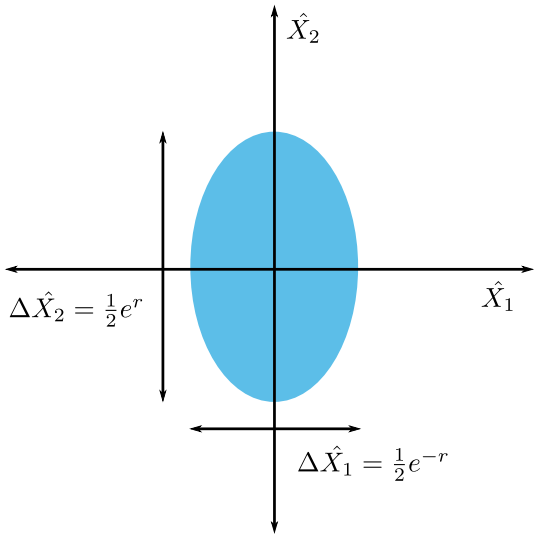

Figure 2.1: The Heisenberg uncertainty region of the squeezed state, represented by the blue ellipse, where the squeezing is present in the $\hat{X}_1$ quadrature. $\Delta\hat{X}_1$ and $\Delta\hat{X}_2$ are the quadrature fluctuations. The direction of squeezing is $\theta = 0$. The figure has been adapted from Ref. [7].

The theory of the squeezed states of light presented thus far has only considered a single-mode field, but can easily be extended to multimode fields. Here, we will briefly

focus on the case of two-mode squeezing. The two-mode squeeze operator reads

$$\hat{S}_2(\xi) = e^{\xi^* \hat{a}\hat{b} - \xi \hat{a}^\dagger \hat{b}^\dagger}, \tag{2.33}$$

where ξ is defined equivalently to the single-mode field and $\hat{a}$ and $\hat{b}$ represent the two different modes. The two-mode squeezed state is then defined as

$$|\xi\rangle_2 = \hat{S}_2(\xi)|0_a, 0_b\rangle. \tag{2.34}$$

Being that the two modes are correlated, the squeezing fluctuations are now not in each individual mode, but in a superposition of the two. The superposition quadrature operators are

$$\begin{aligned} \hat{X}_1 &= \frac{1}{2\sqrt{2}}(\hat{a} + \hat{a}^\dagger + \hat{b} + \hat{b}^\dagger), \\ \hat{X}_2 &= \frac{1}{2\sqrt{2}i}(\hat{a} - \hat{a}^\dagger + \hat{b} - \hat{b}^\dagger). \end{aligned} \tag{2.35}$$

By the same procedure as for calculating the single-mode quadrature fluctuations, the two-mode squeezing leads to identical fluctuations when $\theta = 0$, given by Eq. (2.32) [7].

2.3 The quantum Rabi model

The Rabi model was developed by I. I. Rabi as a semi-classical description of the light-matter interaction between a two-level system and a classical electric field [1, 2]. This model has since been revised in a more rigorous treatment, accounting for the influence of the vacuum modes of the universe [43]. The resulting fully quantized model describes the interaction between any two-level system, such as a qubit, and a single-mode bosonic field in a cavity. The two-level approximation is applicable to a wide variety of physical systems and justified in processes involving resonance phenomena, where the off-resonant transitions can be neglected. Under these conditions, all dynamics will essentially be contained within the two states. The reversible light-matter interaction in the QRM is described by the field of cavity quantum electrodynamics, which addresses the interaction between any two level system and a cavity mode [4]. In the discussion below, the terms harmonic oscillator and cavity will therefore be used interchangeably.

Consider a two level system, like a qubit, consisting of the ground and excited states $|g\rangle$ and $|e\rangle$. With these basis vectors, any arbitrary qubit state $|\chi\rangle$ can be defined through the relation

$$|\chi\rangle = \cos\frac{\theta}{2}|g\rangle + e^{i\phi}\sin\frac{\theta}{2}|e\rangle. \tag{2.36}$$

A commonly used and convenient representation visualizing the state space of a single qubit is the Bloch sphere, depicted in Fig. 2.2. Here, every point on the sphere corresponds to a pure qubit state. The qubit is for instance in its excited state when $\theta = 0$, while in the superposition $|\chi\rangle = (1/\sqrt{2})(|e\rangle + |g\rangle)$ by setting $\theta = \pi/2$ and $\phi = 0$. In accordance with this picture, operations on a qubit to alter its state are often referred to as qubit rotations.

The qubit physics may be described using the Pauli matrices, defining the transition operators

$$\hat{\sigma}^+ = |e\rangle\langle g| = \frac{1}{2}(\hat{\sigma}_x + i\hat{\sigma}_y), \qquad \hat{\sigma}^- = |g\rangle\langle e| = \frac{1}{2}(\hat{\sigma}_x - i\hat{\sigma}_y), \tag{2.37}$$

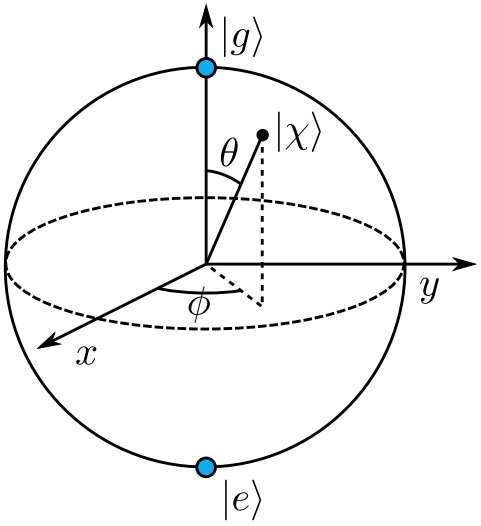

Figure 2.2: The Bloch sphere representation of a qubit in arbitrary state $|\chi\rangle$. The north and south poles on the sphere correspond to the ground and excited states of the qubit, respectively. These are conventionally denoted $|0\rangle$ and $|1\rangle$, but $|g\rangle$ and $|e\rangle$ are used for consistency with the notation of this thesis. The figure has been adapted from Ref. [19].

and the inversion operator

$$\hat{\sigma}_z = |e\rangle\langle e| - |g\rangle\langle g| = 2\hat{\sigma}^+\hat{\sigma}^- - 1. \tag{2.38}$$

These operators correspondingly follow the Pauli spin algebra, satisfying the commutation relations

$$[\hat{\sigma}^+, \hat{\sigma}^-] = \hat{\sigma}_z, \qquad [\hat{\sigma}_z, \hat{\sigma}^\pm] = \pm 2\hat{\sigma}^\pm. \tag{2.39}$$

Defining the ground and excited state of the qubit to be separated by an energy $\hbar\omega_q$ and the zero-point energy to lie halfway in between these states, the qubit Hamiltonian reads

$$\hat{H}_q = \frac{\hbar}{2}\omega_q\hat{\sigma}_z, \tag{2.40}$$

and the Hamiltonian of the cavity may be described using Eq. (2.4) as

$$\hat{H}_c = \hbar\omega_0\hat{a}^\dagger\hat{a}, \tag{2.41}$$

neglecting the zero-point energy and where ω_0 is the cavity frequency. Following the semi-classical approach, the interaction between the qubit and the cavity is described with regards to the quantized dipole moment and electric field, $\hat{H}_I = -\hat{\mathbf{d}}\cdot\hat{\mathbf{E}}$, where the electric field is expressed as

$$\hat{\mathbf{E}} = \hat{\mathbf{e}}\left(\frac{\hbar\omega_0}{\epsilon_0 V_0}\right)^{\frac{1}{2}}(\hat{a} + \hat{a}^\dagger)\sin(kz). \tag{2.42}$$

The vector $\hat{\mathbf{e}}$ denotes the polarization vector, z is the position variable of a one-dimensional cavity and k is the wave-number. V_0 is the modal volume of the resonant cavity. Due to the parity selection rules of the dipole moment, only the off-diagonal elements remain, such that

$$\hat{\mathbf{d}} = d|g\rangle\langle e| + d^*|e\rangle\langle g| = d(\hat{\sigma}^+ + \hat{\sigma}^-), \tag{2.43}$$

where it has been assumed that the dipole moment, d, is real without loss of generality. Now, defining the coupling strength

$$g = -d \cdot \left(\frac{\omega_0}{\hbar \epsilon_0 V_0}\right)^{\frac{1}{2}} \sin(kz), \tag{2.44}$$

the final Hamiltonian for the coupled qubit-cavity system reads

$$\hat{H} = \hat{H}_q + \hat{H}_c + \hat{H}_I = \frac{\hbar}{2}\omega_q \hat{\sigma}_z + \hbar\omega_0 \hat{a}^\dagger \hat{a} + \hbar g(\hat{\sigma}^+ + \hat{\sigma}^-)(\hat{a} + \hat{a}^\dagger). \tag{2.45}$$

The bare states of the uncoupled Hamiltonian ($g = 0$) are then a product of the eigenstates of each composite system,

$$|\psi\rangle = |n\rangle \otimes |\chi\rangle = |n, \chi\rangle, \tag{2.46}$$

where $|\chi\rangle$ is the state of the qubit and $|n\rangle$ is the state of the cavity. The ground state of the system is the state where the qubit is in its ground state and the cavity is in the vacuum state,

$$|\psi_0\rangle = |0, g\rangle. \tag{2.47}$$

The dynamics of Eq. (2.45) are largely determined by the four terms in the interaction Hamiltonian. The term proportional to $\hat{\sigma}^- \hat{a}^\dagger$ can be interpreted as the absorption of one photon by the cavity and the qubit relaxing to the ground state, while the term $\hat{\sigma}^+ \hat{a}$ describes the emission of a photon and the excitation of the qubit. In this sense, these are terms corresponding to processes that conserve the number of excitations. The remaining terms, $\hat{\sigma}^- \hat{a}$ and $\hat{\sigma}^+ \hat{a}^\dagger$, are non-conserving in the sense they either excite or relax both systems. The total number of excitations change by two. These elements of the interaction Hamiltonian are called the rotating and counter-rotating terms [7]. An illustration of a possible system described by Eq. (2.45), depicting the coupling between the cavity and the two-level qubit, is presented in Fig. 2.3.

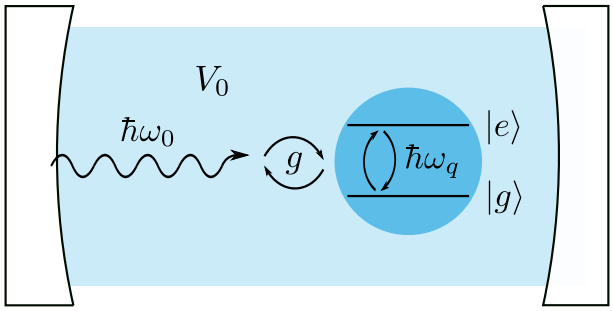

Figure 2.3: A representation of the coupled qubit-cavity system. The strength of the interaction is determined by the coupling strength g. The frequency of the single-mode cavity field is ω_0, while ω_q is the frequency of the $|e\rangle \leftrightarrow |g\rangle$ transition. V_0 is the modal volume of the cavity. The curved walls indicate the concaved mirrors reflecting the photons. The illustration has been adapted from Ref. [4].

The integrability of the QRM is governed by the existence of a discrete symmetry, arising from the fact that the total Hamiltonian of Eq. (2.45) commutes with the parity operator [6].

The parity operator of the composite system can be defined through the total excitation number $\hat{N}$ as

$$\Pi = e^{i\pi\hat{N}} = e^{i\pi(\hat{a}^\dagger\hat{a}+\hat{\sigma}^+\hat{\sigma}^-)}, \tag{2.48}$$

where the $\hat{N}$ is defined in terms of the eigenstates of the uncoupled system. This can be re-expressed by Taylor-expanding the exponential,

$$\begin{aligned} e^{i\pi(\hat{a}^\dagger\hat{a}+\hat{\sigma}^+\hat{\sigma}^-)} &= e^{i\pi\hat{a}^\dagger\hat{a}}e^{i\frac{\pi}{2}(\hat{\sigma}_z+1)} \\ &= i(-1)^{\hat{a}^\dagger\hat{a}}\sum_n\left(\frac{i\pi}{2}\right)^n\frac{(\hat{\sigma}_z)^n}{n!} \\ &= i(-1)^{\hat{a}^\dagger\hat{a}}\begin{pmatrix} i & 0 \\ 0 & -i \end{pmatrix} \\ &= -(-1)^{\hat{a}^\dagger\hat{a}}\hat{\sigma}_z. \end{aligned} \tag{2.49}$$

The commutation between $\hat{H}_q$, $\hat{H}_c$ and Π is straightforward, considering the operators of each separate subsystem automatically commute and the operators within each subsystem coincide. Hence, the parity is a conserved quantity. A major part of understanding the dynamics in this model is to observe that the time-evolution of states is governed by this parity symmetry [44]. The eigenstates of the parity operator must necessarily be eigenstates of the Hamiltonian, each having an eigenvalue $\Pi|p\rangle = p|p\rangle$ of either $p = +1$ or $p = -1$ [45]. As a result, the Hilbert space decomposes into two irreducible and unconnected subspaces,

$$\mathscr{H} = \mathscr{H}_+ \oplus \mathscr{H}_-. \tag{2.50}$$

both infinite dimensional and each containing states of a specific parity, more accurately referred to as parity chains. The adjacent quantum states within each parity chain will be entangled through the rotating and counter-rotating terms of Eq. (2.45), and all dynamics will evolve independently staying within either chain, see Fig. 2.4.

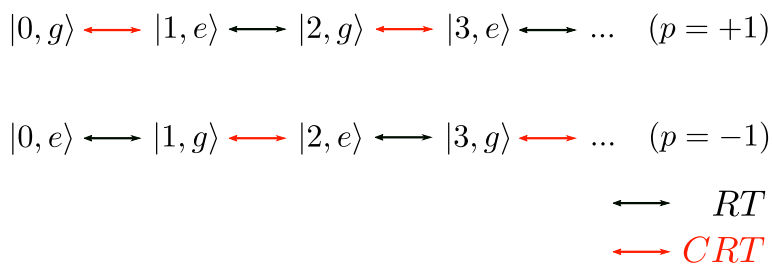

Figure 2.4: Symmetry of the two unconnected subspaces of the QRM. The Hilbert space splits into two parity chains, where neighbouring states are connected by rotating terms (black arrows) and counter-rotating terms (red arrows).

2.3.1 Strong-coupling regime: the Jaynes-Cummings model

Quantum optics define different coupling regimes depending on the size of the coupling strength g relative to the natural system frequencies and decoherence rates. In the SC

regime, the coupling strength is strong enough that it exceeds the system decay rates, but weak enough that the total Rabi Hamiltonian may be approximated in such a way that it can be solved analytically. Below this limit, spontaneous emission events will destroy the superposition of states and no oscillation phenomena will arise [4]. The integrability of the SC regime is most easily recognized when the interaction Hamiltonian of Eq. (2.45) is transformed into the rotating frame. The free-field dependencies of $\hat{a}$ and $\hat{a}^\dagger$ were presented in Eqs. (2.7) and (2.8), and the uncoupled transition operators are determined using Eq. (2.5) and Eq. (2.39),

$$\frac{d\hat{\sigma}^\pm}{dt} = \frac{i}{\hbar}[\hat{H}, \hat{\sigma}_z] = \frac{i}{\hbar}[\frac{\hbar}{2}\omega_q \hat{\sigma}_z, \hat{\sigma}^\pm] = \pm i\omega_q \hat{\sigma}^\pm. \tag{2.51}$$

which has the solution

$$\hat{\sigma}^\pm(t) = \hat{\sigma}^\pm(0) e^{\pm i\omega_q t}. \tag{2.52}$$

Inserting these relations into Eq. (2.45), the interaction Hamiltonian satisfies

$$\hat{H}_I = \hbar g(\hat{\sigma}^+ \hat{a} e^{i(\omega_q-\omega_0)t} + \hat{\sigma}^+ \hat{a}^\dagger e^{i(\omega_q+\omega_0)t} + \hat{\sigma}^- \hat{a} e^{-i(\omega_q+\omega_0)t} + \hat{\sigma}^- \hat{a}^\dagger e^{-i(\omega_q-\omega_0)t}), \tag{2.53}$$

where for the moment, $\hat{a}$ and $\hat{\sigma}$ are given at $t = 0$. We can observe that the non-conserving terms, the middle counter-rotating terms, rotate at a frequency $\omega_q + \omega_0$ while the energy-conserving terms rotate at a frequency $\omega_q - \omega_0$. Thus, when $\omega_q \approx \omega_0$, the counter-rotating terms oscillate much faster than the rotating terms. As a result, provided that $|\omega_q - \omega_0| \ll \omega_q + \omega_0$ and the coupling strength is in the SC regime, the rapidly oscillating terms of the interaction Hamiltonian can be ignored due to their effects averaging out over any time scale of interest. This approximation is referred to as the rotating wave approximation (RWA) [7]. Transforming the interaction Hamiltonian back to the Schrödinger picture, the full Hamiltonian reads

$$\hat{H}_{JC} = \frac{\hbar}{2}\omega_q \hat{\sigma}_z + \hbar\omega_0 \hat{a}^\dagger \hat{a} + \hbar g(\hat{\sigma}^+ \hat{a} + \hat{\sigma}^- \hat{a}^\dagger), \tag{2.54}$$

where the JC-subscript is used to signify that this is the exactly solvable Hamiltonian of the renowned Jaynes-Cummings model, developed by E. T. Jaynes and F. W. Cummings in 1963 [46]. This model was an integral part of the development of the field of cavity quantum electrodynamics for several decades after reaching the SC regime [47].

The Hamiltonian of Eq. (2.54) commutes with the number operator $\hat{N}$, such that total excitation number is a conserved quantity. Since the counter-rotating terms have been omitted, only the states of equal excitation numbers are coupled through the rotating terms $\hat{\sigma}^+ \hat{a}$ and $\hat{\sigma}^- \hat{a}^\dagger$ [3], namely the bare states $|n, e\rangle$ and $|n+1, g\rangle$. Consequently, the Hilbert space of the Rabi Hamiltonian decomposes into an infinite sum of two dimensional dynamically invariant subspaces [48]. The ground state $|0, g\rangle$ is a true ground state as it is not coupled to any other state. This larger degree of symmetry as opposed to the QRM is what renders the Jaynes-Cummings model exactly solvable. Applying the RWA reduces the problem to solving separate two-level systems.

The following discussion proposes a solution to the Jaynes-Cummings Hamiltonian largely based on Ref. [7]. Using the bare states $|n, e\rangle$ and $|n+1, g\rangle$, the matrix representation of Eq. (2.45) reads

$$H_{JC}^n = \hbar \begin{bmatrix} n\omega_0 + \frac{\omega_q}{2} & g\sqrt{n+1} \\ g\sqrt{n+1} & \omega_0(n+1) - \frac{\omega_q}{2} \end{bmatrix} \tag{2.55}$$

which can be solved to give the eigenenergies

$$E_n^{\pm} = \hbar\omega_0\Big(n+\frac{1}{2}\Big) \pm \frac{1}{2}\hbar\Omega_n(\Delta). \tag{2.56}$$

By definition, $\Omega_n(\Delta)$ is the so-called Rabi frequency, with the expression

$$\Omega_n(\Delta) = \big(\Delta^2 + 4g^2(n+1)\big)^{1/2}, \tag{2.57}$$

where $\Delta = \omega_q - \omega_0$ denotes the system detuning. The corresponding eigenstates are referred to as the dressed states,

$$\begin{aligned} |n,+\rangle &= \cos\Big(\frac{\Phi_n}{2}\Big)|n,e\rangle + \sin\Big(\frac{\Phi_n}{2}\Big)|n+1,g\rangle \\ |n,-\rangle &= -\sin\Big(\frac{\Phi_n}{2}\Big)|n,e\rangle + \cos\Big(\frac{\Phi_n}{2}\Big)|n+1,g\rangle, \end{aligned} \tag{2.58}$$

with the angle Φ_n defined through the relations,

$$\sin\Big(\frac{\Phi_n}{2}\Big) = \frac{1}{\sqrt{2}}\Big(\frac{\Omega_n(\Delta)-\Delta}{\Omega_n(\Delta)}\Big)^{1/2} \quad \text{and} \quad \cos\Big(\frac{\Phi_n}{2}\Big) = \frac{1}{\sqrt{2}}\Big(\frac{\Omega_n(\Delta)+\Delta}{\Omega_n(\Delta)}\Big)^{1/2}. \tag{2.59}$$

Even in the case of no detuning, the dressed states are separated by a non-linear energy-splitting. They therefore form a hierarchy of levels that are referred to as the Jaynes-Cummings ladder. Setting the initial state $|\psi(0)\rangle = |n,e\rangle$, the state vector $|\psi(t)\rangle$ is easily determined in terms of the dressed states,

$$|\psi(t)\rangle = e^{-i\hat{H}t/\hbar}|\psi(0)\rangle = \cos\Big(\frac{\Phi_n}{2}\Big)|n,+\rangle e^{-iE_n^+ t/\hbar} - \sin\Big(\frac{\Phi_n}{2}\Big)|n,-\rangle e^{-iE_n^- t/\hbar} \tag{2.60}$$

Switching back to the bare states using Eq. (2.58), setting $\Delta = 0$ and omitting irrelevant phase factors, we obtain the simplified time-evolution

$$|\psi(t)\rangle = \cos\Big(gt\sqrt{n+1}\Big)|n,e\rangle - i\sin\Big(gt\sqrt{n+1}\Big)|n+1,g\rangle. \tag{2.61}$$

The probabilities that the system is in either of the states $|n+1,g\rangle$ and $|n,e\rangle$, are then

$$\begin{aligned} P_{|n,e\rangle}(t) &= \big|C_{|n,e\rangle}(t)\big|^2 = \cos^2(gt\sqrt{n+1}), \\ P_{|n+1,g\rangle}(t) &= \big|C_{|n+1,g\rangle}(t)\big|^2 = \sin^2(gt\sqrt{n+1}). \end{aligned} \tag{2.62}$$

It is apparent that the probabilities oscillate oppositely with the same frequency. Hence, when the coupling is strong enough that the RWA can be applied, there is a coherent and reversible exchange of energy, a single photon, between the qubit and the cavity. These are the Rabi oscillations. The qubit inversion dynamics can be defined in terms of the inversion operator,

$$\begin{aligned} W(t) &= \langle\psi(t)|\hat{\sigma}_z|\psi(t)\rangle \\ &= \cos\Big(2gt\sqrt{n+1}\Big). \end{aligned} \tag{2.63}$$

As made evident from the discussion above, the transition from $|0,e\rangle$ to $|1,g\rangle$ can be achieved by turning on the interaction for the amount of time that $2gt = \pi$, also referred to as a π-pulse. A plot of the evolution of the initial state $|0,e\rangle$ with $g = 0.5\omega_0$ is depicted in Fig. 2.5. Note that despite the coupling strength being outside of the SC regime, the absence of counter-rotating terms in $\hat{H}_{JC}$ used in the simulation limits the dynamics to the ground and first excited state.

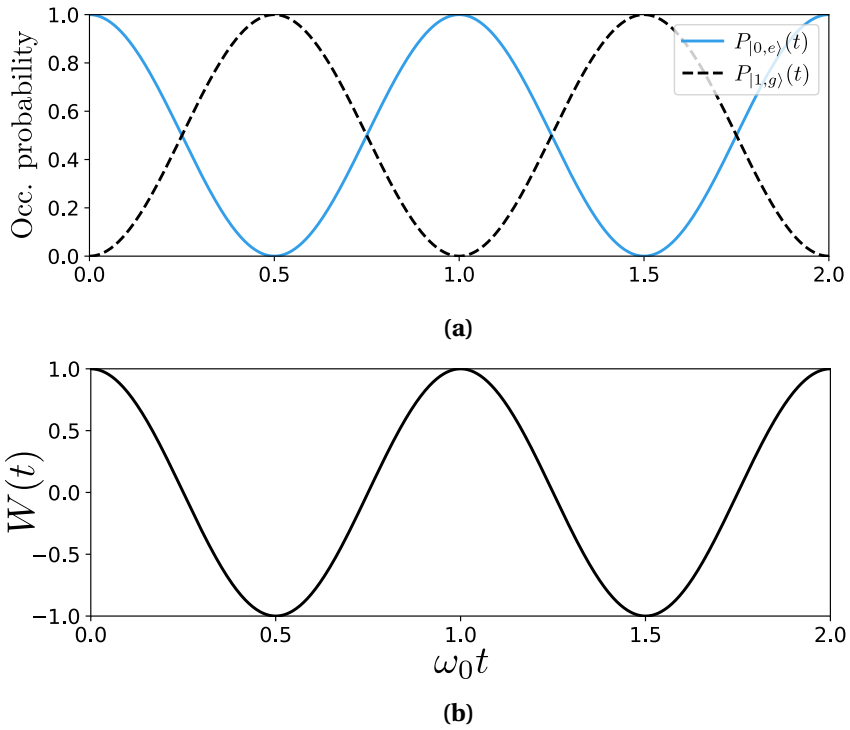

Figure 2.5: Rabi oscillations between the bare states $|0,e\rangle \leftrightarrow |1,g\rangle$, with initial state $|i\rangle = |0,e\rangle$. (a) Probabilities of each of the states, calculated from the expectation value of the projection operators $\hat{P}_{|0,e\rangle} = |0,e\rangle\langle 0,e|$ and $\hat{P}_{|1,g\rangle} = |1,g\rangle\langle 1,g|$. (b) Qubit inversions, $W(t) = \left|C_{|0,e\rangle}(t)\right|^2 - \left|C_{|1,g\rangle}(t)\right|^2$. Both plots have coupling strength $g = 0.5\omega_0$ and cavity and qubit frequencies $\omega_0 = \omega_q = 2\pi$.

2.3.2 Ultra-strong and deep-strong coupling regimes

With persistent technological advances in recent years within the field of cavity quantum electrodynamics and related disciplines, even stronger coupling regimes in physical setups have been achieved where the static and dynamic properties of the system exhibit counter-intuitive behavior. When the coupling strength between the qubit and the cavity field is a substantial fraction of the unperturbed frequencies of the system, around $g/\omega > 0.1$, the RWA can no longer be invoked. As mentioned in the previous section, this is due to the counter-rotating terms being too large to be neglected. Consequently, the number of excitations in the system are no longer conserved and the Hilbert space symmetry returns to the parity symmetry of the QRM. This parameter regime is called the USC regime. An essential distinction between this regime and the SC regime is that the counter-rotating terms enable virtual energy non-conserving transitions that cannot be related to a physically observable particle [16]. The counter-rotating terms additionally introduce imperceptible excitations and virtual photons in the ground state of the system, such that

$$\langle 0|\hat{a}^\dagger \hat{a}|0\rangle \neq 0. \tag{2.64}$$

The existence of the excitation number non-conserving terms in the Hamiltonian create novel, counter-intuitive physical phenomena which are manifested in the chaotic behavior of transitions in this regime. It is no longer described by strictly periodic

oscillations, as in the Jaynes-Cummings model. The two very first works demonstrating this ultra-strong coupling used superconducting flux qubits galvanically connected to an LC-resonator circuit, more specifically by Niemczyk et al. and Forn-Díaz et al., respectively [9, 49]. Ultra-strong coupling has also been realised in other systems, such as microcavity excition-polaritons in quantum wells [50]. The access to increasingly stronger light-matter coupling is a key requisite to the development of emerging quantum technologies. The novel phenomena of the USC regime have for instance been used to simultaneously excite two atoms by a single photon [18], and also have a proposed application in quantum information protocols for ultra-fast quantum computation and remote entanglement [5, 23, 36].

When the coupling strength surpasses the frequency of the cavity, $g/\omega_0 > 1.0$, the system enters the deep-strong coupling (DSC) regime [51] and the dynamics are mainly driven by the interaction. The behavior of this regime was largely unexplored until very recently, seeing as it was experimentally realized only during the past few years. The first work demonstrating this coupling strength used superconducting flux qubits, performed by Yoshihara et al. in 2017 [10]. It has also been achieved in superconducting circuits and gold nanoparticle crystals [52, 53]. Although an exact analytical solution to the QRM valid in all parameter regimes has been found, it involves complex calculations and provides no intuitive picture of the dynamics of the system [6, 47]. There is therefore still high scientific value in experimentally investigating the phenomena of the QRM beyond the USC regime. Theoretical studies thus far show that alike the SC regime, the Hamiltonian can be treated perturbatively in the DSC regime and approximate that of a degenerate qubit, such that the system exhibits coherent and periodic collapse and revival of the state population within each parity chain [39, 45].

2.4 Spin-wave theory

In 1926, Dirac and Heisenberg independently discovered that collective magnetism, such as ferro- and antiferromagnetism, is a result of the purely quantum mechanical origin that is the exchange interaction. This interaction arises from the electrostatic Coulomb interaction and when derived, possesses the non-classical feature of indistinguishability between identical particles and thus culminates from the Pauli exclusion principle. Electrons of parallel spins cannot exist in the same state at the same time, ultimately leading to a reduction in the Coulomb energy. This effect is one of the decisive mechanisms behind the spontaneous magnetization that occurs in ferromagnets.

One of the most successful and important models for describing magnetic phenomena is the Heisenberg model. It assumes the existence of permanent and localized magnetic moments, which interact either through a direct or indirect exchange interaction. It thereby best describes magnetic insulators and metals with localized moments [54]. The simplest form of the Heisenberg Hamiltonian is

$$\hat{H} = -\sum_{i,j} J_{ij} \hat{\mathbf{S}}_i \cdot \hat{\mathbf{S}}_j, \tag{2.65}$$

where i and j refer to specific lattice sites and $\hat{\mathbf{S}}_i$ is the angular momentum operator situated on lattice site i. The coefficient J_{ij} is the exchange constant. This Hamiltonian

can be interpreted as an effective operator, where the $\hat{\mathbf{S}}_i \cdot \hat{\mathbf{S}}_j$ term represents the exchange interaction occurring between spins on different lattice sites. The model is completely generalized and can be applied to any type of lattice.

The spin operators follow the standard SU(2) algebra, with commutation relation

$$[\hat{S}_{ix}, \hat{S}_{jy}] = i\hbar \hat{S}_{iz} \delta_{ij}, \tag{2.66}$$

where the x, y, z indices are interchanged by cyclic permutation. Operators from different lattice sites evidently commute. It is computationally advantageous to express the $\hat{x}$ and $\hat{y}$ components of the spin operator through the spin raising and lowering operators,

$$\begin{aligned} \hat{S}_i^+ &= \hat{S}_{ix} + i\hat{S}_{iy} \\ \hat{S}_i^- &= \hat{S}_{ix} - i\hat{S}_{iy}. \end{aligned} \tag{2.67}$$

The raising and lowering operators act on a spin state by increasing and decreasing the total spin on site i, quantified by the projection of the angular momentum along the $\hat{z}$-axis. By simple insertion of Eq. (2.67), the Heisenberg Hamiltonian reads

$$\hat{H} = -\sum_{i,j} J_{ij} \Big[\frac{1}{2} \big(\hat{S}_i^+ \hat{S}_j^- + \hat{S}_i^- \hat{S}_j^+ \big) + \hat{S}_{iz} \hat{S}_{jz} \Big]. \tag{2.68}$$

Due to the commutator of spin operators being an operator in itself, these are cumbersome to work with. We may therefore more conveniently express them through the canonical bosonic ladder operators. These operators are independent and can be expressed in terms of the spin operators through the Holstein-Primakoff transformation [55], defined by

$$\begin{aligned} \hat{S}_i^+ &= \sqrt{2S} \hat{a}_i^\dagger \Big(1 - \frac{\hat{a}_i^\dagger \hat{a}_i}{2S} \Big)^{\frac{1}{2}} \\ \hat{S}_i^- &= \sqrt{2S} \Big(1 - \frac{\hat{a}_i^\dagger \hat{a}_i}{2S} \Big)^{\frac{1}{2}} \hat{a}_i, \end{aligned} \tag{2.69}$$

where it has been assumed that in the ground state, all spins point in the $-\hat{\mathbf{z}}$-direction with lowest possible spin-projection on the z-axis. Thus, the application of $\hat{S}_i^+$ raises the z-component of the spin at site i by 1, and vice versa. It follows that the $\hat{z}$-component of the spin operator is described by the relation

$$\hat{S}_{iz} = \hat{a}_i^\dagger \hat{a}_i - S. \tag{2.70}$$

The bosonic annihilation and creation operators on different lattice sites commute, i.e. $[\hat{a}_k, \hat{a}_l^\dagger] = \delta_{kl}$, which also will satisfy the correct commutation relations for the original spin operators [56]. The number operator $\hat{a}_i^\dagger \hat{a}_i = \hat{n}_i$ denotes the number of "flipped" spins found on site i. In contrast to the unbounded ladder operator of the Fock states, it is evident from Eq. (2.69) that the value of $\hat{n}_i$ is restricted to satisfy the constraint

$$\langle \hat{n}_i \rangle \leq 2S. \tag{2.71}$$

By making a low-temperature approximation, the total number of spins in a magnetic system is assumed to be much larger than the number of spin deviations. The square root in Eq. (2.69) can thus be Taylor-expanded to give [57]

$$\Big(1 - \frac{\hat{a}_i^\dagger \hat{a}_i}{2S} \Big)^{\frac{1}{2}} = 1 - \frac{\hat{a}_i^\dagger \hat{a}_i}{4S} - \frac{\hat{a}_i^\dagger \hat{a}_i \hat{a}_i^\dagger \hat{a}_i}{32S^2} + \ldots \approx 1, \tag{2.72}$$

such that the Holstein-Primakoff transformation can be rewritten as

$$\begin{aligned}\hat{S}_i^+ &\approx \sqrt{2S}\hat{a}_i^\dagger \\ \hat{S}_i^- &\approx \sqrt{2S}\hat{a}_i.\end{aligned} \tag{2.73}$$

This ultimately means that all higher order terms vanish and interactions between bosons are neglected.

2.4.1 Isotropic ferromagnet

The Heisenberg model introduced in the previous section can be used to prove that the elementary excitations in a spin system which is coupled through exchange interactions, have a wave-like nature and are thereby dubbed spin-waves. These waves are quantized and each quantum is called a magnon [56]. Spin-waves exist in a variety of different ordered magnets, however this discussion will be limited to considering the case of the isotropic ferromagnet.

In its ground state, all spins in a ferromagnet are spontaneously ordered to align in the same direction, which we will choose to be $-\hat{\mathbf{z}}$. It is assumed that the exchange interaction can be limited to only nearest neighbour interactions, thus $J_{ii} = 0$ and $J_{ij} = J_{ji} = J$. The sites j are defined by $j = i + \boldsymbol{\delta}$, where the vector $\boldsymbol{\delta}$ connects the atom on site i to all its nearest neighbours. The simplest Hamiltonian depicting an isotropic ferromagnet is,

$$\hat{H}_F = -J\sum_{i,\boldsymbol{\delta}} \hat{\mathbf{S}}_i \cdot \hat{\mathbf{S}}_{i+\boldsymbol{\delta}} + \left|\gamma\right|\mu_0 H_0 \sum_i \hat{S}_{iz}. \tag{2.74}$$

The first term is identical to Eq. (2.65), while the second term added is the Zeeman energy from a static magnetic field, $\mu_0 H_0$, with negative gyromagnetic ratio γ. Setting $J > 0$, it is energetically favorable for the spins to align in the same direction. We note that for convenience, from this point on, $\hbar = 1$ throughout this thesis. Additionally the total number of lattice sites is N_F and the number of nearest neighbours will be denoted z.

Inserting Eqs. (2.70) and (2.73) of the Holstein-Primakoff transformation into the ferromagnetic Hamiltonian and neglecting all terms above second order gives

$$\hat{H}_F = E_0 - JS\sum_{i,\boldsymbol{\delta}} \left[\hat{a}_i^\dagger \hat{a}_{i+\boldsymbol{\delta}} + \hat{a}_i \hat{a}_{i+\boldsymbol{\delta}}^\dagger - \hat{a}_i^\dagger \hat{a}_i - \hat{a}_{i+\boldsymbol{\delta}}^\dagger \hat{a}_{i+\boldsymbol{\delta}}\right] + \left|\gamma\right|\mu_0 H_0 \sum_i \hat{a}_i^\dagger \hat{a}_i, \tag{2.75}$$

where the ground state energy, E_0, reads

$$E_0 = -\left|\gamma\right|\mu_0 H_0 S N_F - JS^2 N_F z. \tag{2.76}$$

However, considering that we are interested in excitations above the ground state, the ground state energy is not of importance and will be discarded for the rest of the discussion.

The Hamiltonian can be diagonalized by introducing the Fourier transformed bosonic operators,

$$\begin{aligned}\hat{a}_i^\dagger &= \frac{1}{\sqrt{N_F}}\sum_{\mathbf{k}} \hat{a}_{\mathbf{k}}^\dagger e^{i\mathbf{k}\cdot\mathbf{r_i}} \\ \hat{a}_i &= \frac{1}{\sqrt{N_F}}\sum_{\mathbf{k}} \hat{a}_{\mathbf{k}} e^{-i\mathbf{k}\cdot\mathbf{r_i}},\end{aligned} \tag{2.77}$$

following the sign convention of Ref. [56]. The ladder operators in reciprocal space now follow the commutation relation,

$$\left[\hat{\alpha}_{\mathbf{k}}, \hat{\alpha}^{\dagger}_{\mathbf{k}'}\right] = \delta_{\mathbf{k},\mathbf{k}'}, \tag{2.78}$$

and analogously to the ladder operators in real space, the operators $\hat{a}^{\dagger}_{\mathbf{k}}$ and $\hat{a}_{\mathbf{k}}$ create and annihilate magnons with wavevector $\mathbf{k}$, respectively. With periodic boundary conditions imposed on the lattice, this means that $\mathbf{k}$ will only lie within the first Brillouin zone. Inserting Eq. (2.77), the Hamiltonian reads

$$\begin{aligned}\hat{H}_F = &-\frac{JS}{N_F}\sum_{i\mathbf{k}\mathbf{k}'\boldsymbol{\delta}}\left[\hat{a}^{\dagger}_{\mathbf{k}}\hat{a}_{\mathbf{k}'}e^{i(\mathbf{k}-\mathbf{k}')\cdot\mathbf{r}_i}e^{-i\mathbf{k}'\cdot\boldsymbol{\delta}} + \hat{a}_{\mathbf{k}}\hat{a}^{\dagger}_{\mathbf{k}'}e^{-i(\mathbf{k}-\mathbf{k}')\cdot\mathbf{r}_i}e^{i\mathbf{k}'\cdot\boldsymbol{\delta}}\right.\\ &\left.-\hat{a}^{\dagger}_{\mathbf{k}}\hat{a}_{\mathbf{k}'}e^{i(\mathbf{k}-\mathbf{k}')\cdot\mathbf{r}_i} - \hat{a}^{\dagger}_{\mathbf{k}}\hat{a}_{\mathbf{k}'}e^{i(\mathbf{k}-\mathbf{k}')\cdot(\mathbf{r}_i+\boldsymbol{\delta})}\right]\\ &+\left|\gamma\right|\mu_0 H_0\sum_{i\mathbf{k}\mathbf{k}'}\hat{a}^{\dagger}_{\mathbf{k}}\hat{a}_{\mathbf{k}'}e^{i(\mathbf{k}-\mathbf{k}')\cdot\mathbf{r}_i}.\end{aligned} \tag{2.79}$$

Due to the periodicity of the lattice, all the exponential terms will vanish when summing over i, unless $\mathbf{k}=\mathbf{k}'$. Thus, all terms $\sum_i e^{i(\mathbf{k}-\mathbf{k}')\cdot\mathbf{r_i}} = N_F\delta_{\mathbf{k}\mathbf{k}'}$. The resulting Hamiltonian is now

$$\hat{H}_F = -JSz\sum_{\mathbf{k}\boldsymbol{\delta}}\left[\hat{a}^{\dagger}_{\mathbf{k}}\hat{a}_{\mathbf{k}}\gamma_{-\mathbf{k}} + \hat{a}_{\mathbf{k}}\hat{a}^{\dagger}_{\mathbf{k}}\gamma_{\mathbf{k}} - 2\hat{a}^{\dagger}_{\mathbf{k}}\hat{a}_{\mathbf{k}}\right] + \left|\gamma\right|\mu_0 H_0\sum_{\mathbf{k}}\hat{a}^{\dagger}_{\mathbf{k}}\hat{a}_{\mathbf{k}}, \tag{2.80}$$

where $\gamma_{\mathbf{k}}$ depends on the type of lattice and is defined as

$$\gamma_{\mathbf{k}} = \frac{1}{z}\sum_{\mathbf{k}} e^{i\mathbf{k}\cdot\boldsymbol{\delta}}. \tag{2.81}$$

Using the commutation relation of $\hat{a}_{\mathbf{k}}$ and $\hat{a}^{\dagger}_{\mathbf{k}}$ and assuming center of symmetry, the final diagonalized Hamiltonian is

$$\hat{H}_F = \sum_{\mathbf{k}}\left(\left|\gamma\right|\mu_0 H_0 + 2JSz(1-\gamma_{\mathbf{k}})\right)\hat{a}^{\dagger}_{\mathbf{k}}\hat{a}_{\mathbf{k}}. \tag{2.82}$$

The operator $\hat{a}^{\dagger}_{\mathbf{k}}\hat{a}_{\mathbf{k}}$ counts the number of magnons with wavevector $\mathbf{k}$ and resonance frequency $\omega_{\mathbf{k}} = \left|\gamma\right|\mu_0 H_0 + 2JSz(1-\gamma_{\mathbf{k}})$. The frequency $\omega_0 = \left|\gamma\right|\mu_0 H_0$ is the ferromagnetic resonance frequency of the uniform mode, i.e. $\mathbf{k}=0$. Assuming a simple cubic lattice, there are $z=6$ nearest neighbours. Denoting the lattice constant by a, $\gamma_{\mathbf{k}}$ then becomes

$$\gamma_{\mathbf{k}} = \frac{1}{3}\left(\cos k_x a + \cos k_z a + \cos k_z\right), \tag{2.83}$$

such that the dispersion relation can be expressed as

$$\omega_{\mathbf{k}} = \omega_0 + 4JS\left(3 - (\cos k_x a + \cos k_z a + \cos k_z a)\right). \tag{2.84}$$

This expression may be simplified further in the long wavelength limit, assuming that $k_{x,y,z}a \ll 1$. In this case, the cosines can be Taylor-expanded and we obtain the final result for the magnon dispersion relation,

$$\omega_{\mathbf{k}} \approx \omega_0 + 2JSa^2k^2. \tag{2.85}$$

2.5 Spin-qubits

As presented in the previous section, the QRM theoretically describes the manipulation of any two-level system through a bosonic mode. It has correspondingly received wide attention in the realm of quantum computing, since it in many aspects essentially models all steps in qubit state operations, from initialization to read-out. Being generalized to any two-level systems, there are no restrictions to the type of physical system composing the qubits. Nonetheless, the electron spin is not only the textbook example of a two-level system, the single spin proposal is also attractive because the qubit rotations can be implemented through a Rabi process [58, 59].

The spin-qubit enables the intrinsic spin degree of freedom of a single electron confined in a physical semiconductor quantum dot. It was first suggested by Daniel Loss and David DiVincenzo in 1998, by virtue of its long coherence time and the potential for implementation in larger quantum circuits [60, 61]. Spin-qubits have since been intensely studied to meet the challenges of fault-tolerant quantum computation and at the heart of this research is the ability to control its quantum state. A functional qubit must meet a range of criteria. The first and perhaps most elementary criterion is that the qubits must be reliably initialized and measured. Secondly, the qubit operations have to be successfully implemented by quantum gates. Due to the noisy environment of solid state-based qubits as opposed to atomic, molecular or optical based qubits, spin-qubits are prone to degradation and decoherence.

However, the implementation of spin-qubits greatly benefits from the already long and well-established research conducted on field-effect transistors and semiconductors, as quantum dots can be integrated using gate electrodes in the same way. They also require the same procedural steps for on-chip integration. Currently, the most promising spin-qubit is based on isotopically purified Silicon to avoid intrinsic nuclear magnetic noise. With this technology, the confined electrons act as if completely isolated in a vacuum, allowing for high independent control [28].

Several methods of spin-qubit manipulation have been developed. By applying short optical pulses, the spin state exhibits a series of coherent Rabi oscillations [62]. The spin transition can also be coherently driven by tuning an applied magnetic field resonantly to the energy difference between the spin-up and spin-down states [28, 59]. Contrary to modern day electronics which all depend on the same silicon-based circuit technology, emerging quantum technologies require multiple types of qubit realizations suitable for specific tasks. Nevertheless, silicon based spin-qubits are a promising platform to further develop complex on-chip structures for quantum electronics due to its scalability. This also suggests that the exploration of hybrid systems will be crucial in developing technologies that incorporate properties currently only found in separate realizations.

2.6 Quantum error correction

One of the biggest challenges in realizing fault-tolerant quantum computing is the rapid decoherence of superposition of states, in which the system collapses due to entanglement with the environment, ultimately destroying the ability to conduct

extensive calculations [30]. There is no circumventing this issue, as the utilization of superposition and entanglement is a crucial part of employing the parallelism that make quantum computation superior to classical computation, specifically in solving previously intractable problems [60].

The path towards fault-tolerant quantum computation does not solely rely on less error-prone qubits, but also on quantum error correction, the quantum analog to classical error correction codes. Although quantum error correction codes are based on classical error correction, the quantum nature of qubits introduce several specific problems that need to be addressed. Firstly, the no-cloning theorem means that the data cannot be copied to help detect errors later. Secondly, measuring the state will collapse the superposition. Thus, successful error correction codes able to detect errors without interfering with the actual state of the computer are critical [63]. Lastly, qubits are not only prone to bit flips but also phase errors, such as $|0\rangle + |1\rangle \rightarrow |0\rangle - |1\rangle$.

A powerful error correction code is the Shor nine-qubit code developed by P. W. Shor in 1995 [30]. This code is based on the idea of extending the Hilbert space beyond what is necessary to store a single qubit of information, here by adding an additional eight qubits for redundancy. Each logical state is encoded as three blocks of three-qubit states,

$$\begin{aligned} |0\rangle \rightarrow |0\rangle_L &\equiv \frac{1}{2\sqrt{2}}\big(|000\rangle + |111\rangle\big)\big(|000\rangle + |111\rangle\big)\big(|000\rangle + |111\rangle\big) \\ |1\rangle \rightarrow |1\rangle_L &\equiv \frac{1}{2\sqrt{2}}\big(|000\rangle - |111\rangle\big)\big(|000\rangle - |111\rangle\big)\big(|000\rangle - |111\rangle\big). \end{aligned} \tag{2.86}$$

where each individual three-qubit block consists of the paradigmatic maximally entangled GHZ state,

$$|\mathrm{GHZ}\rangle = \frac{|000\rangle + |111\rangle}{2}, \tag{2.87}$$

and its phase-flipped counterpart [31]. A qubit flip error can be detected by comparing the potential erroneous qubit with the two other qubits in the block, while a phase error is detected by comparing the signs of the other two blocks. This error correction scheme can therefore correct for any finite rotation of a qubit state, provided that the error only occurs within one of the nine qubits [19, 63]. As is clear from this correction scheme, encoding the Shor nine-qubit code into a quantum circuit is largely contingent on the effective generation of three-qubit GHZ states.

3 Magnon|spin-qubit ensemble

In the search for quantum systems suitable for performing large scale quantum information processing, a plethora of different disciplines in physics have been investigated. In atomic, molecular and optical physics, systems based on trapped ions have been found to exhibit effortless state preparation and measurement. In cavity quantum electrodynamics, system dynamics are controlled through electromagnetic radiation with a high degree of precision [19, 27]. There has also been rapid progress in achieving higher and higher coupling rates, which govern the strength of the interaction between each subsystem. In essence, these systems closely resemble a completely isolated qubit, crucial in avoiding detrimental entanglement to the environment.

However, they do not pose as good options for implementation of large-scale quantum networks. To ensure completely fault-tolerant computing, an error rate of less than 1% is necessary, with a redundancy of a thousand physical qubits to encode a single robust qubit [28]. On the other hand, solid state systems benefit from decades of study on miniaturization, fitting multiple qubits onto a nanofabricated circuit. This is nonetheless at the expense of a noisy environment, thereby making it difficult to evade imminent decoherence of the fragile qubit states. In other words, each discipline has its advantages and disadvantages.

A prospected resolution to this issue is to develop hybrid systems combining scalability and control, incorporating the best features of both technologies. In this chapter such a hybrid system consisting of a ferromagnet exchange-coupled to a spin-qubit is proposed. The system Hamiltonian is derived for each of the individual subsystems, as well as the interaction Hamiltonian by considering a ferromagnet/metal interface. Capitalizing from the well-established squeezed state concept of quantum optics, an intuitive physical picture of the magnon eigenmodes of an anisotropic ferromagnet in terms of squeezed spin-1 Fock states is developed. The qualitative differences between squeezed states of light and squeezed magnon states are also discussed. The squeezed basis is then used to theoretically demonstrate an anisotropic QRM with individually tunable rotating and counter-rotating terms.

3.1 The system Hamiltonian

The total system is composed of an insulating ferromagnet coupled to a spin-qubit, where in the terminology of the QRM, the ferromagnet acts as a magnonic cavity and the spin-qubit embodies the two-level system. Experimentally, this system can be imagined as a ferromagnetic thin film layer on top of which is directly deposited conducting strips that host the electron gas comprising the spin-qubit, as depicted in Fig. 3.1. For our platform, the heterostructure governs interfacial exchange-mediated coupling between the magnons

and conduction electrons through direct contact.

The total Hamiltonian of the system consists of the two subsystems, as well as an interaction term. Considering first the bosonic mode, we initially assume the insulating ferromagnet to be isotropic and modelled by a nearest neighbour exchange-coupling. It is subjected to a magnetic field $H_0\hat{\mathbf{z}}$ with an equilibrium magnetization saturated in the $-\hat{\mathbf{z}}$-direction. The Hamiltonian can then be derived in terms of the Heisenberg model,

$$\hat{H}_F = -J\sum_{i,\boldsymbol{\delta}} \hat{\mathbf{S}}_i \cdot \hat{\mathbf{S}}_{i+\boldsymbol{\delta}} + \left|\gamma\right|\mu_0 H_0 \sum_i \hat{S}_{iz}, \tag{3.1}$$

where the first term is the exchange-coupling and the second term is the Zeeman energy. Following the exact procedure presented in Sec. 2.4.1, after employing the Holstein-Primakoff approximation and switching to Fourier space, the Hamiltonian reads

$$\hat{H}_F = \sum_{\mathbf{k}} \omega_{\mathbf{k}} \hat{a}^\dagger_{\mathbf{k}} \hat{a}_{\mathbf{k}}, \tag{3.2}$$

where the magnon dispersion relation for the magnon mode with wavevector $\mathbf{k}$, is $\omega_{\mathbf{k}} = \omega_0 + 4JS\big(3 - (\cos k_x a + \cos k_z a + \cos k_z a)\big)$ and thus depends on the external field, the exchange parameter J, the spin S and the lattice parameter a.

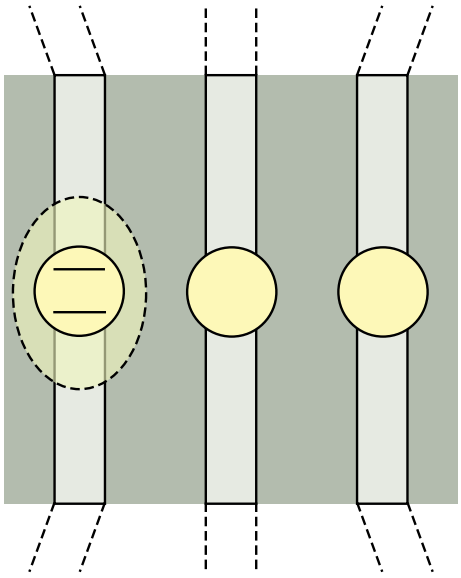

Figure 3.1: Schematic depiction of a magnon|spin-qubit ensemble. The vertical lines represent conducting strips hosting the electronic states embodying the spin-qubits (yellow spheres). The dashed lines represent the external contacts that control the charge carriers in the strips. The spin-qubits are deposited on an thin layer of insulating ferromagnetic material.

We consider next the qubit subsystem, chosen to be in the form of a semiconducting quantum dot with localized states constituting a spin-qubit. As discussed in Sec. 2.5, silicon-based qubits are optimal platforms for processing quantum information as they can be isotopically purified, leading to long decoherence times. They are also based on an already well-established fabrication technology. The semiconductor quantum dot essentially works akin to a field-effect transistor, where the temperature is low enough that

it is only occupied by a discrete number of electrons and all orbital motion is frozen [28]. For this discussion, we consider the spin-qubit to be a confined electron gas controlled such that it consists of a single electronic orbital acting as a two-level system. With the basis states being the spin up and spin down states, the Hamiltonian can be expressed as

$$\hat{H}_q = \text{const.} + \frac{\omega_q}{2}\left(\hat{c}_\uparrow^\dagger \hat{c}_\uparrow - \hat{c}_\downarrow^\dagger \hat{c}_\downarrow\right), \tag{3.3}$$

where $\hat{c}_{\uparrow,\downarrow}^\dagger$ and $\hat{c}_{\uparrow,\downarrow}$ are the fermionic creation and annihilation operators for the spin-up and -down state and the number operator $\hat{n}_{\uparrow,\downarrow} = \hat{c}_{\uparrow,\downarrow}^\dagger \hat{c}_{\uparrow,\downarrow}$ counts the number of electrons in each spin projection, respectively. With an applied magnetic field in the $\hat{\mathbf{z}}$-direction and a negative gyromagnetic ratio, γ, the qubit degeneracy is lifted with a splitting $\omega_q > 0$ between the spin-up and -down states. The constant energy term will not be of importance in the subsequent discussion. The bilinear fermion operators can be redefined in terms of the notation

$$\hat{\sigma}_z \equiv \hat{c}_\uparrow^\dagger \hat{c}_\uparrow - \hat{c}_\downarrow^\dagger \hat{c}_\downarrow \equiv \begin{pmatrix}\hat{c}_\uparrow^\dagger & \hat{c}_\downarrow^\dagger\end{pmatrix}\begin{pmatrix}1 & 0\\ 0 & -1\end{pmatrix}\begin{pmatrix}\hat{c}_\uparrow\\ \hat{c}_\downarrow\end{pmatrix} \equiv \underline{\hat{c}}^\dagger \underline{\sigma}_z \underline{\hat{c}} \tag{3.4}$$

where the underline represents a matrix. The Hamiltonian of Eq. (3.3) may then in turn be rewritten in terms of the new notation as

$$\hat{H}_q = \frac{\omega_q}{2}\hat{\sigma}_z. \tag{3.5}$$

Following this notation, $\hat{\sigma}_x$ and $\hat{\sigma}_y$ are defined by the following relations

$$\begin{aligned}
\hat{\sigma}_x &\equiv \underline{\hat{c}}^\dagger \underline{\sigma}_x \underline{\hat{c}} \equiv \begin{pmatrix}\hat{c}_\uparrow^\dagger & \hat{c}_\downarrow^\dagger\end{pmatrix}\begin{pmatrix}0 & 1\\ 1 & 0\end{pmatrix}\begin{pmatrix}\hat{c}_\uparrow\\ \hat{c}_\downarrow\end{pmatrix} \equiv \hat{c}_\uparrow^\dagger \hat{c}_\downarrow + \hat{c}_\downarrow^\dagger \hat{c}_\uparrow \\
\hat{\sigma}_y &\equiv \underline{\hat{c}}^\dagger \underline{\sigma}_y \underline{\hat{c}} \equiv \begin{pmatrix}\hat{c}_\uparrow^\dagger & \hat{c}_\downarrow^\dagger\end{pmatrix}\begin{pmatrix}0 & -i\\ i & 0\end{pmatrix}\begin{pmatrix}\hat{c}_\uparrow\\ \hat{c}_\downarrow\end{pmatrix} \equiv i(\hat{c}_\downarrow^\dagger \hat{c}_\uparrow - \hat{c}_\uparrow^\dagger \hat{c}_\downarrow),
\end{aligned} \tag{3.6}$$

and $\hat{\sigma}^\pm = \frac{1}{2}(\hat{\sigma}_x \pm i\hat{\sigma}_y)$ follows straightforwardly.

The transfer of spin current across the interface of a magnet-metal bilayer has garnered great interest in the past years for its potential application in spintronic devices. Here, the interconversion of angular momentum between the conduction electrons and magnons occur through the so-called spin-pumping and spin-transfer torque mechanisms. It has been shown for insulating magnets that spin-transfer can be entirely ascribed to magnons, as decay is usually due to conduction electrons. Spin currents can therefore persist for much greater distances in insulating as opposed to non-insulating magnets [64–66]. As the conducting strips hosting the spin-qubits are deposited directly on the ferromagnetic thin film, the interaction between localized moments and electrons can be modelled as an interfacial exchange-coupling with Hamiltonian

$$\hat{H}_{\text{int}} = J_{\text{int}} \sum_l \hat{\mathbf{S}}_l \cdot \hat{\mathbf{s}}_l, \tag{3.7}$$

where $\hat{\mathbf{S}}_l$ and $\hat{\mathbf{s}}_l$ denote the ferromagnetic and qubit spin operators, respectively. The lattice of the ferromagnet is assumed to be overlapping with the spin-qubit such that l labels each site, running over the entire interface. J_{int} is the coupling constant parametrizing

the exchange interaction. Following the procedure described in Sec. 2.4 and employing Eq. (2.67) for both spin operators, the Hamiltonian may be rewritten as

$$\hat{H}_{\text{int}} = J_{\text{int}} \sum_l \Big[\frac{1}{2} \big(\hat{S}_l^+ \hat{s}_l^- + \hat{S}_l^- \hat{s}_l^+ \big) + \hat{S}_{lz} \hat{s}_{lz} \Big]. \tag{3.8}$$

Focusing on the spin operators of the qubit, the local quantum field operators acting on position $\mathbf{r}$ are represented as a complete sum of eigenstates

$$\begin{aligned} \hat{\Psi}_s(\mathbf{r}) &= \sum_t \psi_t(\mathbf{r}) \hat{c}_{ts} \\ \hat{\Psi}_s^\dagger(\mathbf{r}) &= \sum_t \psi_t^*(\mathbf{r}) \hat{c}_{ts}^\dagger. \end{aligned} \tag{3.9}$$

The ladder operators $\hat{\Psi}_s(\mathbf{r})$ and $\hat{\Psi}_s^\dagger(\mathbf{r})$ act to annihilate or create an electron in the state $\psi_t(\mathbf{r})$ at position $\mathbf{r}$, the spatial wavefunction of the orbital labeled by index t, where s denotes the spin projection. The wavefunction $\psi_t(\mathbf{r})$ captures the orbital dynamics of the conducting layer and may be modelled by plane-waves in the most elementary case [65]. The total spin operator at position $\mathbf{r}$ is then further expressed through the ladder operators,

$$\hat{\mathbf{s}}(\mathbf{r}) = \sum_{s,s'=\uparrow,\downarrow} \hat{\Psi}_s^\dagger(\mathbf{r}) \mathbf{s}_{ss'} \hat{\Psi}_{s'}(\mathbf{r}) = \frac{1}{2} \sum_{s,s'=\uparrow,\downarrow} \hat{\Psi}_s^\dagger(\mathbf{r}) \boldsymbol{\sigma}_{ss'} \hat{\Psi}_{s'}(\mathbf{r}), \tag{3.10}$$

where $\boldsymbol{\sigma}$ denotes the vector of Pauli matrices, $\boldsymbol{\sigma} = \sigma_x \hat{\mathbf{x}} + \sigma_y \hat{\mathbf{y}} + \sigma_z \hat{\mathbf{z}}$. Inserting Eq. (3.9) the total spin operator becomes [67],

$$\hat{\mathbf{s}}(\mathbf{r}) = \frac{1}{2} \sum_{s,s',t,t'} \psi_t^*(\mathbf{r}) \psi_{t'}(\mathbf{r}) \boldsymbol{\sigma}_{ss'} \hat{c}_{ts}^\dagger \hat{c}_{t',s'}. \tag{3.11}$$

As only a specific set of energy levels are of interest for the spin-qubit, the index t is omitted, allowing only one set of complete orbitals. In keeping with the notation of Eq. (3.4), the total spin operator may be simplified as,

$$\hat{\mathbf{s}}(\mathbf{r}) = \frac{1}{2} \sum_{s,s'} \big|\psi(\mathbf{r})\big|^2 \boldsymbol{\sigma}_{ss'} \hat{c}_s^\dagger \hat{c}_{s'} = \frac{\big|\psi(\mathbf{r})\big|^2}{2} \underline{\hat{c}}^\dagger \underline{\boldsymbol{\sigma}} \underline{\hat{c}}, \tag{3.12}$$

which in interchanging the position $\mathbf{r}$ for the lattice site index l, becomes

$$\hat{\mathbf{s}}_l = \frac{\big|\psi_l\big|^2}{2} \underline{\hat{c}}^\dagger \underline{\boldsymbol{\sigma}} \underline{\hat{c}}. \tag{3.13}$$

The wave-function ψ_l now represents the qubit orbital situated on interfacial lattice site l. The spin-qubit excitation and relaxation operators accordingly become

$$\hat{\mathbf{s}}_l^\pm = \frac{\big|\psi_l\big|^2}{2} \underline{\hat{c}}^\dagger (\underline{\sigma}_x \pm i \underline{\sigma}_y) \underline{\hat{c}} = \big|\psi_l\big|^2 \underline{\hat{c}}^\dagger \underline{\hat{\sigma}}^\pm \underline{\hat{c}}. \tag{3.14}$$

The Hamiltonian of Eq. (3.8) may now be expressed in terms of the definition of the qubit spin operators, Eqs. (3.13) and (3.14), and the ferromagnetic spin operators can be

reformulated through the magnon operators using the Holstein-Primakoff approximation and switching to Fourier space, employing Eqs. (2.73), (2.70) and (2.77). Splitting the interaction Hamiltonian into two contributing terms, the first contribution reads

$$\begin{aligned}\hat{H}_{\text{int1}} &= \frac{J_{\text{int}}}{2}\sum_l (\hat{S}_l^+ \hat{s}_l^- + \hat{S}_l^- \hat{s}_l^+) \\ &= J_{\text{int}}\sqrt{\frac{S}{2}}\sum_l |\psi_l|^2 \left(\hat{a}_l^\dagger \hat{\sigma}^- + \hat{a}_l \hat{\sigma}^+\right) \\ &= J_{\text{int}}\sqrt{\frac{S}{2N_F}}\sum_{l,\mathbf{k}} |\psi_l|^2 \left(\hat{a}_{\mathbf{k}}^\dagger e^{i\mathbf{k}\mathbf{r}_l}\hat{\sigma}^- + \hat{a}_{\mathbf{k}} e^{-i\mathbf{k}\mathbf{r}_l}\hat{\sigma}^+\right).\end{aligned} \tag{3.15}$$

Retaining only the spatially uniform magnon mode, ($\mathbf{k} = 0$), without loosing essential features, this can be simplified to

$$\hat{H}_{\text{int1}} = g(\hat{a}_{\mathbf{0}}^\dagger \hat{\sigma}^- + \hat{a}_{\mathbf{0}}\hat{\sigma}^+), \quad g = J_{\text{int}} N_{\text{int}} |\psi|^2 \sqrt{\frac{S}{2N_F}} \tag{3.16}$$

where N_{int} is the total number of interfacial sites, and the electronic wavefunction averaged over the interface, $|\psi|^2 \equiv \left(\sum_l |\psi_l|^2\right)/N_{\text{int}}$, has been introduced. The second contribution is

$$\begin{aligned}\hat{H}_{\text{int2}} &= J_{\text{int}}\sum_l \hat{S}_{lz}\hat{s}_{lz} \\ &= J_{\text{int}}\sum_l \frac{|\psi_l|^2}{2}\left(\hat{a}_l^\dagger \hat{a}_l - S\right)\hat{\sigma}_z \\ &\approx -\frac{S J_{\text{int}} N_{\text{int}} |\psi|^2}{2}\hat{\sigma}_z\end{aligned} \tag{3.17}$$

where only interaction terms of quadratic order or less have been retained. The second contribution normalizes the spin-qubit energy and can be absorbed into ω_q of the spin-qubit Hamiltonian given in Eq. (3.5),

$$\hat{H}_q' = \hat{H}_q + \hat{H}_{\text{int2}} = \frac{\omega_q'}{2}\hat{\sigma}_z, \quad \omega_q' = \omega_q - S J_{\text{int}} N_{\text{int}} |\psi|^2 \tag{3.18}$$

in which the primes will hereby be omitted and the interaction Hamiltonian is redefined as $\hat{H}_{\text{int}} = \hat{H}_{\text{int1}}$. We thus obtain for the the total Hamiltonian of the uniform mode

$$\hat{H} = \hat{H}_F + \hat{H}_{\text{int}} + \hat{H}_q = \omega_0 \hat{a}_{\mathbf{0}}^\dagger \hat{a}_{\mathbf{0}} + g(\hat{a}_{\mathbf{0}}^\dagger \hat{\sigma}^- + \hat{a}_{\mathbf{0}}\hat{\sigma}^+) + \frac{\omega_q}{2}\hat{\sigma}_z. \tag{3.19}$$

It is apparent from the form of the Hamiltonian that the magnon|spin-qubit system can be described by an ideal Jaynes-Cummings model, where the interaction conserves the total number of excitations. The uniform magnon mode of the isotropic ferromagnet acts as a single-mode bosonic cavity with cavity frequency ω_0, and the interaction is governed solely by rotating terms.

This is a direct result of the rotational invariance of the exchange-coupling, providing spin conservation. A magnon with spin 1 can be absorbed by the qubit and cause a spin-flip

from the lower -1/2 to +1/2 state, yet a magnon cannot be created from a $-1/2 \rightarrow +1/2$ transition in the qubit, as this would break the conservation of the total number of spins in the system. On the contrary, if the interaction between the spin-qubit and the ferromagnet was dipolar, this would generally result in a standard isotropic QRM exhibiting virtual transitions, as this coupling does not conserve spin. Additionally, the dipolar interaction has an estimated energy of $E_D \approx 10^{-4}\,eV$ and is much weaker than the direct exchange interaction, usually only considered to be an anisotropic effect and a correction [54]. Thus, the effective coupling g of the magnon|spin-qubit ensemble afforded by the exchange interaction is strong enough to surpass the magnon frequency ω_0 and enable a coupling ranging from SC into DSC regimes.

3.2 Equilibrium magnon squeezing

So far only an isotropic ferromagnet has been considered, however as the ferromagnetic material intended for the magnon-qubit system is a thin film, it is expected that the magnetic properties will be directionally dependent from the creation of an easy axis, breaking the rotational symmetry. As a result, additional shape anisotropy contributions must be taken into account, in addition to other potential magnetic anisotropy effects such as single-ion magnetocrystalline or dipolar contributions [54]. The exact form of the magnetic anisotropy depends on the crystal lattice, but must in general be invariant to a change of sign in the spin components to ensure that the ground state still has a uniform magnetization [56]. Without assuming a crystal lattice or specific anisotropy effects, a general Hamiltonian encompassing all types of contributions is of the form

$$\hat{H}_F = -J\sum_{i,\boldsymbol{\delta}} \hat{\mathbf{S}}_i \cdot \hat{\mathbf{S}}_{i+\boldsymbol{\delta}} + \left|\gamma\right|\mu_0 H_0 \sum_i \hat{S}_{iz} + \sum_i \Big[K_x \big(\hat{S}_{ix}\big)^2 + K_y \big(\hat{S}_{iy}\big)^2 + K_z \big(\hat{S}_{iz}\big)^2 \Big], \tag{3.20}$$

where the first and second sums represent the ferromagnetic exchange and Zeeman terms, and the third is the general anisotropic term parametrized by $K_{x,y,z}$. The derivation of the magnonic Hamiltonian in terms of the exchange and Zeeman terms has already been conducted in Sec. (2.4.1), hence the third sum will now be considered separately. Applying Eq. (2.67), the anisotropic term is rewritten as

$$\hat{H}_{\text{an}} = \sum_i \frac{\Delta K}{2} \big[(\hat{S}_i^+)^2 + (\hat{S}_i^-)^2 \big] + \frac{\overline{K}}{2} \big[\hat{S}_i^+ \hat{S}_i^- + \hat{S}_i^- \hat{S}_i^+ \big] + K_z \big(\hat{S}_{iz}\big)^2, \tag{3.21}$$

where the parameters $\Delta K \equiv (K_x - K_y)/2$ and $\overline{K} \equiv (K_x + K_y)/2$ have been introduced. Assuming that the anisotropy dominates the Zeeman energy, all spins still point in the $-\hat{\mathbf{z}}$-direction in the ground state. Inserting the Holstein-Primakoff transformation, Eq. (2.70) and (2.73), and omitting all terms above quadratic order,

$$\hat{H}_{\text{an}} = \text{const.} + \sum_i \Delta K S \big(\hat{a}_i^\dagger \hat{a}_i^\dagger + \hat{a}_i \hat{a}_i \big) + 2S(\overline{K} - K_z)\, \hat{a}_i^\dagger \hat{a}_i, \tag{3.22}$$

where the constant term is $\overline{K} S N_F + K_z S^2 N_F$. Employing the Fourier transform of Eq. (2.77) and summing over all lattice sites i, one then obtains

$$\hat{H}_{\text{an}} = \text{const.} + \sum_{\mathbf{k}} 2\big(\overline{K} - K_z\big)\, \hat{a}_{\mathbf{k}}^\dagger \hat{a}_{\mathbf{k}} + \Delta K \big(\hat{a}_{\mathbf{k}} \hat{a}_{-\mathbf{k}} + \hat{a}_{\mathbf{k}}^\dagger \hat{a}_{-\mathbf{k}}^\dagger \big). \tag{3.23}$$

The total ferromagnetic Hamiltonian now becomes

$$\hat{H}_F = \text{const.} + S\sum_{\mathbf{k}} A_{\mathbf{k}}\hat{a}^\dagger_{\mathbf{k}}\hat{a}_{\mathbf{k}} + B_{\mathbf{k}}\big(\hat{a}_{\mathbf{k}}\hat{a}_{-\mathbf{k}} + \hat{a}^\dagger_{\mathbf{k}}\hat{a}^\dagger_{-\mathbf{k}}\big) \tag{3.24}$$

where the total constant term is $\overline{K}SN_F + K_zS^2N_F - |\gamma|\mu_0H_0SN_F - JS^2N_Fz$ and

$$\begin{aligned} A_{\mathbf{k}} &\equiv 2S(\overline{K} - K_z) + |\gamma|\mu_0H_0 + 4JS\big[3 - (\cos k_x a + \cos k_y a + \cos k_z a)\big], \\ B_{\mathbf{k}} &\equiv \Delta KS. \end{aligned} \tag{3.25}$$

It follows that $A_{\mathbf{k}} = A_{-\mathbf{k}}$ and $B_{\mathbf{k}} = B_{-\mathbf{k}}$. The ensuing Hamiltonian has the characteristic feature of possessing the $\hat{a}_{\mathbf{k}}\hat{a}_{-\mathbf{k}}$ and $\hat{a}^\dagger_{\mathbf{k}}\hat{a}^\dagger_{-\mathbf{k}}$-terms, which can be interpreted as the annihilation and creation of two magnons with wavevector $\pm\mathbf{k}$, similar to the two photon processes found in the case of squeezed states of light. In the manner that these terms lead to quadrature squeezing in light, they lead to magnons of elliptical instead of circular spin fluctuations in a ferromagnet [68].

The mathematical connection between the squeezed states of light and magnon squeezed states, and the significance of the off-diagonal $\hat{a}_{\mathbf{k}}\hat{a}_{-\mathbf{k}}$ and $\hat{a}^\dagger_{\mathbf{k}}\hat{a}^\dagger_{-\mathbf{k}}$-terms, is further elucidated by diagonalizing the Hamiltonian of Eq. (3.24) and employing the framework of squeezed states from quantum optics. Being entirely bilinear in the annihilation and creation operators, the diagonal Hamiltonian can be obtained exactly by a Bogoliubov transformation, defining the new operators through the relations

$$\begin{aligned} \hat{\alpha}_{\mathbf{k}} &= u_{\mathbf{k}}\hat{a}_{\mathbf{k}} - v_{\mathbf{k}}\hat{a}^\dagger_{-\mathbf{k}} \\ \hat{\alpha}^\dagger_{-\mathbf{k}} &= u_{\mathbf{k}}\hat{a}^\dagger_{-\mathbf{k}} - v_{\mathbf{k}}\hat{a}_{\mathbf{k}}, \end{aligned} \tag{3.26}$$

where it has been assumed that both $u_{\mathbf{k}}$ and $v_{\mathbf{k}}$ are real. These operators still need to fulfill the Bose commutator rules such that $\big[\hat{\alpha}_{\mathbf{k}}, \hat{\alpha}^\dagger_{\mathbf{k}'}\big] = \delta_{\mathbf{k},\mathbf{k}'}$, imposing on $u_{\mathbf{k}}$ and $v_{\mathbf{k}}$ the condition

$$u^2_{\mathbf{k}} - v^2_{\mathbf{k}} = 1, \tag{3.27}$$

which additionally ensures that the transformation is unitary [69]. Inserting Eq. (3.26) in terms of the isotropic ladder operators and gathering all equal terms, the anisotropic ferromagnet Hamiltonian reads

$$\hat{H}_F = \sum_{\mathbf{k}}\Big(A_{\mathbf{k}}(u^2_{\mathbf{k}} + v^2_{\mathbf{k}}) + 4B_{\mathbf{k}}u_{\mathbf{k}}v_{\mathbf{k}}\Big)\hat{\alpha}^\dagger_{\mathbf{k}}\alpha_{\mathbf{k}} + \Big(A_{\mathbf{k}}u_{\mathbf{k}}v_{\mathbf{k}} + B_{\mathbf{k}}(u^2_{\mathbf{k}} + v^2_{\mathbf{k}})\Big)\Big[\hat{a}_{\mathbf{k}}\hat{a}_{-\mathbf{k}} + \hat{a}^\dagger_{\mathbf{k}}\hat{a}^\dagger_{-\mathbf{k}}\Big]. \tag{3.28}$$

We observe that this Hamiltonian becomes diagonalized if the following relation is satisfied,

$$A_{\mathbf{k}}u_{\mathbf{k}}v_{\mathbf{k}} + B_{\mathbf{k}}(u^2_{\mathbf{k}} + v^2_{\mathbf{k}}) = 0, \tag{3.29}$$

and by solving this equation, we obtain the final solutions for the coefficients,

$$\begin{aligned} u_{\mathbf{k}} &= \Big(\frac{1}{2} + \frac{1}{2}\frac{A_{\mathbf{k}}}{\sqrt{A^2_{\mathbf{k}} - 4B^2_{\mathbf{k}}}}\Big)^{\frac{1}{2}} \\ v_{\mathbf{k}} &= -\Big(-\frac{1}{2} + \frac{1}{2}\frac{A_{\mathbf{k}}}{\sqrt{A^2_{\mathbf{k}} - 4B^2_{\mathbf{k}}}}\Big)^{\frac{1}{2}}. \end{aligned} \tag{3.30}$$

The signs of $u_{\mathbf{k}}$ and $v_{\mathbf{k}}$ have been chosen to satisfy the original equation. Employing this result, the final Hamiltonian becomes

$$\hat{H}_F = \sum_{\mathbf{k}} \omega_{\mathbf{k}} \hat{\alpha}^\dagger_{\mathbf{k}} \hat{\alpha}_{\mathbf{k}}, \quad \omega_{\mathbf{k}} = \sqrt{A^2_{\mathbf{k}} - 4B^2_{\mathbf{k}}}, \tag{3.31}$$

where $\omega_{\mathbf{k}}$ is the eigenmode frequency. The Bogoliubov transformation also introduces an additional constant term which has been omitted. Now denoting the vacuum state in the new $\alpha_{\mathbf{k}}$-basis and the spin-1 magnon $a_{\mathbf{k}}$-basis as $|0\rangle_{\alpha_{\mathbf{k}}}$ and $|0\rangle_{a_{\mathbf{k}}}$, the relation between the two ground states can be found by applying the mathematical framework of the squeezed states of light. A relation that will be useful here is

$$\hat{S}_2(\xi_{\mathbf{k}}) \hat{a}_{\mathbf{k}} \hat{S}^\dagger_2(\xi_{\mathbf{k}}) = \cosh r_{\mathbf{k}} \hat{a} + e^{i\theta_{\mathbf{k}}} \sinh r_{\mathbf{k}} \hat{a}^\dagger, \tag{3.32}$$

which can be derived straightforwardly using the same procedure as proposed for Eq. (2.28) and where $\hat{S}_2(\xi) = e^{\xi^*_{\mathbf{k}} \hat{a}_{\mathbf{k}} \hat{a}_{-\mathbf{k}} - \xi_{\mathbf{k}} \hat{a}^\dagger_{\mathbf{k}} \hat{a}^\dagger_{-\mathbf{k}}}$ is the two-mode squeeze operator of Eq. (2.33) with $\hat{a} = \hat{a}_{\mathbf{k}}$ and $\hat{b} = \hat{a}_{-\mathbf{k}}$. The relation defining the new vacuum state is

$$\hat{\alpha}_{\mathbf{k}} |0\rangle_{\alpha_{\mathbf{k}}} = \left(u_{\mathbf{k}} \hat{a}_{\mathbf{k}} - v_{\mathbf{k}} \hat{a}^\dagger_{-\mathbf{k}} \right) |0\rangle_{\alpha_{\mathbf{k}}} = 0. \tag{3.33}$$

We can then identify that by setting $u_{\mathbf{k}} = \cosh r_{\mathbf{k}}$ and $v_{\mathbf{k}} = -e^{i\theta_{\mathbf{k}}} \sinh r_{\mathbf{k}}$, $\hat{\alpha}_{\mathbf{k}}$ is the squeezed annihilation operator of the spin-1 magnon excitations,

$$\hat{\alpha}_{\mathbf{k}} = \hat{S}_2(\xi_{\mathbf{k}}) \hat{a}_{\mathbf{k}} \hat{S}^\dagger_2(\xi_{\mathbf{k}}), \tag{3.34}$$

such that Eq. (3.33) becomes

$$\hat{S}_2(\xi_{\mathbf{k}}) \hat{a}_{\mathbf{k}} \hat{S}^\dagger_2(\xi_{\mathbf{k}}) |0\rangle_{\alpha_{\mathbf{k}}} = 0 \tag{3.35}$$

Applying $\hat{S}^\dagger_2(\xi_{\mathbf{k}})$ to the left hand side of this relation and recapitulating that $\hat{a}_{\mathbf{k}} |0\rangle_{\mathbf{k}} = 0$, it follows that

$$\hat{S}^\dagger_2(\xi_{\mathbf{k}}) |0\rangle_{\alpha_{\mathbf{k}}} = |0\rangle_{a_{\mathbf{k}}} \quad \text{and} \quad \hat{S}_2(\xi_{\mathbf{k}}) |0\rangle_{a_{\mathbf{k}}} = |0\rangle_{\alpha_{\mathbf{k}}}. \tag{3.36}$$

Whence, we have shown that the squeezed vacuum $|0\rangle_{\alpha_{\mathbf{k}}}$ is obtained by squeezing the spin-1 magnon vacuum $|0\rangle_{a_{\mathbf{k}}}$, a result originating from the addition of anisotropic contributions to the ferromagnet. The total ground state becomes

$$|G\rangle_{\alpha_{\mathbf{k}}} = \left(\prod_{\mathbf{k}} \hat{S}(\xi_{\mathbf{k}}) \right) |0\rangle_{\hat{a}_{\mathbf{k}}}, \tag{3.37}$$

and the value of the squeezing parameter, $r_{\mathbf{k}}$, is determined through the relation

$$\cosh r_{\mathbf{k}} = \left(\frac{1}{2} + \frac{1}{2} \frac{A_{\mathbf{k}}}{\sqrt{A^2_{\mathbf{k}} - 4B^2_{\mathbf{k}}}} \right)^{\frac{1}{2}}, \tag{3.38}$$

meaning the degree of squeezing can be conveniently engineered through the applied magnetic field and ferromagnet anisotropies. Without the anisotropic contributions, the eigenmodes of the system would return to the spin-1 magnon Fock states in the $\hat{a}_{\mathbf{k}}$ basis [37].

To derive the explicit dependence of the two-mode quadratures in terms of the observables of our system, the operators $a_{\mathbf{k}}$ and $a_{-\mathbf{k}}$ must be rewritten in terms of the spin

operators. By employing the reverse Fourier and Holstein-Primakoff transformations on Eq. (2.33), we obtain the relations

$$\begin{aligned}\hat{X}_1 &= \frac{1}{2\sqrt{N_F S}}\left(\hat{S}_{x,\mathbf{k}} + \hat{S}_{x,-\mathbf{k}}\right),\\ \hat{X}_2 &= -\frac{1}{2\sqrt{N_F S}}\left(\hat{S}_{y,\mathbf{k}} + \hat{S}_{y,-\mathbf{k}}\right).\end{aligned} \tag{3.39}$$

The indexes $\pm\mathbf{k}$ denote the two types of modes, and the unconventional minus sign of $\hat{X}_2$ results from the choice of the ground state pointing in the $-\hat{\mathbf{z}}$-direction. In contrast to squeezed states of light, which are a non-equilibrium phenomenon, the magnon squeezing is a result of intrinsic minimization of the ground state energy while obeying the Heisenberg principle. In accordance with the commutation relation of spin operator components, see Eq. (2.66), the spin cannot be perfectly aligned to the z-direction as this would necessitate the uncertainty in the x and y-components of the spin vanishing. Hence, the ground state of the system still exhibits small fluctuations in the $x-y$-plane afforded by the Heisenberg principle, with a geometrically constrained uncertainty region as depicted in Fig. 3.2 [38]. For the distinct case of the uniform mode, the quadratures are simply proportional to the $\hat{S}_x$ and $\hat{S}_y$ components of the spin. Subsequently, the spin fluctuations can be depicted as elliptical with the uncertainty of one observable reduced at the expense of an enlarged uncertainty in the other observable. This process is equilibrium in nature as a result of minimizing the energy. The shape of the ellipse depends on the anisotropy and which magnetization direction manifest a higher energy cost.

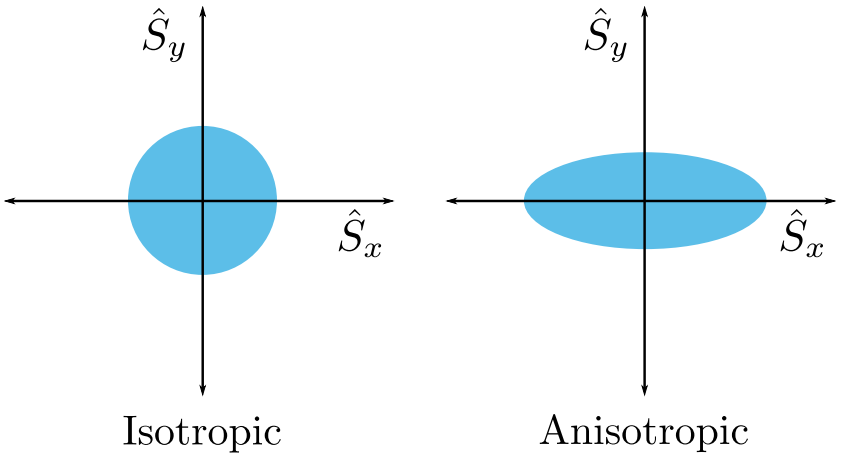

Figure 3.2: Isotropic (left) and anisotropic (right) Heisenberg uncertainty regions for spin saturation in the z-direction, for the uniform mode. In the isotropic ferromagnet the quantum fluctuations are circular, while they in the presence of anisotropy become elliptical. The ellipse has its minor axis in the y-direction, depicting squeezing at the expense of larger fluctuations in the x-direction. The figure has been adapted from Ref. [38].

The squeezed magnons can not only be determined in terms of the vacuum, but also through the squeezing of the spin-1 magnon number states. The squeezed eigenexcitation is defined through the single spin-flip state as

$$|1\rangle_{\alpha_\mathbf{k}} = \hat{S}(\xi_\mathbf{k})|1\rangle_{\hat{a}_\mathbf{k}}. \tag{3.40}$$

For the sake of simplicity, the subsequent discussion will be working in the spatially uniform mode, $\mathbf{k} = 0$, such that $\hat{\alpha}_{\mathbf{k}} = \hat{\alpha}_{-\mathbf{k}} = \hat{\alpha}_{\mathbf{0}}$. As a result, the squeezing effect can be limited to a single-mode, however the extension to two modes does not alter the physics significantly. The disentangled squeeze operator has the form [70, 71],

$$\hat{S}(\xi_{\mathbf{0}}) = e^{-\frac{1}{2}e^{i\theta_{\mathbf{0}}}\tanh r_{\mathbf{0}}\hat{a}_{\mathbf{0}}^{\dagger}\hat{a}_{\mathbf{0}}^{\dagger}}\operatorname{sech} r_{\mathbf{0}}^{\frac{1}{2}+\hat{a}_{\mathbf{0}}^{\dagger}\hat{a}_{\mathbf{0}}}e^{\frac{1}{2}e^{i\theta_{\mathbf{0}}}\tanh r_{\mathbf{0}}\hat{a}_{\mathbf{0}}\hat{a}_{\mathbf{0}}}. \tag{3.41}$$

Setting $d = \frac{1}{2}e^{-i\theta_{\mathbf{0}}}\tanh r_{\mathbf{0}}$, the squeezed magnon in terms of an arbitrary state $|n\rangle_{a_{\mathbf{0}}}$ with n magnons is

$$\begin{aligned}
\hat{S}(\xi_{\mathbf{0}})|n\rangle_{a_{\mathbf{0}}} &= e^{-d\hat{a}_{\mathbf{0}}^{\dagger}\hat{a}_{\mathbf{0}}^{\dagger}}\operatorname{sech} r_{\mathbf{0}}^{\frac{1}{2}+\hat{a}_{\mathbf{0}}^{\dagger}\hat{a}_{\mathbf{0}}}e^{d^{*}\hat{a}_{\mathbf{0}}\hat{a}_{\mathbf{0}}}|n\rangle_{a_{\mathbf{0}}} \\
&= \sum_{m=0}^{\infty}\frac{(-d\hat{a}_{\mathbf{0}}^{\dagger}\hat{a}_{\mathbf{0}}^{\dagger})^{m}}{m!}\operatorname{sech} r_{\mathbf{0}}^{\frac{1}{2}+\hat{a}_{\mathbf{0}}^{\dagger}\hat{a}_{\mathbf{0}}}\sum_{l=0}^{\infty}\frac{(d^{*}\hat{a}_{\mathbf{0}}\hat{a}_{\mathbf{0}})^{l}}{l!}|n\rangle_{a_{\mathbf{0}}} \\
&= \sum_{m=0}^{\infty}\frac{(-d\hat{a}_{\mathbf{0}}^{\dagger}\hat{a}_{\mathbf{0}}^{\dagger})^{m}}{m!}\operatorname{sech} r_{\mathbf{0}}^{\frac{1}{2}+\hat{a}_{\mathbf{0}}^{\dagger}\hat{a}_{\mathbf{0}}}\sum_{l=0}^{[n/2]}\sqrt{\frac{n!}{(n-2l)!}}\frac{(d^{*})^{l}}{l!}|n-2l\rangle_{a_{\mathbf{0}}} \\
&= \operatorname{sech} r_{\mathbf{0}}^{n-2l+\frac{1}{2}}\sqrt{n!}\sum_{m=0}^{\infty}\sum_{l=0}^{[n/2]}(d^{*})^{l}(-d)^{m}\frac{\sqrt{(n-2l+2m)!}}{(n-2l)!l!m!}|n-2l+2m\rangle_{a_{\mathbf{0}}},
\end{aligned} \tag{3.42}$$

where $[\frac{n}{2}]$ is the greatest integer function. Thus, the squeezed magnon vacuum with $n = 0$ and $l = 0$, is comprised of a superposition of even spin-1 magnon number states. For the first eigenexcitation, $n = 1$ and $l = 0$, resulting in a coherent superposition of odd-numbered magnon states, as depicted in Fig. 3.3. To see the implications of this, it is of interest to calculate the average number of magnons in the squeezed vacuum state. We obtain

$$\begin{aligned}
\langle 0|\hat{a}_{\mathbf{0}}^{\dagger}\hat{a}_{\mathbf{0}}|0\rangle_{\alpha_{\mathbf{0}}} &= \langle 0|\hat{S}^{\dagger}(\xi_{\mathbf{0}})\hat{a}_{\mathbf{0}}^{\dagger}\hat{S}^{\dagger}(\xi_{\mathbf{0}})\hat{S}(\xi_{\mathbf{0}})\hat{a}_{\mathbf{0}}\hat{S}(\xi_{\mathbf{0}})|0\rangle_{a_{\mathbf{0}}} \\
&= \langle 0|\big(\cosh r_{\mathbf{0}}\hat{a}_{\mathbf{0}}^{\dagger} - e^{-i\theta_{\mathbf{0}}}\sinh r_{\mathbf{0}}\hat{a}_{\mathbf{0}}\big)\big(\cosh r_{\mathbf{0}}\hat{a}_{\mathbf{0}} - e^{i\theta_{\mathbf{0}}}\sinh r_{\mathbf{0}}\hat{a}_{\mathbf{0}}^{\dagger}\big)|0\rangle_{a_{\mathbf{0}}} \\
&= \sinh^{2} r_{\mathbf{0}},
\end{aligned} \tag{3.43}$$

where Eq. (2.28) was used in the second line. Thus, the average number of magnons in the squeezed magnon vacuum for the uniform mode is $\langle 0|\hat{a}_{\mathbf{0}}^{\dagger}\hat{a}_{\mathbf{0}}|0\rangle_{\alpha_{\mathbf{0}}} = \sinh^{2} r_{\mathbf{0}} = |v_{\mathbf{0}}|^{2}$. This in return means that the average spin of the squeezed magnons is non-integer and is highly dependent on the degree of squeezing through $r_{\mathbf{0}}$. The average spin is therefore potentially much larger than 1, in contrast to the spin-1 magnon.

3.3 Tunable anisotropic quantum Rabi model

Ensuing from our results above, our system can be described in terms of two different bases. The spin-1 magnon base, represented by $\hat{a}_{\mathbf{k}}$ and the squeezed magnon base represented by $\hat{\alpha}_{\mathbf{k}}$. The latter is also the eigenmode of the system, where the squeezed single magnon state, otherwise known as the first eigenexcitation but hereby dubbed simply as the squeezed magnon, comprises a superposition of odd magnon number states. As previously discussed, the spin-1 magnon basis is directly associated with spin-flips in the magnet such that the interaction exclusively comprises rotating terms, see Eq. (3.19). The interaction is limited

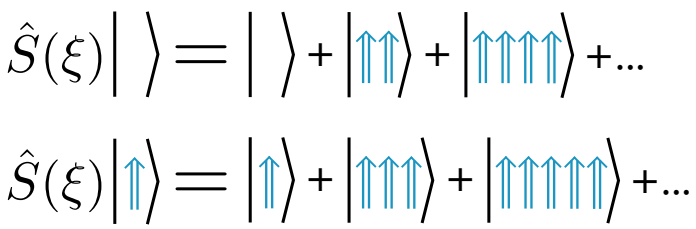

Figure 3.3: Schematic depiction of the squeezed magnon vacuum and eigenexcitation, where the application of the squeeze operator $\hat{S}(\xi)$ to the vacuum or first excited state of the spin-1 magnon mode leads to a superposition of even and odd magnon states, respectively. These are the ground state and first eigenexcitation of the anisotropic ferromagnet. An empty ket represents a fully saturated ground state, while a ket with a single arrow represents a single magnon state. The figure has been adapted from Ref. [38].

to excitation number conserving absorption and emission processes, in agreement with an ideal Jaynes-Cummings model.

Discussing the squeezed basis in terms of the QRM, all essential physics are still captured in the spatially uniform mode. Thus, only the $\mathbf{k} = 0$ mode will be considered, and $\hat{a}_{\mathbf{0}}$, $\hat{\alpha}_{\mathbf{0}}$ and $r_{\mathbf{0}}$ will simply be denoted as $\hat{a}$, $\hat{\alpha}$ and r henceforth. Likewise, the corresponding Bogoliubov transformation is in this case $\hat{\alpha} = \cosh r\,\hat{a} - \sinh r\,\hat{a}^\dagger$, where the squeezing angle $\theta_{\mathbf{0}}$ has been set to zero. Transforming the total system into the squeezed magnon basis, one achieves the final Hamiltonian

$$\hat{H} = \omega_0 \alpha^\dagger \alpha + g_R(\sigma^- \hat{a}^\dagger + \sigma^+ \hat{a}) + g_{CR}(\sigma^+ \hat{a}^\dagger + \sigma^- \hat{a}) + \frac{\omega_q}{2}\sigma_z, \tag{3.44}$$

where $g_R = g\cosh r$ and $g_{CR} = g\sinh r$. Therefore, the system is consistent with an anisotropic QRM in the eigenbasis, in the sense that the coupling strength of the excitation number conserving and non-conserving terms can be individually tuned.

The anisotropic QRM is a generalization, leading to the Jaynes-Cummings model if $g_{CR} = 0$ and to the standard QRM if $g_R = g_{CR}$. This model was first investigated in the context of the multi-qubit Dicke model, and has since been paid great theoretical and experimental interest [72, 73]. With the ability to individually tune the coupling strength of the rotating and counter-rotating terms, our magnon|spin-qubit ensemble grants an advantageous platform for experimentally investigating the intermediate dynamics of the QRM in various parameter regimes. This also provides the opportunity of achieving predictable classical behavior in the USC regime. In terms of quantum information, implementation schemes allowing generation of Schrödinger cat states and quantum controlled phase gates have been investigated [74]. Several experimental realizations of the anisotropic QRM have also been proposed, such as superconducting flux qubits in circuit quantum electrodynamics [25]. However, many proposals afford limited parametric range or are dependent on an external non-equilibrium drive [74].

Contrarily, the proposed magnon|spin-qubit ensemble is a promising platform for experimentally realizing the anisotropic QRM, owing to its equilibrium nature. The separate control of the rotating and counter-rotating terms is a direct consequence of intrinsic squeezing emerging from energy minimization. Thus, the different coupling strengths can

be engineered through the squeeze parameter r, which again for the proposed system is controllable through the applied magnetic field and anisotropies in the ferromagnet. Furthermore, owing to the eigenmodes comprising a superposition of odd magnon states, the squeezed magnon has with a significant amount of squeezing introduced to the system, a non-integer spin larger than 1, as proved in Eq. (3.43). This additionally leads to an enhancement in the exchange-coupling to excitations in the qubit, without requiring a non-equilibrium drive [75, 76]. In other words, this hybrid system harnesses the advantages of being a solid-state platform while exploiting the valuable features of the squeezed state concept, capitalizing on two different technologies.

4 Synchronous three-qubit excitation

The generation of multipartite entangled states is paramount in achieving fault-tolerant large-scale quantum computation and is an indispensable resource in quantum information research. They have been generated using a variety of schemes, such as applying superconducting phase qubits or employing multi-photon exchange in USC cavity quantum electrodynamics [16, 77]. Of special interest are the maximally entangled GHZ states, stemming from their central role in implementing Shor's nine-qubit quantum error correction protocol, as described in Sec. 2.6. However, the conventional way of generating GHZ states is by step-wise operations of two-qubit gates, applying qubit rotations, synchronous driving into resonance, exact pulses and so forth, inevitably suffering from cumulative errors and complexity. Furthermore, state preparations based on probabilistic methods rapidly fail to accommodate even higher multi-qubit states [78].

It is well known that a qubit strongly coupled to a bosonic mode can exchange a single photon in a coherent and reversible Rabi oscillation, as discussed in Sec. 2.3, providing a manner in which quantum states can be precisely manipulated. With the experimental realization of the USC and DSC regimes however, new and novel phenomena of light-matter interaction could be investigated. In these coupling regimes, the dynamics are not strictly contained within each two-dimensional subspace of the Jaynes-Cummings model, as described in Sec. 2.3.1. Due to the rotating-wave approximation breaking down, the counter-rotating terms of the QRM govern higher-order transitions between states that do not conserve the number of excitations. These types of transitions have been under recent investigation, in which it was found that by tuning the cavity mode and qubit frequencies, one can achieve a resonant coupling between states that are connected through virtual intermediate states. Consequently, enabling joint emission and absorption of multiple photons by a coherent and reversible Rabi process [16–18].

In this and the subsequent chapter, we provide an analysis of the three-qubit resonant transition between the states $|1, ggg\rangle$ and $|0, eee\rangle$ for our magnon|spin-qubit ensemble. The transition in question is thus one squeezed magnon exciting three qubits. We therefore extend our tunable anisotropic QRM to comprise three qubits and one squeezed magnon mode, where in the terminology of the QRM, the squeezed magnon acts as the cavity field mode. We study this transition with the intention of proposing an alternative method for one-step concurrent qubit excitation using the coupling enhanced magnon|spin-qubit ensemble, and thus establishing a robust method of generating GHZ states. The primary purpose of this chapter is the theoretical investigation of the transition of interest by the derivation of an effective Hamiltonian and thus the amplitude of the transition, evaluated using third-order and fifth-order perturbation theory.

4.1 The anisotropic quantum Rabi model: One squeezed magnon coupled to three qubits

With the objective of demonstrating robust generation of GHZ states, our magnon|spin-qubit model is extended to encompass a single squeezed magnon eigenmode coupled to three qubits. For typical values of the exchange parameter J and with lateral dimensions in the μm range, the ferromagnetic thin film that is the base of the spin-qubit conducting strips will have a quantized magnon spectrum. Considering that the only interactions that will be evaluated for the problem at hand are resonant coherent transitions, only the spatially uniform mode needs to be treated as the energy levels in the magnon spectrum will be sufficiently separated by approximately a few GHz. The extended anisotropic QRM then reads

$$\hat{H}_3 = \omega_0 \hat{\alpha}^\dagger \alpha + \sum_{n=1,2,3} \left[g_{Rn}\left(\hat{\alpha}^\dagger \hat{\sigma}_n^- + \hat{\alpha}\hat{\sigma}_n^+\right) + g_{CRn}\left(\hat{\alpha}^\dagger \hat{\sigma}_n^+ + \hat{\alpha}\hat{\sigma}_n^-\right) + \frac{\omega_{qn}}{2}\hat{\sigma}_{z,n} \right], \tag{4.1}$$

where n addresses each individual qubit. A schematic illustrating how the standing wave of the squeezed magnon mode interacts individually with each of the three qubits through rotating and counter-rotating processes, is depicted in Fig. 4.1. The spin-down ground and spin-up excited states of the qubit will be denoted $|g\rangle$ and $|e\rangle$, consistently with the QRM formalism presented in Sec. 2.3, and correspond to the $|0\rangle$ and $|1\rangle$-states used in Shor's nine-qubit code.

As the anisotropic QRM with three qubits essentially contains all the same terms as the standard QRM, the Hamiltonian conserves the global parity operator and it inherently exhibits a parity symmetry [79]. With the total excitation number operator $\hat{N} = \hat{\alpha}^\dagger\hat{\alpha} + \sum_{n=1,2,3}\hat{\sigma}_n^+\hat{\sigma}_n^-$, the global parity operator is easily calculated following the procedure of Eq. (2.49),

$$\begin{aligned}
\Pi_{\mathrm{AQRM}} &= e^{i\pi\hat{\alpha}^\dagger\hat{\alpha}} \times \prod_{n=1,2,3} e^{i\pi\hat{\sigma}_n^+\hat{\sigma}_n^-} \\
&= (-1)^{\hat{\alpha}^\dagger\hat{\alpha}} \prod_{n=1,2,3} e^{i\frac{\pi}{2}(\hat{\sigma}_{z,n}-1)} \\
&= -i(-1)^{\hat{\alpha}^\dagger\hat{\alpha}} \prod_{n=1,2,3} \begin{pmatrix} i & 0 \\ 0 & -i \end{pmatrix} \\
&= -(-1)^{\hat{\alpha}^\dagger\hat{\alpha}} \prod_{n=1,2,3} \hat{\sigma}_{z,n},
\end{aligned} \tag{4.2}$$

giving the equivalent result, only comprising two more qubits. Consequently, the Hilbert space is split into two irreducible and unconnected subspaces, both infinite dimensional but with a finite number of states associated with each number of squeezed magnons. The parity symmetry imposes the constraint that all dynamics beginning in one of the bifurcated parity chains will remain within that chain.

To generate the $|\mathrm{GHZ}\rangle = \frac{1}{\sqrt{2}}(|ggg\rangle + |eee\rangle)$ state, the transition of interest is the excitation of three qubits by a single squeezed magnon mode,

$$|1, ggg\rangle \longrightarrow |0, eee\rangle. \tag{4.3}$$

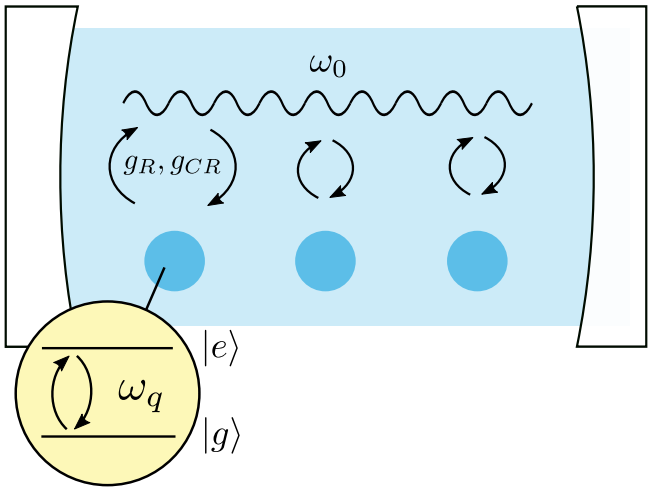

Figure 4.1: The tunable anisotropic QRM depicted in the manner of cavity quantum electrodynamics. Here, three qubits (blue dots) interact with a single magnon mode, portrayed as a standing wave. The interaction is governed by g_R and g_{CR}, the rotating and counter-rotating coupling strengths. The frequency ω_0 is the eigenfrequency of the uniform mode squeezed magnon and ω_q is the qubit frequency.

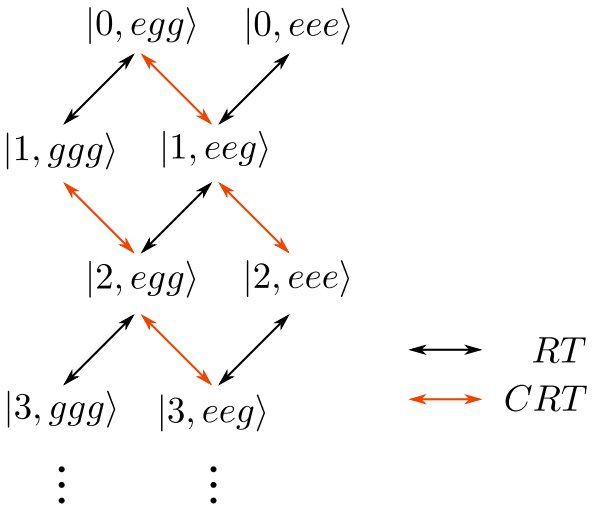

Figure 4.2: All states contained in the negative parity chain and their respective connections by rotating or counter-rotating terms. The black arrows indicate a transition by a rotating term, $\hat{a}^\dagger\hat{\sigma}^-$ or $\hat{a}\hat{\sigma}^+$, while the red arrows indicate a counter-rotating term, $\hat{a}^\dagger\hat{\sigma}^+$ or $\hat{a}\hat{\sigma}^-$. The shortest possible paths connecting $|1, ggg\rangle$ and $|0, eee\rangle$ are of third order.

There is no single step directly connecting these two states by rotating or counter-rotating terms, indicating that the initial state $|1, ggg\rangle$ can only be accomplished by going through a series of virtual intermediate states. By application of Eq. (4.2), we identify that the transition is contained within the negative parity chain and all intermediate states will also be within this chain, rendering a predictability as to which possible pathways will contribute overall and of how many steps they will consist. On the contrary, if working with only two qubits and a transition $|1, gg\rangle \rightarrow |0, ee\rangle$, parity symmetry-breaking of the atomic potentials would

be mandatory as these two states are situated in separate parity chains.

Fig. 4.2 depicts the network of states constituting the negative parity chain and how they are connected by either excitation number conserving or non-conserving transitions. It is apparent that for the transitions by a rotating term, the number of excitations is conserved, while the counter-rotating terms change the total number of excitations by two. As described previously, the composite nature of the squeezed magnon causes an intrinsic coupling enhancement by being comprised of a superposition of odd magnon number states. This in turn means that only an odd number of qubits can be excited. For instance in our case, the three qubits are coupled to the number state of three magnons in the superposition. A schematic depiction of how the squeezed magnon mode acts to excite the qubits is presented in Fig. 4.3.

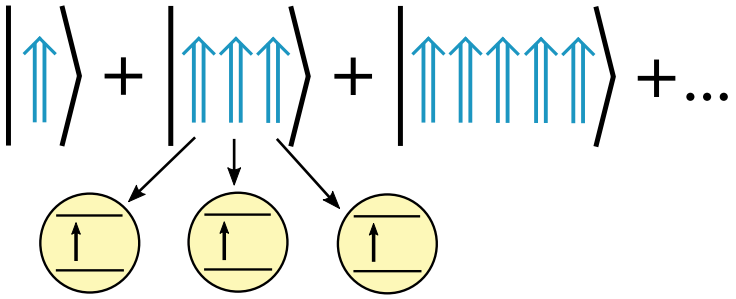

Figure 4.3: The superposition of odd magnon number states that is the squeezed magnon, enables the excitation of an odd number of qubits. Here, the excitation of three qubits (represented by yellow spheres) resulting from the state comprising three magnons, is illustrated.

4.2 Derivation of the effective Hamiltonian

Physical insights on the transition in question can be gained using the framework of perturbation theory, assuming that the interaction terms are small compared to the other terms in the Hamiltonian. The perturbation is thus

$$\hat{V} = \hat{H}_{\text{int}} = \sum_{n=1,2,3} g_{Rn}\left(\hat{\alpha}^{\dagger}\hat{\sigma}_n^{-} + \hat{\alpha}\hat{\sigma}_n^{+}\right) + g_{CRn}\left(\hat{\alpha}^{\dagger}\hat{\sigma}_n^{+} + \hat{\alpha}\hat{\sigma}_n^{-}\right), \tag{4.4}$$

for each qubit n. According to time-dependent perturbation theory, if a perturbation that is independent of time is switched on at t=0, the probability per unit time that the transition between initial state $|i\rangle$ and final state $|f\rangle$ occurs, can be determined using Fermi's golden rule,

$$W_{i\to f} = \frac{2\pi}{\hbar}\left|V_{fi}^{\text{eff}}\right|^2 \delta(E_f - E_i). \tag{4.5}$$

Here, V_{fi}^{eff} is the matrix element that defines the effective coupling, also known as the transition amplitude, of the initial and final state, $g_{\text{eff}} = -V_{fi}^{\text{eff}}$, and the δ-function ensures

energy-conservation. We note that energy conservation yields the requirement that

$$\omega_0 = \sum_i \omega_{qi}. \tag{4.6}$$

Then the bosonic mode and qubits are of similar energy, thus allowing for a resonant coupling between the states. Using first-order perturbation theory, this effective coupling corresponds to the direct transition, $V_{fi}^{\text{eff}} = \langle f|\hat{V}|i\rangle$. However, if there exists no immediate path between the two states, the transition is described by the effective Hamiltonian,

$$\hat{H}_{\text{eff}} = V_{fi}^{\text{eff}}\left(|1,ggg\rangle\langle 0,eee| + |0,eee\rangle\langle 1,ggg|\right) \tag{4.7}$$

where V_{fi}^{eff} is approximated by a series of contributions from higher-order perturbation theory. Using the standard correction to an eigenstate from time-independent perturbation theory, the effective coupling between two states $|k\rangle$ and $|n\rangle$ is approximated by the series

$$V_{nk}^{\text{eff}} = \langle k|\hat{V}|n\rangle = \langle k|\hat{V}|n^{(0)}\rangle + \lambda\langle k|\hat{V}|n^{(1)}\rangle + \lambda^2\langle k|\hat{V}|n^{(2)}\rangle + \ldots \tag{4.8}$$

where λ is the book-keeping parameter. The energy does not need to be conserved for the transitions between virtual intermediate states, only the final and initial states [42]. This is particularly relevant for the task at hand, pertaining to the fact that the transition $|1,ggg\rangle \rightarrow |0,eee\rangle$ is only possible through virtual paths that do not necessarily conserve the total excitation number, see Fig. 4.2.

4.2.1 Third-order perturbation theory

There are no direct or second-order paths that connect the states $|1,ggg\rangle$ and $|0,eee\rangle$, meaning the first contribution to V_{fi}^{eff} must be derived using third-order perturbation theory. As the transition requires an increase in the total excitation number by two, at least one of the intermediate virtual processes must be administered by a counter-rotating term. Thus, it is evident that non-zero squeezing, $r \neq 0$, is required in our system. There are only two possible routes connecting the initial and final state, as depicted in Fig. 4.4. Relating this checkerboard method of visualizing each path to Fig. 4.2, each transition can only occur between every other square, as these are the states that are within the negative parity chain. Correspondingly, only diagonal movements are allowed. Both paths involve one counter-rotating term.

The detailed expression for each diagram will be calculated using the diagrammatic approach presented by W. R. Salzman in Ref. [80]. The third-order contribution can be calculated from the second-order correction to the eigenstate of the unperturbed Hamiltonian $\hat{H}_0$,

$$|n^{(2)}\rangle = \frac{Q_n^0}{E_n^{(0)} - \hat{H}_0}\hat{V}\frac{Q_n^0}{E_n^{(0)} - \hat{H}_0}\hat{V}|n^{(0)}\rangle - \langle n^{(0)}|\hat{V}|n^{(0)}\rangle \times \left(\frac{Q_n^0}{E_n^{(0)} - \hat{H}_0}\right)^2 |n^{(0)}\rangle. \tag{4.9}$$

The complementary projection operator is $Q_n^0 = 1 - |n^{(0)}\rangle\langle n^{(0)}| = \sum_{n\neq k}|k^{(0)}\rangle\langle k^{(0)}|$. Considering the nature of $\hat{V}$, the matrix element $\langle n^{(0)}|\hat{V}|n^{(0)}\rangle$ is zero regardless of the state of $|n^{(0)}\rangle$. By setting $|n^{(0)}\rangle = |1,ggg\rangle$, applying $\langle 0,eee|\hat{V}$ from the left side of Eq. (4.9) and

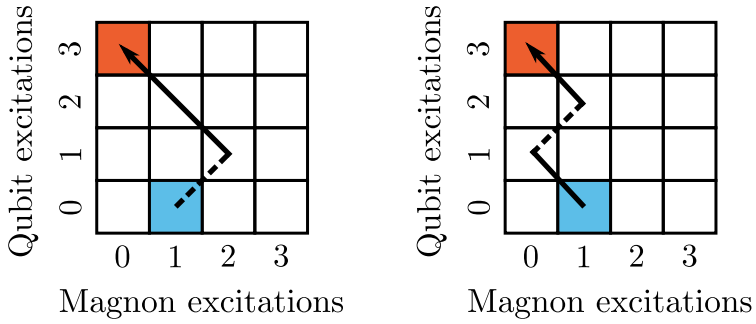

Figure 4.4: Diagrams of the third-order paths connecting the initial state $|1,ggg\rangle$, represented by a blue square, to the final state $|0,eee\rangle$, represented by a red square. A counter-rotating process and rotating process is pictured by a dashed line and solid line, respectively. The magnon excitations in question are the number of squeezed magnons, as represented by the $\hat{\alpha}$-basis.

inserting the identity operator between all operator products, the contribution from the first path of Fig. 4.4 to the third-order effective coupling can be calculated,

$$\begin{aligned} g_{\text{eff}}^{(3a)} &= -\langle 0,eee|\hat{V}|1,ggg^{(2)}\rangle \\ &= -\sum_{\substack{i,j,k \\ i\neq j\neq k}} \frac{\langle 0,eee|\hat{V}|1,eeg\rangle}{(-\omega_{qi}-\omega_{qj})} \frac{\langle 1,eeg|\hat{V}|2,egg\rangle}{(-\omega_0-\omega_{qi})} \times \langle 2,egg|\hat{V}|1,ggg\rangle \\ &= -\sum_{\substack{i,j,k \\ i\neq j\neq k}} \frac{2g_{CRi}g_{Rj}g_{Rk}}{(-\omega_{qi}-\omega_{qj})(-\omega_0-\omega_{qi})} \end{aligned}, \tag{4.10}$$

where i,j,k label the order of excited qubits, counting all possible qubit permutations. Using the same procedure and carrying out the calculation for $g_{\text{eff}}^{(3b)}$, the total third-order contribution becomes

$$g_{\text{eff}}^{(3)} = g_{\text{eff}}^{(3a)} + g_{\text{eff}}^{(3b)} = \sum_{\substack{i,j,k \\ i\neq j\neq k}} \left[-\frac{2g_{CRi}g_{Rj}g_{Rk}}{(\omega_{qi}+\omega_{qj})(\omega_0+\omega_{qi})} + \frac{g_{Ri}g_{CRj}g_{Rk}}{(\omega_{qi}+\omega_{qj})(\omega_0-\omega_{qi})} \right] \tag{4.11}$$

By the restriction of energy-conservation between the initial and final state, the squeezed magnon mode frequency must be $\omega_0 = \sum_i \omega_{qi}$. Inserting this into Eq. (4.11) and accounting for all possible permutations, it can be shown that all contributions cancel each other out and the effective coupling $g_{\text{eff}}^{(3)} = 0$. Therefore, the third-order contribution to g_{eff} is zero and higher-order corrections must be considered.

Assuming symmetric qubits, such that $\omega_{qi} = \omega_q$, $g_{Ri} = g_R$ and $g_{CRi} = g_{CR}$, a simplified expression for $g_{\text{eff}}^{(3)}$ can be achieved. Counting all possible qubit permutations, our expression for $g_{\text{eff}}^{(3)}$ reads

$$g_{\text{eff}}^{(3)} = 6 \times \left(\frac{g_{CR}g_R^2}{2\omega_q(\omega_0-\omega_q)} - \frac{2g_{CR}g_R^2}{2\omega_q(\omega_0+\omega_q)} \right) = 3g_{CR}g_R^2 \frac{3\omega_q-\omega_0}{\omega_q(\omega_0^2-\omega_q^2)}, \tag{4.12}$$

from which we can clearly see how the third-order contribution cancels under the resonance condition $\omega_0 = 3\omega_q$.

4.2.2 Fifth-order perturbation theory

Since the third-order contribution cancels out and there exist no possible fourth-order paths connecting $|1,ggg\rangle$ and $|0,eee\rangle$, the lowest order contribution will be fifth-order. In contrast to the relatively straightforward expression of $|n^{(2)}\rangle$, $|n^{(4)}\rangle$ contains 13 different terms. However, the matrix element $\langle n^{(0)}|\hat{V}|n^{(0)}\rangle$ occurs in the coefficients of nine of these terms, effectively leaving us with only four terms that need to be considered. The fourth-order correction to the eigenstate with only the remaining terms is

$$\begin{aligned}
|n^{(4)}\rangle = &- \langle n^{(0)}|\hat{V}\frac{Q_n^0}{E_n^{(0)}-\hat{H}_0}\hat{V}|n^{(0)}\rangle \times \Big(\frac{Q_n^0}{E_n^{(0)}-\hat{H}_0}\Big)^2\hat{V}\frac{Q_n^0}{E_n^{(0)}-\hat{H}_0}\hat{V}|n^{(0)}\rangle ... \\
&- \langle n^{(0)}|\hat{V}\frac{Q_n^0}{E_n^{(0)}-\hat{H}_0}\hat{V}|n^{(0)}\rangle \times \frac{Q_n^0}{E_n^{(0)}-\hat{H}_0}\hat{V}\Big(\frac{Q_n^0}{E_n^{(0)}-\hat{H}_0}\Big)^2\hat{V}|n^{(0)}\rangle ... \\
&- \langle n^{(0)}|\hat{V}\Big(\frac{Q_n^0}{E_n^{(0)}-\hat{H}_0}\hat{V}\Big)^2|n^{(0)}\rangle \times \Big(\frac{Q_n^0}{E_n^{(0)}-\hat{H}_0}\Big)^2\hat{V}|n^{(0)}\rangle ... \\
&+ \Big(\frac{Q_n^0}{E_n^{(0)}-\hat{H}_0}\hat{V}\Big)^4|n^{(0)}\rangle
\end{aligned} \tag{4.13}$$

By the same procedure as used for third-order, the matrix element $\langle 0,eee|\hat{V}|1,ggg^{(4)}\rangle$ can be calculated. Insertion of the complementary projection operator leads to contributions corresponding to 15 unique paths, where there is one "pure" fifth-order path and the rest are third-order paths with one additional loop. There are no second-order paths connecting the final and initials state, such that the third term of Eq. (4.13) lead to no contributions. Setting $|1,ggg\rangle = |i\rangle$ and $|0,eee\rangle = |f\rangle$ for simple notation, the fifth-order correction to the coupling strength with only non-vanishing contributions is

$$\begin{aligned}
\langle f|\hat{V}|i^{(4)}\rangle = &- \langle i^{(0)}|\hat{V}\frac{Q_i^0}{E_i^{(0)}-\hat{H}_0}\hat{V}|i^{(0)}\rangle \times \langle f|\hat{V}\Big(\frac{Q_i^0}{E_i^{(0)}-\hat{H}_0}\Big)^2\hat{V}\frac{Q_i^0}{E_i^{(0)}-\hat{H}_0}\hat{V}|i^{(0)}\rangle ... \\
&- \langle i^{(0)}|\hat{V}\frac{Q_i^0}{E_i^{(0)}-\hat{H}_0}\hat{V}|i^{(0)}\rangle \times \langle f|\hat{V}\frac{Q_i^0}{E_i^{(0)}-\hat{H}_0}\hat{V}\Big(\frac{Q_i^0}{E_i^{(0)}-\hat{H}_0}\Big)^2\hat{V}|i^{(0)}\rangle ... \\
&+ \langle f|\hat{V}\Big(\frac{Q_i^0}{E_i^{(0)}-\hat{H}_0}\hat{V}\Big)^4|i^{(0)}\rangle
\end{aligned} \tag{4.14}$$

As seen in the previous section, the two third-order contributions to the effective coupling cancel under the resonance condition $\omega_0 = \sum_i \omega_{qi}$, accounting for all possible qubit permutations. Therefore, all pairs of third-order diagrams with a loop on a shared vertex will also fully cancel at resonance, such as the pair depicted in Fig. 4.5. This is with the exception of the paths that have a shared loop on the initial vertices, as these have remaining contributions supplied by the terms with coefficients $\langle i^{(0)}|\hat{V}Q_i^0/(E_i^{(0)}-\hat{H}_0)\hat{V}|i^{(0)}\rangle$ of Eq. (4.14). Additionally we note that the single pair of diagrams which have a shared loop through the final state $|0,eee\rangle$, are divided by a zero energy difference due to energy-conservation, but cancel faster than they diverge regardless.

The seven remaining diagrams with non-vanishing contributions are depicted in Figs. 4.6, 4.7 and 4.8. Beginning with the diagrams that have a loop on the initial vertices,

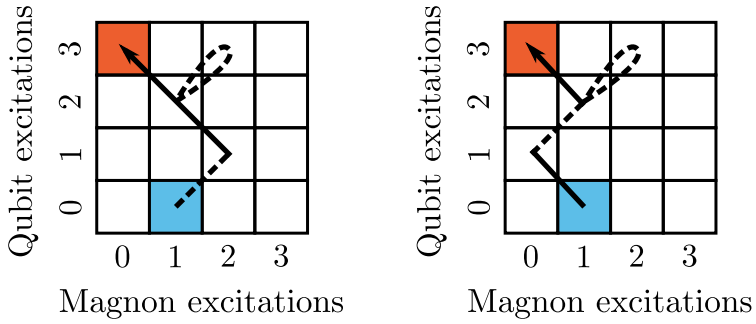

Figure 4.5: Example of the fifth-order diagrams which comprise a third-order path and a loop on a shared vertex. Consistently with the result from third-order perturbation theory, these diagrams cancel at resonance. The initial state is represented by a blue square and the final state by a red square. Dashed lines illustrate counter-rotating processes.

these only cancel partially. The pair of diagram (a) and (b) depicted in Fig. 4.6 give the contributions:

$$g_{\text{eff}}^{(5a)} = -\sum_{\substack{i,j,k,l \\ j\neq k\neq l}} \left(\frac{2g_{CRi}^2}{-\omega_0-\omega_{qi}}\right)\left(\frac{2g_{CRj}g_{Rk}g_{Rl}}{(-\omega_0-\omega_{qj})^2(-\omega_{qj}-\omega_{qk})}\right) \tag{4.15}$$

$$g_{\text{eff}}^{(5b)} = -\sum_{\substack{i,j,k,l \\ j\neq k\neq l}} \left(\frac{2g_{CRi}^2}{-\omega_0-\omega_{qi}}\right)\left(\frac{g_{Rj}g_{CRk}g_{Rl}}{(\omega_0-\omega_{qj})^2(-\omega_{qj}-\omega_{qk})}\right) \tag{4.16}$$

Similarly, the diagram (c) and (d) depicted in Fig. 4.7 give the contributions:

$$g_{\text{eff}}^{(5c)} = -\sum_{\substack{i,j,k,l \\ j\neq k\neq l}} \left(\frac{g_{Ri}^2}{\omega_0-\omega_{qi}}\right)\left(\frac{2g_{CRj}g_{Rk}g_{Rl}}{(-\omega_0-\omega_{qj})^2(-\omega_{qj}-\omega_{qk})}\right) \tag{4.17}$$

$$g_{\text{eff}}^{(5d)} = -\sum_{\substack{i,j,k,l \\ j\neq k\neq l}} \left(\frac{g_{Ri}^2}{\omega_0-\omega_{qi}}\right)\left(\frac{g_{Rj}g_{CRk}g_{Rl}}{(\omega_0-\omega_{qj})^2(-\omega_{qj}-\omega_{qk})}\right) \tag{4.18}$$

The remaining diagrams originate from the third term of Eq. (4.14), depicted in Fig. 4.8. The diagram (e) represents the single "pure" fifth-order path, while (f) and (g) contribute as these have no corresponding third-order pair with a shared loop. The contribution from diagrams (e), (f) and (g) are:

$$g_{\text{eff}}^{(5e)} = \sum_{\substack{i,j,k,l \\ i\neq j\neq k}} \frac{6g_{CRi}g_{CRj}g_{Rk}g_{CRl}g_{Rl}}{(-\omega_0-\omega_{qi})(-2\omega_0-\omega_{qi}-\omega_{qj})(-\omega_0-\sum_n\omega_{qn})(\omega_{ql}-\sum_n\omega_{qn})} \tag{4.19}$$

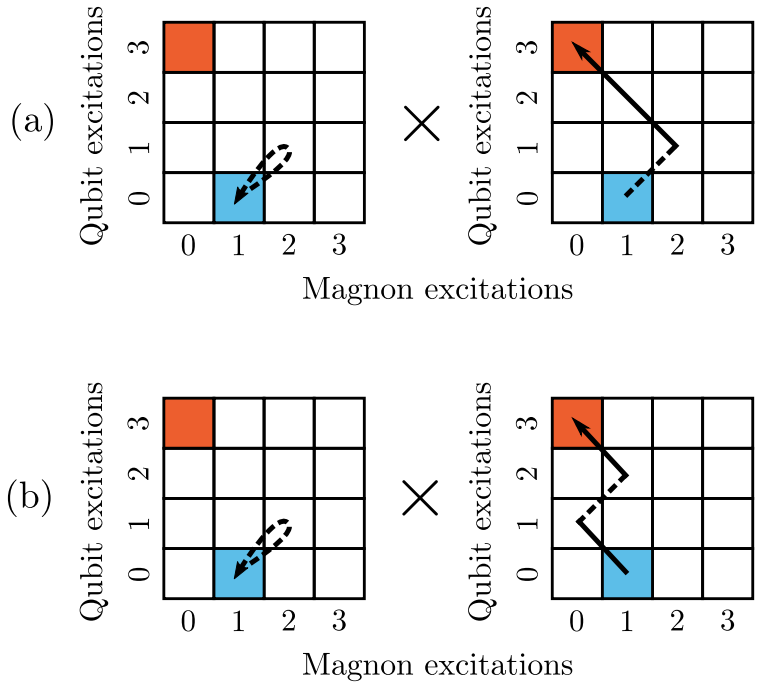

Figure 4.6: Pairs of fifth-order paths connecting the states $|1,ggg\rangle$ and $|0,eee\rangle$ by virtual transitions, comprising a third-order path and a counter-rotating loop on a shared vertex. As a result of the loop being on an initial vertex, these diagrams do not cancel fully at resonance such as the example diagrams in Fig. 4.5.

$$g_{\text{eff}}^{(5f)} = \sum_{\substack{i,j,k,l,m,n \\ i\neq j\neq k \\ l=i,j \;\; m=l,k \\ m\neq n \;\; n=l,k}} \frac{6 g_{CRi} g_{CRj} g_{CRl} g_{Rm} g_{Rn}}{(-\omega_0-\omega_{qi})(-2\omega_0-\omega_{qi}-\omega_{qj})(-\omega_0+\omega_{ql}+\omega_{qk}-\sum_p \omega_{qp})(\omega_{qn}-\sum_p \omega_{qp})} \tag{4.20}$$

$$g_{\text{eff}}^{(5g)} = \sum_{\substack{i,j,k,l \\ i\neq j\neq k}} \frac{6 g_{CRi} g_{Ri} g_{Rj} g_{Rk} g_{Rl}}{(-\omega_0-\omega_{qi})(-2\omega_0)(-\omega_0-\omega_{ql})(-\omega_{qj}-\omega_{qk})} \tag{4.21}$$

The next lowest-order contribution to the effective coupling can be found by seventh-order perturbation theory, where several of the possible contributions will be third-order paths with multiple additional loops. Assuming that the coupling strengths are small enough that the seventh-order contributions will be much smaller than fifth-order, we approximate our fifth-order result as the lowest-order contribution to the effective coupling strength. Assuming symmetric qubits, setting $\omega_{qi} = \omega_q$, $g_{Ri} = g_R$, $g_{CRi} = g_{CR}$ and $\omega_0 = 3\omega_q$ and accounting for all possible qubit permutations, the total effective coupling to fifth-order is,

$$g_{\text{eff}}^{(5)} = -\frac{27 g_{CR}^3 g_R^2}{32\omega_q^4} + \frac{9 g_{CR} g_R^4}{4\omega_q^4}. \tag{4.22}$$

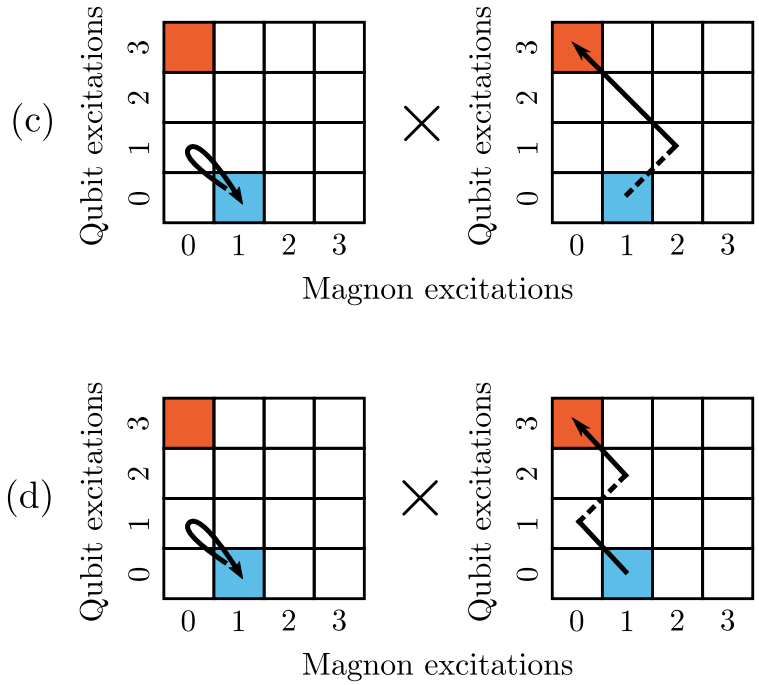

Figure 4.7: Pairs of fifth-order paths connecting the states $|1,ggg\rangle$ and $|0,eee\rangle$ by virtual transitions, comprising a third-order path and a rotating loop on a shared vertex. As a result of the loop being on an initial vertex, these diagrams cancel only partially at resonance.

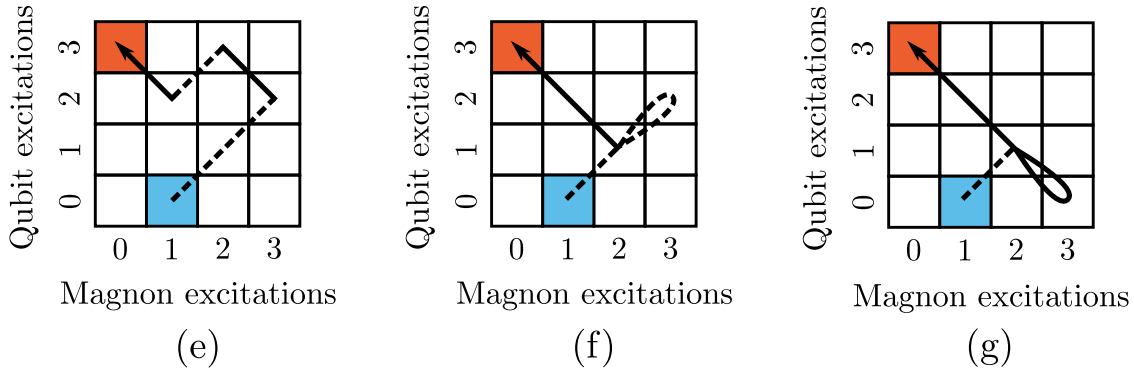

Figure 4.8: Fifth-order diagrams connecting the states $|1,ggg\rangle$ and $|0,eee\rangle$ by virtual transitions, with non-vanishing contributions. (a) is the single pure fifth-order path with no loops, while (f) and (g) do not cancel as they have no corresponding third-order path with a loop on shared vertex.

The effective coupling strength can therefore be tuned to zero at the specific instance $g_{CR} = \pm\sqrt{\frac{8}{3}}g_R$, as well as when either of g_{CR} or g_R themselves are zero. With this expression we finally obtain the effective Hamiltonian,

$$\hat{H}_{\text{eff}} = \left(\frac{27g_{CR}^3 g_R^2}{32\omega_q^4} - \frac{9g_{CR}g_R^4}{4\omega_q^4}\right) \times \left(|1,ggg\rangle\langle 0,eee| + |0,eee\rangle\langle 1,ggg|\right). \tag{4.23}$$

We have thus achieved an analytical expression for the effective coupling in the truncated Hilbert space consisting of $|1, ggg\rangle$ and $|0, eee\rangle$. In the preceding numerical analysis of the tunable anisotropic QRM that describes our system, this result will not only be central in describing the static properties of our system but also the dynamical properties.

5 Numerical investigation of system eigenenergies and dynamics

As made evident from the analysis of the previous chapters, the existence of squeezing in our system enables higher-order transitions that do not conserve the total number of excitations. Guided by this intuition, this chapter will present a numerical investigation of the system eigenenergies and dynamics for the three-qubit $|1, ggg\rangle \rightarrow |0, eee\rangle$ transition. The calculations involve a numerical diagonalization of the tunable anisotropic QRM Hamiltonian, proceeded by a corresponding discussion on the energy spectrum and resonant couplings between the eigenstates. Furthermore, an analysis of the system dynamics investigating the existence of coherent oscillations of energy between the initial and final states is made, quantifying the behavior in terms of the parameters governing the time-evolution of the system. The nature of the transition will also be probed by evaluating the coherence rate of the excitations using a three-qubit correlation function.

All numerical calculations in this thesis were performed in Python with the use of the QuTiP - Quantum Toolbox in Python - library, which is a framework created for simulating dynamics of open quantum systems [81, 82]. The dynamics of the magnon|spin-qubit system were solved using a master equation evolution of the anisotropic Rabi Hamiltonian of Eq. (4.1), without introducing any dissipation. In all cases, the system has been time-evolved from the initial state $|1, ggg\rangle$ and the transition is thus mandated by the paths outlined in chapter 4. For all calculations the qubits and couplings are assumed to be symmetric, as this does not affect the physical picture significantly. The coupling strengths are $g_R = g_{CR} = 0.1\omega_q$ unless otherwise stated, just on the border between the SC and USC regimes to ensure that our results are compatible with the perturbative analysis. Consistent with the rest of the thesis, $\hbar$ is set to 1. Additionally, all frequencies are determined relatively to the qubit frequency $\omega_q = 2\pi$.

5.1 System eigenenergies

To explore the coupling between states under various resonance conditions we numerically diagonalize the Hamiltonian of Eq. (4.1), coupling one squeezed magnon mode to three qubits, in a range of values of the squeezed magnon mode frequency ω_0. This yields the spectrum depicted in Fig. 5.1. Labelling the resulting eigenstates and eigenvalues as $|i\rangle$ and ω_i, where $\omega_k > \omega_j$ for $k > j$, the eigenfrequency of the state $|i\rangle$ is plotted as the energy difference $\omega_i - \omega_0$, where ω_0 for the moment labels the eigenfrequency of the ground state. Employing the small but finite symmetric coupling strengths $g_R = g_{CR} = 0.1\omega_q$, the system is on the immediate boundary between the SC and USC regimes, such that it can be closely described by the Jaynes-Cummings model. Consequently, there are no major perceptible

differences between this spectrum and an equivalent spectrum where the counter-rotating terms have been neglected, at this scale.

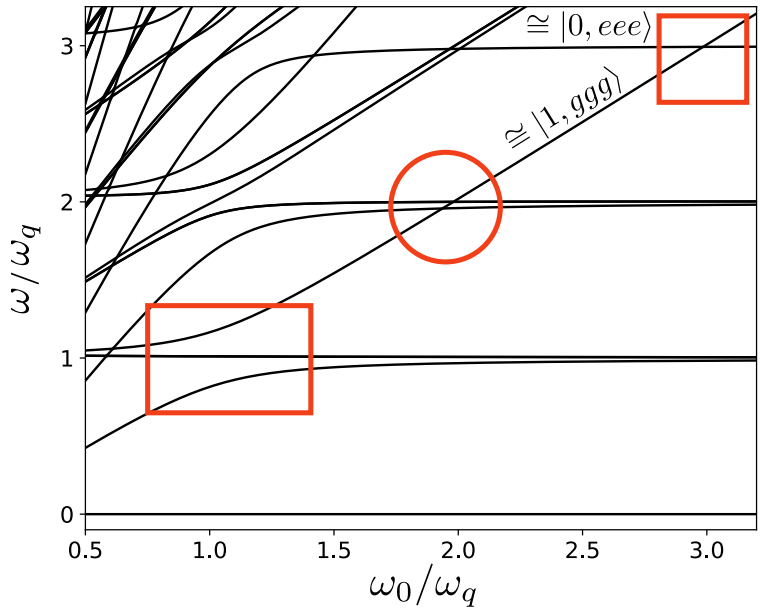

Figure 5.1: The energy spectrum resulting from the numerical diagonalization of Eq. (4.1), describing a system of one squeezed magnon mode coupled to three qubits. All qubit frequencies and coupling strengths are symmetric, with $g_R = g_{CR} = 0.1\omega_q$. The red rectangle in the lower left corner highlights the large one-excitation anti-crossing at $\omega_0 \approx \omega_q$, present in both the Jaynes-Cummings model and QRM as the total number of excitations is conserved. The red circle emphasizes the double crossing at $\omega_0 \approx 2\omega_q$, resulting from the forbidden interaction between one squeezed magnon and an even number of qubits. The red square features a small anti-crossing at $\omega_0 \approx 3\omega_q$, from the resonant coupling between one squeezed magnon and three qubits, present due to finite squeezing enabling counter-rotating processes in our system. Far from the anti-crossing, the energy-levels can be approximated by the states $|0, eee\rangle$ and $|1, ggg\rangle$, as indicated.

The main features of the energy spectrum are those of the individual subsystem with zero qubit-magnon coupling, only with energy-splittings bestowed by the coupling between states, introduced by the rotating and counter-rotating terms. Pure qubit states have a flat energy-level irrespective of the value of ω_0 where the degeneracy is dependent on the number of possible qubit permutations. For instance, the states $|0, eeg\rangle$ and $|0, egg\rangle$ give rise to two degenerate triplets, overall giving four visually distinct flat curves from the various qubit states with zero squeezed magnons. States with n squeezed magnons will exhibit a linear dependence of $n\omega_0$. Beginning with the lowest energy levels, the first major anti-crossing in Fig. 5.1, highlighted by a rectangle, is around $\omega_0 \approx \omega_q$. This anti-crossing corresponds to the first rung of the Jaynes-Cummings ladder, with the states $|1, ggg\rangle$ and $|0, egg\rangle$ coupled by a rotating process. Thus, with no change in the total number of excitations, this large anti-crossing is both present with and without the rotating wave-approximation. When the energy-splitting is at its minimum, the resulting eigenstates are the dressed states

$$\frac{1}{\sqrt{2}}(|0, egg\rangle \pm |1, ggg\rangle). \tag{5.1}$$

The next distinct crossing, highlighted by the red circle in Fig. 5.1, is the double crossing of the states $|1,ggg\rangle$ and $|0,eeg\rangle$ at around $\omega_0 \approx 2\omega_q$. A coupling between these states is forbidden as only an odd number of qubits can be excited by one squeezed magnon, as depicted in Fig. 3.3, further elucidated by the fact that these two states are confined in separate parity chains. This result was also verified by checking that the levels still cross at a magnitude much smaller than a plausible splitting value. An enlarged view of each crossing can be found in Fig. 5.2.

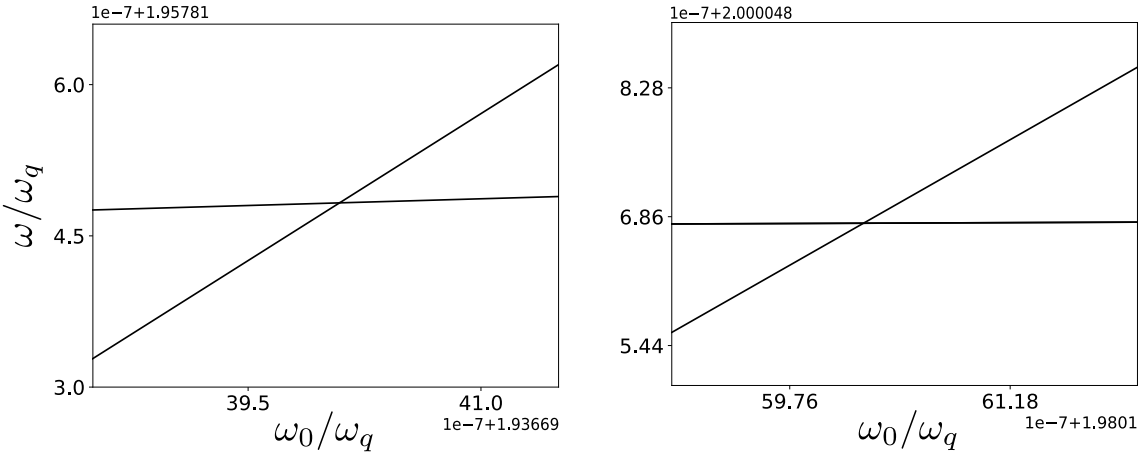

(a) **(b)**

Figure 5.2: Enlarged view of the double crossings emphasized by the red circle in Fig. 5.1. (a) corresponds to the left-most and (b) to the right-most crossing. The crossing levels approximately correspond to the states $|1,ggg\rangle$ and $|0,eeg\rangle$ and are present in both the Jaynes-Cummings and QRM, as the total excitation number is not conserved and the excitation of an even number of qubits by a squeezed magnon is forbidden. The crossings were inspected at a scale smaller than a possible splitting value, to verify that they are not avoided crossings.

The crossing around $\omega_0 \approx 3\omega_q$ emphasized by the red square in Fig. 5.1 is in fact an anti-crossing manifesting a small splitting, a signature for resonant coupling. In accordance with the effective Hamiltonian, Eq. (4.23), this energy splitting is given by

$$\Delta\omega = 2g_{\text{eff}}^{(5)}. \tag{5.2}$$

The flat energy level corresponds to the state $|0,eee\rangle$, while the diagonal line corresponds to $|1,ggg\rangle$. This splitting is a result of the resonant coupling between these states and at its minimum, the resulting system is in the hybridized states

$$\frac{1}{\sqrt{2}}(|0,eee\rangle \pm |1,ggg\rangle). \tag{5.3}$$

This anti-crossing is not present in the Jaynes-Cummings model as the total number of excitations is not conserved and forbidden through solely rotating transitions, but is present in our system due to non-zero squeezing. The presence of squeezing enables the counter-rotating terms to allow virtual non-conserving transitions, coupling the states in our transition of interest. Hence, the presence of an avoided crossing close to the resonance condition $\omega_0 \approx 3\omega_q$ provides the evidence that one squeezed magnon is able to

resonantly excite three qubits. An enlarged view of the anti-crossing along with the same system evaluated with an absence of counter-rotating terms, is depicted in Fig. 5.3. By virtue of the perturbation, a shift in the energy-levels is introduced, which depends on the individual values of g_R and g_{CR}. As a result, the crossings in the presence and absence of counter-rotating terms occur for different values of the squeezed magnon frequency. In Fig. 5.3 the crossing and anti-crossing are depicted as overlapping for the sake of an intuitive physical picture.

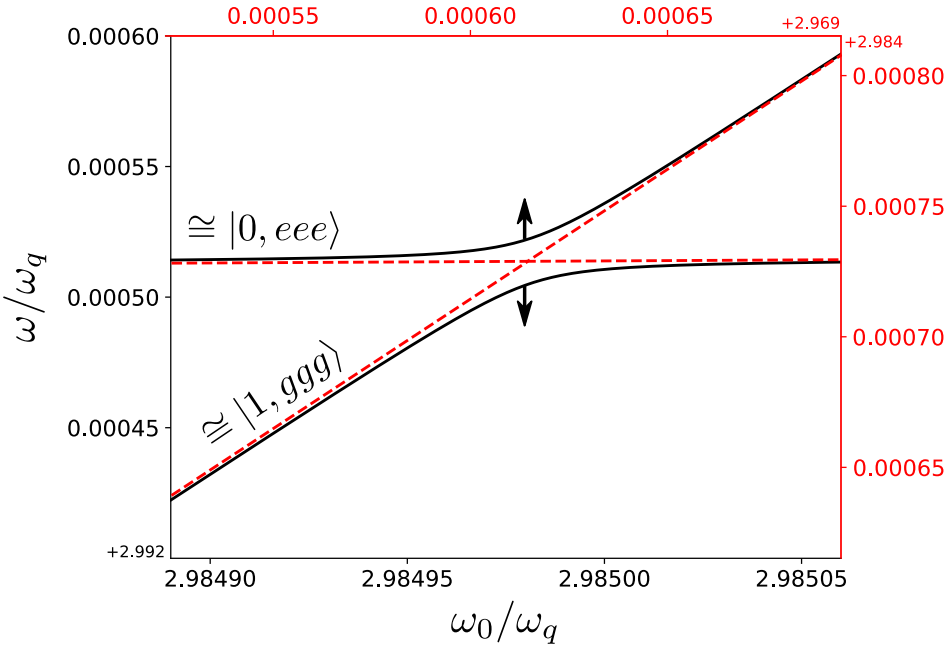

Figure 5.3: Enlarged view of the anti-crossing highlighted by a square in Fig. 5.1. The arrows highlight the smallest splitting, $\Delta\omega \approx 2g_{\text{eff}}$, where the system is in the eigenstates $(1/\sqrt{2})(|0, eee\rangle \pm |1, ggg\rangle)$. The red dashed lines depict the spectrum evaluated with the rotating wave approximation applied, i.e. $g_{CR} = 0$, which has a small shift relative to the anti-crossing.

The g_R and g_{CR} dependence of the effective coupling responsible for the $|1, ggg\rangle \rightarrow |0, eee\rangle$ transition, Eq. (4.22), was found through a perturbative treatment to fifth order. However, an exact expression for g_{eff} can also be obtained through a fitting procedure of $\Delta\omega$, since the effective coupling is related to the splitting value through the expression in Eq. (5.2). We expect the following relation for the splitting,

$$\frac{\Delta\omega}{g_{CR}} = Ag_R^4 + Bg_R^2 g_{CR}^2, \tag{5.4}$$

due to there only existing fifth-order paths with either four rotating transitions and one counter-rotating transition, or two of the former and three of the latter. By setting $g_R = 0.1\omega_q$, we achieve a parabolic relationship between $\Delta\omega/g_{CR}$ and g_{CR} where the values of the constants A and B can be determined by a series measurement of the splitting value $\Delta\omega$ for different values of $0 < g_{CR} < 0.1\omega_q$. This will be more accurate than the result obtained using perturbation theory, since by using the smallest splitting it is implicit that the effective coupling strength is evaluated at the exact resonance frequency. Plotting the obtained data

set, the fitting shows a perfect parabolic dependence as demonstrated in Fig. 5.4, and is thus in agreement with the terms in g_{eff} achieved with perturbation theory. The calculated final relation for g_{eff} is,

$$\frac{g_{\text{eff}}}{\omega_q} = 1.2\left(\frac{g_R}{\omega_q}\right)^4\left(\frac{g_{CR}}{\omega_q}\right) - 0.3\left(\frac{g_R}{\omega_q}\right)^2\left(\frac{g_{CR}}{\omega_q}\right)^3. \tag{5.5}$$

We remark that this expression for the splitting value is not only dependent on g_R and g_{CR}, but also on the value of ω_q. Additionally, albeit this result is consistent with the perturbation analysis, the fitting procedure was done for $g_R = 0.1\omega_q$ which renders our perturbation theory always correct because g_R is consistently small. The determined values of A and B therefore only apply for values of g_R and g_{CR} where the seventh-order correction can be neglected.

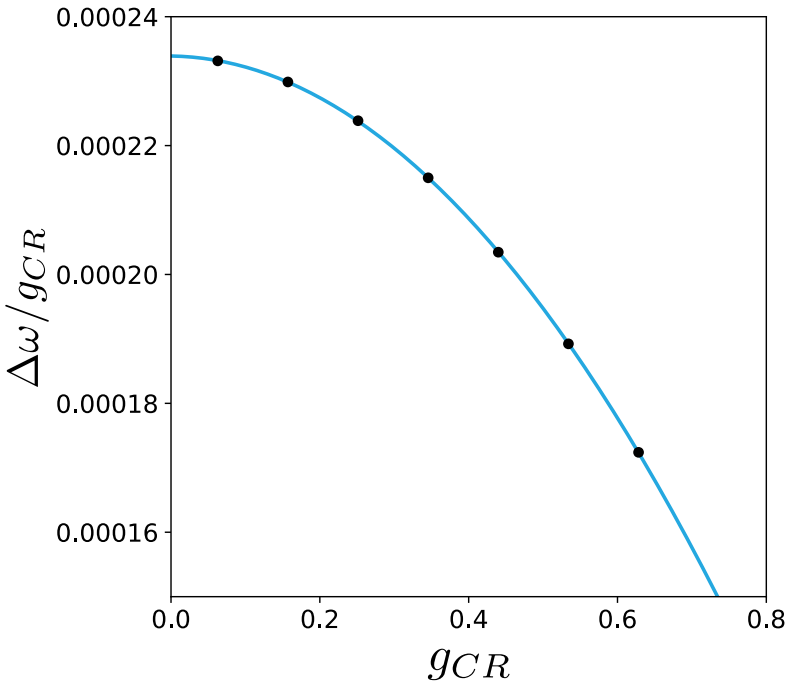

Figure 5.4: Parabolic fitting (blue solid line) of the obtained splitting values $\Delta\omega$, evaluated for seven values of $0 < g_{CR} < 0.1\omega_q$ (black points). The perfect fit ensures that the fifth-order perturbation theory provides a good approximation to the effective coupling strength for our choice of parameters.

5.1.1 Correction to the resonance frequency

As mentioned previously, the perturbation introduces a slight shift in the energy-levels such that the location of the crossing depends on the value of g_{CR} and g_R. Consequently, the smallest splitting does not occur exactly at $\omega_0 = \sum_i \omega_{qi}$ and the $|1,ggg\rangle \rightarrow |0,eee\rangle$ transition is resonant for a slightly smaller value of ω_0, where we assume in keeping with the previous perturbation analysis that the qubits are not symmetric. This value can be approximated theoretically by second-order perturbation for the two relevant states. Beginning with $|1,ggg\rangle$, there are two possible intermediate states contributing to the

second-order correction, $|0,egg\rangle$ and $|1,egg\rangle$. With the correction defined through the relation $E_n^{(2)} = \sum_k |\langle n|V|k\rangle|^2/(E_n - E_k)$, we obtain

$$E_{|1,ggg\rangle} = \omega_0 + \sum_i \frac{g_{Ri}^2}{2\omega_{qi}} - \frac{g_{CRi}^2}{2\omega_{qi}}. \tag{5.6}$$

For the state $|0,eee\rangle$ there are only one possible intermediate state, $|2,eeg\rangle$, giving the correction

$$E_{|0,eee\rangle} = \sum_i \omega_{qi} - \frac{g_{Ri}^2}{2\omega_{qi}}. \tag{5.7}$$

The position of the largest splitting in terms of ω_0, can then be found by equating these relations, the same position as where the energy of the separate states would cross, giving the following expression for the correction to the resonance frequency

$$\omega_0 = \sum_i \omega_{qi} - \frac{g_{Ri}^2}{\omega_{qi}} + \frac{g_{CRi}^2}{2\omega_{qi}}, \tag{5.8}$$

which for symmetric qubits is

$$\omega_0 = 3\omega_q - 3\frac{g_R^2}{\omega_q} + 3\frac{g_{CR}^2}{2\omega_q}. \tag{5.9}$$

We observe that the correction increases quadratically for increasing g_{CR} and decreases with g_R^2. Comparing this result to the numerical determination of the resonance frequency, $\omega_0 \approx 2.98498\omega_q$, we have at $g_R = g_{CR} = 0.1\omega_q$, a percentage deviation of less than 0.0006%. This percentage difference increases the larger the coupling strengths get, and is most accurate for both coupling strengths at $g < 0.1\omega_q$.

This also introduces a correction to the third-order result for the effective coupling strength $g_{\text{eff}}^{(3)}$, Eq. (4.12), as the resonance frequency no longer is $\omega_0 = 3\omega_q$. Inserting Eq. (5.9) into the expression for $g_{\text{eff}}^{(3)}$ and omitting terms over fifth order in $g_{CR,R}$ leaves us with

$$g_{\text{eff}}^{(3)\prime} = \frac{9\left(g_{CR}^3 g_R^2 - 2g_{CR}g_R^4\right)}{16\omega_q^4}, \tag{5.10}$$

where the prime now indicates that this is the third-order result evaluated specifically at the avoided crossing. This result can be individually tuned to zero at $g_{CR} = \pm\sqrt{2}g_R$. By similarly evaluating $g_{\text{eff}}^{(5)}$ at the anti-crossing and neglecting terms above fifth order in g_R and g_{CR}, the fifth-order result will remain unchanged and the correction at the anti-crossing provides no significant contribution here. The total effective coupling strength, evaluated using perturbation theory becomes

$$g_{\text{eff}}' = g_{\text{eff}}^{(3)\prime} + g_{\text{eff}}^{(5)} = \frac{-9\left(g_{CR}^3 g_R^2 - 4g_{CR}g_R^4\right)}{32\omega_q^4}, \tag{5.11}$$

which can be tuned to zero at $g_{CR} = \pm 2g_R$. Thus, evaluating the effective coupling at the anti-crossing instead of at $\omega_0 = 3\omega_q$, adds a small correction from the non-zero third-order result. This result is more consistent with the expression for g_{eff} achieved from the numerical fitting procedure.

5.2 System dynamics and three-qubit correlation

So far, a numerical investigation of the system has been conducted, revealing a coherent coupling between the states of interest at a resonance frequency determined by the minimum splitting $\Delta\omega$ in the spectrum. However, to probe this resonant coupling further, we need a quantitative analysis of the system dynamics through the evaluation of average squeezed magnon and qubit occupation numbers. as well as qubit correlation functions. A central objective here is to establish the nature of the transition between the states, in the sense of whether or not there is a joint and synchronous excitation of qubits and a reversible transfer of energy between the bosonic mode and the qubits.

The time evolution of the initial state $|1,ggg\rangle$ is calculated numerically using a master equation evolution available in the QuTiP library, of the Hamiltonian in Eq. (4.1). Analytically, the time evolution is defined through the standard relation,

$$|\psi(t)\rangle = e^{-i\hat{H}t}|\psi(0)\rangle. \tag{5.12}$$

In lieu of having to manage large numbers computationally, all variables in the Hamiltonian such as $g_{R,CR}$ and ω_0, are normalized in terms of the qubit frequency ω_q. The time evolution then reads,

$$|\psi(t')\rangle = e^{-i\frac{\hat{H}}{\omega_q}\omega_q t}|\psi(0)\rangle = e^{-i\hat{H}'t'}|\psi(0)\rangle, \tag{5.13}$$

with the Hamiltonian and time parameter redefined as

$$\hat{H}' = \frac{\hat{H}}{\omega_q} \quad \text{and} \quad t' = \omega_q t. \tag{5.14}$$

We therefore note that the temporal evolution of $|\psi(t)\rangle$ is evaluated over the time period t'.

An important distinction in the USC regime from the SC regime, is that the virtual excitations arising from the counter-rotating terms do not generate physically observable particles that can be detected in experiment. As a result, special consideration need to be taken to not acquire unphysical emission and absorption statistics. As originally outlined in R. J. Glauber's formulation of photodetection, employing the terminology of cavity quantum electrodynamics, an accurate depiction of the field statistics is captured by expressing the cavity electric-field operator $\hat{X} = \hat{a} + \hat{a}^\dagger$ in the dressed basis. The result is the decomposed positive- and negative frequency operators,

$$\hat{X}^+ = \sum_{j,k>j} X_{jk}|j\rangle\langle k|, \quad \hat{X}^- = (\hat{X}^+)^\dagger \tag{5.15}$$

where $X_{jk} \equiv \langle j|(\hat{a} + \hat{a}^\dagger)|k\rangle$ [83, 84]. Using these operators, one obtains that $\hat{X}^+|0\rangle = 0$ in the USC regime as opposed to $\hat{a}|0\rangle \neq 0$ as given in Eq. (2.64). Hence, only observable photons are accounted for. Likewise, the qubit positive- and negative frequency operators reads

$$\hat{C}^+ = \sum_{j,k>j} C_{jk}|j\rangle\langle k|, \quad \hat{C}^- = (\hat{C}^+)^\dagger \tag{5.16}$$

where $C_{jk} \equiv \langle j|(\hat{\sigma}^- + \hat{\sigma}^+)|k\rangle$ [16, 18]. As follows, in the USC regime the photon and qubit emission rates are proportional to the photon and qubit mean excitation numbers, $\langle \hat{X}^-\hat{X}^+\rangle$ and $\langle \hat{C}^-\hat{C}^+\rangle$, respectively.

This framework for photodetection does not directly translate to our magnon|spin-qubit ensemble, as $\hat{X}$ does not correspond to an electric field and $\hat{\alpha}$ does not inherit all the same properties as the annihilation and creation operators of a photon bosonic mode. However, the positive and negative frequency operators for the cavity field operators can be defined in terms of our squeezed magnon mode, without loosing any essential physics. Additionally, as we are working in the immediate boundary between the SC and USC regime, our system is well approximated by the Jaynes-Cummings model and the effects of the virtual transitions will be small. In the SC regime $\hat{X}^{\pm}$ and $\hat{C}^{\pm}$ reduce to the regular squeezed magnon and qubit operators, where $\hat{X}^{+} = \hat{\alpha}$ and $\hat{C}^{+} = \hat{\sigma}^{-}$. We can therefore approximate the emission and absorption statistics to be equal to the squeezed magnon and qubit mean excitation numbers, $\langle \hat{\alpha}^{\dagger}\hat{\alpha} \rangle$ and $\langle \hat{\sigma}_i^{+}\hat{\sigma}_i^{-} \rangle$, where i accounts for the fact that we have multiple qubits.

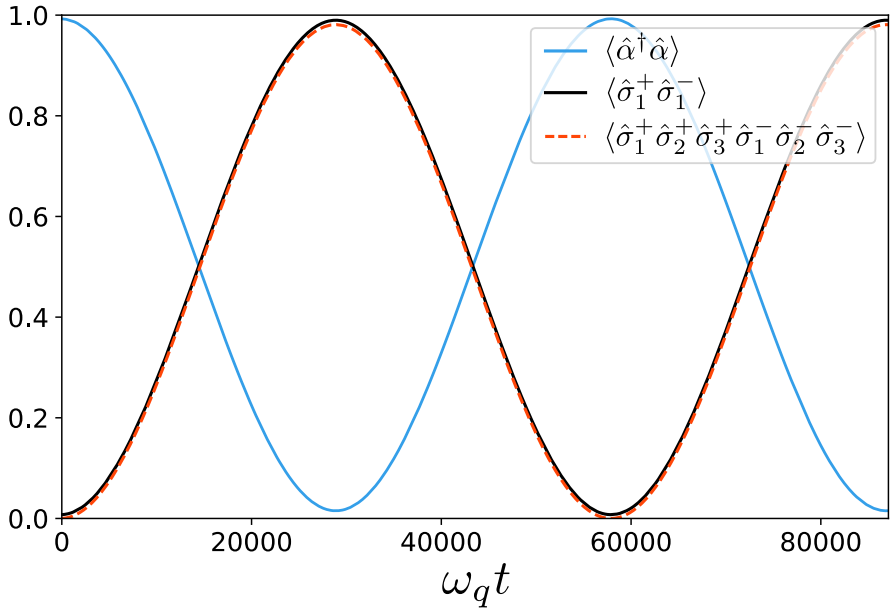

Figure 5.5: System dynamics depicting the time evolution of the squeezed magnon mean excitation number, $\langle \hat{\alpha}^{\dagger}\hat{\alpha} \rangle$ (blue solid line), the qubit mean excitation number, $\langle \hat{\sigma}_1^{+}\hat{\sigma}_1^{-} \rangle$ (black solid line), and the three-qubit zero-delay correlation function, $\langle \hat{\sigma}_1^{+}\hat{\sigma}_2^{+}\hat{\sigma}_3^{+}\hat{\sigma}_1^{-}\hat{\sigma}_2^{-}\hat{\sigma}_3^{-} \rangle$ (red dashed line). The initial state is $|\psi(0)\rangle = |1, ggg\rangle$. The mean single-qubit and squeezed magnon excitations exhibit typical Rabi oscillations, manifesting a coherent and reversible energy-transfer between the states $|1, ggg\rangle$ and $|0, eee\rangle$. The nearly perfect overlap between the single-qubit excitation number and three-qubit correlation function confirms the joint and simultaneous nature of the three-qubit excitation.

Numerically calculating the time-evolution of the system, we consider the qubits to be symmetric with a qubit frequency $\omega_q = 2\pi$ and coupling strengths $g_R = g_{CR} = 0.1\omega_q$. The squeezed magnon frequency is set to the value determined by the smallest splitting in the spectrum, $\omega_0 = 2.98498\omega_q$, to achieve the strongest possible coupling between $|1, ggg\rangle$ and $|0, eee\rangle$. The initial state is set to $|\psi(0)\rangle = |1, ggg\rangle$. To probe the nature of the transition, it is not sufficient to solely evaluate the mean excitation numbers, as these do not offer any information on specifically how the transition transpires. We therefore also calculate the coincidence rate between the transitions, in terms of the three-qubit zero-delay correlation function $\langle \hat{\sigma}_1^{+}\hat{\sigma}_2^{+}\hat{\sigma}_3^{+}\hat{\sigma}_1^{-}\hat{\sigma}_2^{-}\hat{\sigma}_3^{-} \rangle$. Furthermore, the mean qubit excitation numbers are determined by $\langle \hat{\sigma}_1^{+}\hat{\sigma}_1^{-} \rangle$. As the qubits are symmetric, there is no distinction

between calculating the mean qubit excitation number for any value of $i = 1,2,3$. The calculated dynamics of these quantities are displayed in Fig. 5.5. We observe that at the time $t' = 0$, the occupation probability of the squeezed magnon is 1 while the qubit occupation probability is 0. After a time $t' = \pi/g_{\text{eff}}$, half of a complete oscillation, $\langle \hat{\alpha}^\dagger \hat{\alpha} \rangle$ and $\langle \hat{\sigma}_1^+ \hat{\sigma}_1^- \rangle$ reach their first minimum and maximum, showing that the qubits are maximally excited when the squeezed magnon population is 0. After a time period $2\pi/g_{\text{eff}}$ the reverse transition, $|0,eee\rangle \rightarrow |1,ggg\rangle$, occurs and they have carried out a full oscillation. The observed oscillation period $2\pi/g_{\text{eff}}$ is consistent with the value of g_{eff} extracted from Eq. (5.5). This oscillatory pattern of complete population inversion continues for several periods without experiencing any kind of dephasing.

These results confirm that we have a resonant coupling between the states, leading to typical Rabi oscillations with a coherent and reversible transfer of energy between the states and with a complete population oscillation with Rabi period $2\pi/g_{\text{eff}}$. The correlation function $\langle \hat{\sigma}_1^+ \hat{\sigma}_2^+ \hat{\sigma}_3^+ \hat{\sigma}_1^- \hat{\sigma}_2^- \hat{\sigma}_3^- \rangle$ coincides nearly perfectly with the mean single-qubit excitation. This is a clear signature of the qubits being perfectly correlated and excited by the absorption of a single squeezed magnon, allowing us to exclude the possibility that the transition occurs via a down-conversion process generating multiple squeezed magnons that individually excite each qubit.

By establishing that our system enables the synchronous excitation of three qubits by a single-squeezed magnon, we furthermore demonstrate the prospect of single-step generation of maximally entangled states. After a time $t' = \pi/2g_{\text{eff}}$ of turning on the dynamics, equivalent to a $\pi/2$ pulse, the system will be in the entangled state $(|0,eee\rangle + |1,ggg\rangle)/\sqrt{2}$ which is the three-qubit GHZ state. Our system therefore presents an opportunity to circumvent the conventional way of generating GHZ states, involving complex multi-step processes reliant on careful engineering of intermediate quantum states, by generating entangled qubit states through an elementary quantum Rabi process.

As the effective coupling strength for our transition scales with $(g_{CR,R}/\omega_q)^5$ it is inevitable that by employing the system parameters chosen in this analysis, the resonant three-qubit coupling will be very weak. Such a resonant coupling would therefore not be realizable using cavity quantum electrodynamics platforms that can only reach the SC regime. However, despite our choice of parameters, motivated by the purpose of drawing comparisons to our results from perturbation theory, we have shown that the proposed systems can, through squeezing mediated coupling enhancement, achieve coupling strengths reaching into the DSC regime.

6 Conclusion

In this master's thesis, we have conducted a detailed theoretically study of a spin-qubit exchange-coupled to an anisotropic ferromagnet, focusing on its potential applications within quantum computation and communication. Specifically, the generation of maximally entangled GHZ and related states for the physical implementation of quantum error correction codes was investigated. As the magnon|spin-qubit ensemble combines the features of several disciplines, frameworks from quantum optics, cavity quantum electrodynamics and condensed matter have been employed to develop a complete theoretically description. Furthermore, due to its interdisciplinary nature, this hybrid system combines various complementary advantages of different physical disciplines into one platform.

Deriving the system Hamiltonian, it is found that for the case of an isotropic ferromagnet, the system can be described in terms of an ideal Jaynes-Cummings model. This is a result of the spin-conservation imposed by the exchange-coupling, leading to the counter-rotating terms of the generalized QRM being forbidden. Consequently, all dynamics are governed solely by rotating terms that conserve the total excitation number. The qubit and the bosonic mode can only exchange a single quantum at resonance.

When allowing anisotropy in the ferromagnet, it was demonstrated that the new eigenmodes are that of a magnon with a controllable degree of squeezing in the fluctuations of $\hat{S}_x$ and $\hat{S}_y$. The squeezed magnon vacuum comprises a superposition of even-numbered magnon Fock states, while the eigenexcitation consists of odd-numbered magnon states. As a result, we have a squeezing dependent enhanced average spin, potentially much larger than for a single magnon, depending on the value of the squeezing parameter r. Additionally, we find that the squeezed magnon mode gives rise to non-zero counter-rotating terms and that the excitation conserving and non-conserving terms of the Hamiltonian can be individually tuned. This is through the coupling strengths $g_R = g\cosh r$ and $g_{CR} = g\sinh r$, where the value of r can be conveniently engineered through the magnet anisotropies and applied magnetic field. The squeezing phenomenon is mathematically equivalent to that of squeezed states of light, but in contrast is a result of energy minimization. The proposed magnon|spin-qubit ensemble thus achieves an intrinsic coupling enhancement reaching into the DSC regime, without requiring a non-equilibrium drive.

Extending the ensuing anisotropic QRM to incorporate three qubits instead of one qubit, we find that the non-zero squeezing enables higher order virtual transitions between states that do not have the same number of excitations. Focusing on the transition $|1,ggg\rangle \rightarrow |0,eee\rangle$, the derived effective coupling scales as $(g_{CR,R}/\omega_q)^5$ by virtue of being a fifth-order process and the third-order contribution to g_{eff} cancelling at resonance. The dynamics are governed by the parity symmetry of the full Hamiltonian, and is limited exclusively to the negative parity chain of states. Numerically investigating the static properties of our system, we determine that there is a Rabi splitting between the states $|1,ggg\rangle$ and $|0,eee\rangle$ embodied

by a small avoided crossing in the energy spectrum around $\omega_0 \approx 3\omega_q$. We thus confirm that there is a resonant coupling between these states when the squeezed magnon frequency is approximately three times the qubit frequency. Additionally, we find that the perturbation of the interaction Hamiltonian introduces a shift in the energy spectrum, where an analytical expression for the corrected resonance frequency was derived using perturbation theory.

Studying the time evolution of the our anisotropic QRM from the initial state $|1, ggg\rangle$ with the system tuned into resonance, we achieve coherent and reversible Rabi oscillations between the two states, where a full population inversion occurs over the Rabi period $2\pi/g_{\text{eff}}$. Furthermore, evaluating the qubit correlation function, this perfectly coincides with the mean qubit excitation number, verifying that we have a perfectly correlated and synchronous three-qubit excitation excited by a single squeezed magnon. The magnon|spin-qubit ensemble is thus an ideal platform for generating entanglement between the qubits through a coherent process, specifically in the form of GHZ states that are fundamental in Shor's quantum error correction code.

To conclude, our magnon|spin-qubit ensemble is shown to capitalize on several unique features that combine the advantages of previous proposals. These include exploiting intrinsic magnon squeezing to generate entangled states without the need for an external non-equilibrium drive and utilizing the composite nature of the squeezed magnon for coupling-enhancement. Furthermore, by matching the ferromagnet with the spin-qubit, the proposed platform profits of an already mature fabrication technology, with the potential of scaling up into larger quantum circuits. Additionally, with the tunability of the rotating and counter-rotating terms, our system provides an ideal opportunity for investigating novel phenomena in the USC regime and transitioning into the DSC regime. Overall, our proposal is a promising platform for implementation of quantum computing protocols and the manipulation of qubit or bosonic field states.

The parameters used in the numerical analysis in this thesis were chosen with the objective of comparing the results with those obtained using perturbation theory. The coupling strengths were therefore $g_R = g_{CR} = 0.1\omega_q$, in between the SC and USC regime. For further work, it is therefore of interest to extend the analysis to higher parameter regimes to investigate the features of our anisotropic QRM. This involves further exploring the potential properties that come from the tunability of the rotating and counter-rotating terms, by studying the static and dynamic properties of the system when these have different values. This will also entail determining the potential impact of seventh-order contributions in perturbation theory, as well as additional corrections to third and fifth-order. It is also expected that a numerical fitting procedure of the splitting value incorporating a third term, $Cg_R^2 g_{CR}$, will provide an expression for g_{eff} that is more consistent in higher parameter regimes.

Acronyms

RWA rotating wave approximation

QRM quantum Rabi model

SC strong-coupling

USC ultra-strong coupling

DSC deep-strong coupling

GHZ Greenberger-Horne-Zeilinger

Bibliography

[1] I. I. Rabi. On the Process of Space Quantization. *Phys. Rev.*, **49**:324–328, Feb 1936. doi: 10.1103/PhysRev.49.324.

[2] I. I. Rabi. Space Quantization in a Gyrating Magnetic Field. *Phys. Rev.*, **51**:652–654, Apr 1937. doi: 10.1103/PhysRev.51.652.

[3] S. Haroche and J. M. Raimond. *Exploring the Quantum : Atoms, Cavities and Photons*. Oxford graduate texts. Oxford University Press, Oxford, 2006. ISBN 0198509146.

[4] M. Fox. *Quantum Optics: An Introduction*. Oxford master series in physics. Oxford University Press, Incorporated, Oxford, 2006. ISBN 9780198566731.

[5] P. Forn-Díaz, L. Lamata, E. Rico, J. Kono, and E. Solano. Ultrastrong coupling regimes of light-matter interaction. *Rev. Mod. Phys.*, **91**:025005, Jun 2019. doi: 10.1103/RevModPhys.91.025005.

[6] D. Braak. Integrability of the Rabi Model. *Phys. Rev. Lett.*, **107**:100401, Aug 2011. doi: 10.1103/PhysRevLett.107.100401.

[7] C. C. Gerry and P. L. Knight. *Introductory Quantum Optics*. Cambridge University Press, Cambridge, 2005. ISBN 0521820359.

[8] S. Ashhab and F. Nori. Qubit-oscillator systems in the ultrastrong-coupling regime and their potential for preparing nonclassical states. *Phys. Rev. A*, **81**:042311, Apr 2010. doi: 10.1103/PhysRevA.81.042311.

[9] T. Niemczyk, F. Deppe, H. Huebl, E. P. Menzel, F. Hocke, M. J. Schwarz, J. J. Garcia-Ripoll, D. Zueco, T. Hümmer, E. Solano, et al. Circuit quantum electrodynamics in the ultrastrong-coupling regime. *Nature Physics*, **6**(10):772–776, 2010. doi: https://doi.org/10.1038/nphys1730.

[10] F. Yoshihara, T. Fuse, S. Ashhab, K. Kakuyanagi, S. Saito, and K. Semba. Superconducting qubit–oscillator circuit beyond the ultrastrong-coupling regime. *Nature Physics*, **13**(1):44–47, 2017. doi: https://doi.org/10.1038/nphys3906.

[11] Z. Chen, Y. Wang, T. Li, L. Tian, Y. Qiu, K. Inomata, F. Yoshihara, S. Han, F. Nori, J. S. Tsai, and J. Q. You. Single-photon-driven high-order sideband transitions in an ultrastrongly coupled circuit-quantum-electrodynamics system. *Phys. Rev. A*, **96**:012325, Jul 2017. doi: 10.1103/PhysRevA.96.012325.

[12] J. Braumüller, M. Marthaler, A. Schneider, A. Stehli, H. Rotzinger, M. Weides, and A. V. Ustinov. Analog quantum simulation of the Rabi model in the ultra-strong coupling regime. *Nature communications*, **8** (1):1–8, 2017. doi: https://doi.org/10.1038/s41467-017-00894-w.

[13] P. Forn-Díaz, J. J. García-Ripoll, B. Peropadre, J. L. Orgiazzi, M. A. Yurtalan, R. Belyansky, C. M. Wilson, and A. Lupascu. Ultrastrong coupling of a single artificial atom to an electromagnetic continuum in the nonperturbative regime. *Nature Physics*, **13**(1):39–43, 2017. doi: https://doi.org/10.1038/nphys3905.

[14] X. Li, M. Bamba, Q. Zhang, S. Fallahi, G. C. Gardner, W. Gao, M. Lou, K. Yoshioka, M. J. Manfra, and J. Kono. Vacuum Bloch–Siegert shift in Landau polaritons with ultra-high cooperativity. *Nature Photonics*, **12**(6):324–329, 2018. doi: https://doi.org/10.1038/s41566-018-0153-0.

[15] D. Lv, S. An, Z. Liu, J. N. Zhang, J. S. Pedernales, L. Lamata, E. Solano, and K. Kim. Quantum Simulation of the Quantum Rabi Model in a Trapped Ion. *Phys. Rev. X*, **8**:021027, Apr 2018. doi: 10.1103/PhysRevX.8.021027.

[16] L. Garziano, R. Stassi, V. Macrì, A. F. Kockum, S. Savasta, and F. Nori. Multiphoton quantum Rabi oscillations in ultrastrong cavity QED. *Phys. Rev. A*, **92**:063830, Dec 2015. doi: 10.1103/PhysRevA.92.063830.

[17] K. K. W. Ma and C. K. Law. Three–photon resonance and adiabatic passage in the large-detuning Rabi model. *Phys. Rev. A*, **92**:023842, Aug 2015. doi: 10.1103/PhysRevA.92.023842.

[18] L. Garziano, V. Macrì, R. Stassi, O. Di Stefano, F. Nori, and S. Savasta. One Photon Can Simultaneously Excite Two or More Atoms. *Phys. Rev. Lett.*, **117**:043601, Jul 2016. doi: 10.1103/PhysRevLett.117.043601.

[19] M. A. Nielsen and I. L. Chuang. *Quantum Computation and Quantum Information*. Cambridge University Press, Cambridge, 10th anniversary edition, 2010. ISBN 9781107002173.

[20] S. Wehner, D. Elkouss, and R. Hanson. Quantum internet: A vision for the road ahead. *Science*, **362** (6412), 2018. doi: 10.1126/science.aam9288.

[21] A. Laucht, F. Hohls, N. Ubbelohde, M. F. Gonzalez-Zalba, D. J. Reilly, S. Stobbe, T. Schröder, P. Scarlino, J. V. Koski, A. Dzurak, et al. Roadmap on quantum nanotechnologies. *Nanotechnology*, **32**(16):162003, 2021. doi: https://doi.org/10.1088/1361-6528/abb333.

[22] G. Romero, D. Ballester, Y. M. Wang, V. Scarani, and E. Solano. Ultrafast Quantum Gates in Circuit QED. *Phys. Rev. Lett.*, **108**:120501, Mar 2012. doi: 10.1103/PhysRevLett.108.120501.

[23] T. H. Kyaw, D. A. Herrera-Martí, E. Solano, G. Romero, and L.-C. Kwek. Creation of quantum error correcting codes in the ultrastrong coupling regime. *Phys. Rev. B*, **91**:064503, Feb 2015. doi: 10.1103/PhysRevB.91.064503.

[24] D. Z. Rossatto, S. Felicetti, H. Eneriz, E. Rico, M. Sanz, and E. Solano. Entangling polaritons via dynamical Casimir effect in circuit quantum electrodynamics. *Phys. Rev. B*, **93**:094514, Mar 2016. doi: 10.1103/PhysRevB.93.094514.

[25] G. Wang, R. Xiao, H. Z. Shen, C. Sun, and K. Xue. Simulating Anisotropic quantum Rabi model via frequency modulation. *Scientific reports*, **9**(1):1–11, 2019. doi: https://doi.org/10.1038/s41598-019-40899-7.

[26] C. S. Muñoz, A. F. Kockum, A. Miranowicz, and F. Nori. Simulating ultrastrong-coupling processes breaking parity conservation in Jaynes-Cummings systems. *Phys. Rev. A*, **102**:033716, Sep 2020. doi: 10.1103/PhysRevA.102.033716.

[27] M. Wallquist, K. Hammerer, P. Rabl, M. Lukin, and P. Zoller. Hybrid quantum devices and quantum engineering. *Physica Scripta*, **2009**(T137):014001, Dec 2009. doi: 10.1088/0031-8949/2009/t137/014001.

[28] L. M. K. Vandersypen and M. A. Eriksson. Quantum computing with semiconductor spins. *Physics Today*, **72**:8–38, 2019. doi: https://doi.org/10.1063/PT.3.4270.

[29] C. Nayak, S. H. Simon, A. Stern, M. Freedman, and S. Das Sarma. Non-Abelian anyons and topological quantum computation. *Rev. Mod. Phys.*, **80**:1083–1159, Sep 2008. doi: 10.1103/RevModPhys.80.1083.

[30] P. W. Shor. Scheme for reducing decoherence in quantum computer memory. *Phys. Rev. A*, **52**: R2493–R2496, Oct 1995. doi: 10.1103/PhysRevA.52.R2493.

[31] D. M. Greenberger, M. A. Horne, and A. Zeilinger. Going Beyond Bell's Theorem. arXiv:0712.0921 [quanth-ph], 2007. URL `https://arxiv.org/abs/0712.0921`.

[32] T. Aoki, G. Takahashi, T. Kajiya, J. Yoshikawa, S. L. Braunstein, P. Van Loock, and A. Furusawa. Quantum error correction beyond qubits. *Nature Physics*, **5**(8):541–546, 2009. doi: https://doi.org/10.1038/nphys1309.

[33] G. J. Milburn and S. L. Braunstein. Quantum teleportation with squeezed vacuum states. *Phys. Rev. A*, **60**:937–942, Aug 1999. doi: 10.1103/PhysRevA.60.937.

[34] R. Schnabel. Squeezed states of light and their applications in laser interferometers. *Physics Reports*, **684**:1–51, 2017. ISSN 0370-1573. doi: https://doi.org/10.1016/j.physrep.2017.04.001.

[35] W. Qin, A. Miranowicz, P. B. Li, X. Y. Lü, J. Q. You, and F. Nori. Exponentially Enhanced Light-Matter Interaction, Cooperativities, and Steady-State Entanglement Using Parametric Amplification. *Phys. Rev. Lett.*, **120**:093601, Mar 2018. doi: 10.1103/PhysRevLett.120.093601.

[36] C. Leroux, L. C. G. Govia, and A. A. Clerk. Enhancing Cavity Quantum Electrodynamics via Antisqueezing: Synthetic Ultrastrong Coupling. *Phys. Rev. Lett.*, **120**:093602, Mar 2018. doi: 10.1103/PhysRevLett.120.093602.

[37] A. Kamra and W. Belzig. Super-Poissonian Shot Noise of Squeezed-Magnon Mediated Spin Transport. *Phys. Rev. Lett.*, **116**:146601, Apr 2016. doi: 10.1103/PhysRevLett.116.146601.

[38] A. Kamra, W. Belzig, and A. Brataas. Magnon-squeezing as a niche of quantum magnonics. *Applied Physics Letters*, **117**(9):090501, 2020. doi: https://doi.org/10.1063/5.0021099.

[39] I. C. Skogvoll. The Quantum Rabi Model: Strong to Deep-Strong Coupling. Specialization project report in TFY4520, Department of Physics - Norwegian University of Science and Technology. Dec 2020.

[40] P. C. Hemmer. *Kvantemekanikk*. Tapir akademisk forl, Trondheim, 5. edition, 2005. ISBN 8251920280.

[41] J. Linder. *Intermediate Quantum Mechanics*. 1. edition, 2017. ISBN 9788740317831.

[42] J. J Sakurai. *Modern Quantum Mechanics*. Cambridge University Press, Cambridge, 2. edition, 2017. ISBN 9781108422413.

[43] M. O. Scully and M. S. Zubairy. *Quantum Optics*. Cambridge University Press, Cambridge, 1997. ISBN 0521434580.

[44] J. Zhao, L. Qin, X. Cai, Q. Lin, and Z. Wang. Parity chain and parity chain breaking in the two-level cavity quantum electrodynamics system. *Chin. Opt. Lett.*, **15**(5):050202, May 2017. URL `http://col.osa.org/abstract.cfm?URI=col-15-5-050202`.

[45] J. Casanova, G. Romero, I. Lizuain, J. J. García-Ripoll, and E. Solano. Deep Strong Coupling Regime of the Jaynes-Cummings Model. *Phys. Rev. Lett.*, **105**:263603, Dec 2010. doi: 10.1103/PhysRevLett.105.263603.

[46] E. T. Jaynes and F. W. Cummings. Comparison of quantum and semiclassical radiation theories with application to the beam maser. *Proceedings of the IEEE*, **51**(1):89–109, 1963. doi: 10.1109/PROC.1963.1664.

[47] D. Z. Rossatto, C. J. Villas-Bôas, M. Sanz, and E. Solano. Spectral classification of coupling regimes in the quantum Rabi model. *Phys. Rev. A*, **96**:013849, Jul 2017. doi: 10.1103/PhysRevA.96.013849.

[48] D. Braak. Symmetries in the Quantum Rabi Model. *Symmetry*, **11**(10), 2019. ISSN 2073-8994. URL `https://www.mdpi.com/2073-8994/11/10/1259`.

[49] P. Forn-Díaz, J. Lisenfeld, D. Marcos, J. J. García-Ripoll, E. Solano, C. J. P. M. Harmans, and J. E. Mooij. Observation of the Bloch-Siegert Shift in a Qubit-Oscillator System in the Ultrastrong Coupling Regime. *Phys. Rev. Lett.*, **105**:237001, Nov 2010. doi: 10.1103/PhysRevLett.105.237001.

[50] S. Gambino, M. Mazzeo, A. Genco, O. Di Stefano, S. Savasta, S. Patanè, D. Ballarini, F. Mangione, G. Lerario, D. Sanvitto, et al. Exploring Light–Matter Interaction Phenomena under Ultrastrong Coupling Regime. *ACS Photonics*, **1**(10):1042–1048, 2014. doi: 10.1021/ph500266d.

[51] D. Braak, Q. H. Chen, M. T. Batchelor, and E. Solano. Semi-classical and quantum Rabi models: in celebration of 80 years. *Journal of Physics A: Mathematical and Theoretical*, **49**(30):300301, Jun 2016. doi: 10.1088/1751-8113/49/30/300301.

[52] F. Yoshihara, T. Fuse, Z. Ao, S. Ashhab, K. Kakuyanagi, S. Saito, T. Aoki, K. Koshino, and K. Semba. Inversion of Qubit Energy Levels in Qubit-Oscillator Circuits in the Deep-Strong-Coupling Regime. *Phys. Rev. Lett.*, **120**:183601, May 2018. doi: 10.1103/PhysRevLett.120.183601.

[53] N. S. Mueller, Y. Okamura, B. G. M. Vieira, S. Juergensen, H. Lange, E. B. Barros, F. Schulz, and S. Reich. Deep strong light–matter coupling in plasmonic nanoparticle crystals. *Nature*, **583**(7818):780–784, 2020. doi: https://doi.org/10.1038/s41586-020-2508-1.

[54] W. Nolting and A. Ramakanth. *Quantum Theory of Magnetism*. Springer Berlin / Heidelberg, Berlin, Heidelberg, 2009. ISBN 3540854150.

[55] T. Holstein and H. Primakoff. Field Dependence of the Intrinsic Domain Magnetization of a Ferromagnet. *Phys. Rev.*, **58**:1098–1113, Dec 1940. doi: 10.1103/PhysRev.58.1098.

[56] C. Kittel. *Quantum Theory of Solids*. Wiley, New York, 1963. ISBN 0471490253.

[57] D. D. Stancil and A. Prabhakar. *Spin Waves: Theory and Applications*. Springer-Verlag, New York, NY, 1. edition, 2009. ISBN 9780387778648.

[58] J. Medford, J. Beil, J. M. Taylor, E. I. Rashba, H. Lu, A. C. Gossard, and C. M. Marcus. Quantum-Dot-Based Resonant Exchange Qubit. *Phys. Rev. Lett.*, **111**:050501, Jul 2013. doi: 10.1103/PhysRevLett.111.050501.

[59] F. H. L. Koppens, C. Buizert, K. J. Tielrooij, I. T. Vink, K. C. Nowack, T. Meunier, L. P. Kouwenhoven, and L. M. K. Vandersypen. Driven coherent oscillations of a single electron spin in a quantum dot. *Nature*, **442**(7104):766–771, 2006. doi: https://doi.org/10.1038/nature05065.

[60] D. Loss and D. P. DiVincenzo. Quantum computation with quantum dots. *Phys. Rev. A*, **57**:120–126, Jan 1998. doi: 10.1103/PhysRevA.57.120.

[61] E. A. Laird, J. M. Taylor, D. P. DiVincenzo, C. M. Marcus, M. P. Hanson, and A. C. Gossard. Coherent spin manipulation in an exchange-only qubit. *Phys. Rev. B*, **82**:075403, Aug 2010. doi: 10.1103/PhysRevB.82.075403.

[62] D. Press, T. D. Ladd, B. Zhang, and Y. Yamamoto. Complete quantum control of a single quantum dot spin using ultrafast optical pulses. *Nature*, **456**(7219):218–221, 2008. doi: https://doi.org/10.1038/nature07530.

[63] S. J. Devitt, W. J. Munro, and K. Nemoto. Quantum error correction for beginners. *Reports on Progress in Physics*, **76**(7):076001, Jun 2013. doi: 10.1088/0034-4885/76/7/076001.

[64] Y. Kajiwara, K. Harii, S. Takahashi, J. Ohe, K. Uchida, M. Mizuguchi, H. Umezawa, H. Kawai, K. Ando, K. Takanashi, et al. Transmission of electrical signals by spin-wave interconversion in a magnetic insulator. *Nature*, **464**(7286):262–266, 2010. doi: https://doi.org/10.1038/nature08876.

[65] A. Kamra and W. Belzig. Magnon-mediated spin current noise in ferromagnet | nonmagnetic conductor hybrids. *Phys. Rev. B*, **94**:014419, Jul 2016. doi: 10.1103/PhysRevB.94.014419.

[66] S. Takahashi, E. Saitoh, and S. Maekawa. Spin current through a normal-metal/insulating-ferromagnet junction. *Journal of Physics: Conference Series*, **200**(6):062030, Jan 2010. doi: 10.1088/1742-6596/200/6/062030.

[67] S. A. Bender and Y. Tserkovnyak. Interfacial spin and heat transfer between metals and magnetic insulators. *Phys. Rev. B*, **91**:140402, Apr 2015. doi: 10.1103/PhysRevB.91.140402.

[68] P. Bruno. Spin-wave theory of two-dimensional ferromagnets in the presence of dipolar interactions and magnetocrystalline anisotropy. *Phys. Rev. B*, **43**:6015–6021, Mar 1991. doi: 10.1103/PhysRevB.43.6015.

[69] A. L. Fetter and D. Walecka. *Quantum Theory of Many-Particle Systems*. Dover Publications, Mineola, N.Y, 2003. ISBN 0486428273.

[70] M. M. Nieto. Displaced and squeezed number states. *Physics Letters A*, **229**(3):135–143, May 1997. ISSN 0375-9601. doi: 10.1016/s0375-9601(97)00183-7.

[71] G. S. Agarwal. *Quantum Optics*. Cambridge University Press, 2012. ISBN 9781139035170. doi: https://doi.org/10.1017/CBO9781139035170.

[72] Q. Xie, H. Zhong, M. T. Batchelor, and C. Lee. The quantum Rabi model: solution and dynamics. *Journal of Physics A: Mathematical and Theoretical*, **50**(11):113001, Feb 2017. doi: 10.1088/1751-8121/aa5a65.

[73] F. T. Hioe. Phase Transitions in Some Generalized Dicke Models of Superradiance. *Phys. Rev. A*, **8**: 1440–1445, Sep 1973. doi: 10.1103/PhysRevA.8.1440.

[74] Y. Wang, W. L. You, M. Liu, Y. L. Dong, H. G. Luo, G. Romero, and J. Q. You. Quantum criticality and state engineering in the simulated anisotropic quantum rabi model. *New Journal of Physics*, **20**(5):053061, May 2018. doi: 10.1088/1367-2630/aac5b5.

[75] A. Kamra, E. Thingstad, G. Rastelli, R. A. Duine, A. Brataas, W. Belzig, and A. Sudbø. Antiferromagnetic magnons as highly squeezed fock states underlying quantum correlations. *Phys. Rev. B*, **100**:174407, Nov 2019. doi: 10.1103/PhysRevB.100.174407.

[76] Y. Tabuchi, S. Ishino, T. Ishikawa, R. Yamazaki, K. Usami, and Y. Nakamura. Hybridizing Ferromagnetic Magnons and Microwave Photons in the Quantum Limit. *Phys. Rev. Lett.*, **113**:083603, Aug 2014. doi: 10.1103/PhysRevLett.113.083603.

[77] M. Neeley, R. C. Bialczak, M. Lenander, E. Lucero, M. Mariantoni, A. D. O'connell, D. Sank, H. Wang, M. Weides, J. Wenner, et al. Generation of three-qubit entangled states using superconducting phase qubits. *Nature*, **467**(7315):570–573, 2010. doi: https://doi.org/10.1038/nature09418.

[78] Y. D. Wang, S. Chesi, D. Loss, and C. Bruder. One-step multiqubit Greenberger-Horne-Zeilinger state generation in a circuit QED system. *Phys. Rev. B*, **81**:104524, Mar 2010. doi: 10.1103/PhysRevB.81.104524.

[79] L. Mao, S. Huai, and Y. Zhang. The two-qubit quantum Rabi model: inhomogeneous coupling. *Journal of Physics A: Mathematical and Theoretical*, **48**(34):345302, Aug 2015. doi: 10.1088/1751-8113/48/34/345302.

[80] W. R. Salzman. Diagrammatical Derivation and Representation of Rayleigh–Schrödinger Perturbation Theory. *The Journal of Chemical Physics*, **49**(7):3035–3040, 1968. doi: https://doi.org/10.1063/1.1670546.

[81] J. R. Johansson, P. D. Nation, and F. Nori. QuTiP: An open-source Python framework for the dynamics of open quantum systems. *Computer Physics Communications*, **183**(8):1760 – 1772, 2012. ISSN 0010-4655. doi: https://doi.org/10.1016/j.cpc.2012.02.021.

[82] J. R. Johansson, P. D. Nation, and F. Nori. QuTiP 2: A Python framework for the dynamics of open quantum systems. *Computer Physics Communications*, **184**(4):1234 – 1240, 2013. ISSN 0010-4655. doi: https://doi.org/10.1016/j.cpc.2012.11.019.

[83] A. Ridolfo, M. Leib, S. Savasta, and M. J. Hartmann. Photon Blockade in the Ultrastrong Coupling Regime. *Phys. Rev. Lett.*, **109**:193602, Nov 2012. doi: 10.1103/PhysRevLett.109.193602.

[84] R. J. Glauber. The Quantum Theory of Optical Coherence. *Phys. Rev.*, **130**:2529–2539, Jun 1963. doi: 10.1103/PhysRev.130.2529.

A Manuscript for research article

The following is the manuscript for the research article “Tunable anisotropic quantum Rabi model via magnon|spin-qubit ensemble”, which was carried out as part of this master’s thesis. It is currently under review at the time of this writing. The Supplemental Materials accompanying the manuscript can be found in appendix B.

Tunable anisotropic quantum Rabi model via magnon|spin-qubit ensemble

Ida C. Skogvoll,[1] Jonas Lidal,[1] Jeroen Danon,[1] and Akashdeep Kamra[2,1,*]

[1] *Center for Quantum Spintronics, Department of Physics, Norwegian University of Science and Technology, NO-7491 Trondheim, Norway*

[2] *Condensed Matter Physics Center (IFIMAC) and Departamento de Física Teórica de la Materia Condensada, Universidad Autónoma de Madrid, E-28049 Madrid, Spain*

The ongoing rapid progress towards quantum technologies relies on and strives for new hybrid platforms optimized for specific quantum computation and communication tasks. We theoretically study a spin qubit exchange-coupled to an anisotropic ferromagnet that hosts magnons with a controllable degree of intrinsic squeezing. We find this system to physically realize the quantum Rabi model from isotropic to the Jaynes-Cummings limit with coupling strengths that can foray into the deep-strong regime. We demonstrate that the composite nature of the squeezed-magnon enables concurrent excitation of 3 spin qubits coupled to the same magnet. Thus, 3-qubit Greenberger-Horne-Zeilinger and related states needed for implementing Shor's quantum error correction code can be robustly generated. Our analysis highlights some unique advantages offered by this hybrid platform and hopes to motivate corresponding experimental efforts.

Introduction.—A bosonic mode interacting with a two-level system constitutes the paradigmatic quantum Rabi model (QRM) employed in understanding light-matter interaction [1, 2]. The recent theoretical discovery of its integrability [3] and increasing coupling strengths realized in experiments have brought the QRM into a sharp focus [4, 5]. It also models a qubit interacting with an electromagnetic mode, a key ingredient for quantum communication and distant qubit-qubit coupling [6–9]. Thus, the ongoing quantum information revolution [6, 10] capitalizes heavily on the advancements in physically realizing and theoretically understanding the QRM. In particular, larger coupling strengths are advantageous for faster gate operations on qubits, racing against imminent decoherence. Generating squeezed states of the bosonic mode [11, 12], typically light, via parametric amplification has emerged as a nonequilibrium means of strengthening this coupling [13, 14]. Other related methods [15, 16] that exploit drives to control, for example, the QRM anisotropy [4] have also been proposed.

Contemporary digital electronics relies heavily on the very-large-scale integration of the same silicon-based circuits. In sharp contrast, emerging quantum information technologies benefit from multiple physical realizations of qubits and their interconnects in order to choose the best platform for implementing a specific task or computation [6, 8, 17–20]. Fault-tolerant quantum computing, either via less error-prone qubits [21] or via implementation of quantum error correction [22–24], is widely seen as the path forward. A paradigmatic error correction code [22] put forth by Shor requires encoding one logical qubit into 9 physical qubits and generating 3-qubit Greenberger–Horne–Zeilinger (GHZ) [25] and related states. A continuous-variable analog of this code employing squeezed states of light has been experimentally demonstrated [26]. This has spurred fresh hopes of fault-tolerant quantum computing and demonstrated the bosonic modes as more than just interconnects for qubits.

In our discussion above, we have encountered squeezed states of light in multiple contexts. These nonequilibrium states, bearing widespread applications from metrology [27] to quantum teleportation [28, 29], decay with time. In contrast, the bosonic normal modes - magnons - in anisotropic ferromagnets were recently shown to be squeezed [30] and embody various quantum features inherent to such squeezed states [11, 31–33]. Being equilibrium in nature, these are also somewhat different from light and require care when making comparisons. This calls for examining ways in which we can exploit the robust equilibrium-squeezed nature of magnons in addressing challenges facing emerging quantum technologies [20, 34, 35]. The spin qubit [18, 19, 36] becomes the perfect partner because of its potential silicon-based nature, feasibility of a strong exchange-coupling to the magnet, reliance on a mature fabrication technology and so on.

Here, we theoretically study a ferromagnet exchange-coupled to a spin qubit. We find the ensuing magnon|qubit ensemble to combine various complementary advantages mentioned above into one promising platform. We show that this system realizes an ideal Jaynes-Cummings model, enabled by spin conservation in the system that forbids the counter rotating terms (CRTs) by symmetry. Allowing anisotropy in the magnet, the squeezed-magnon [30, 31] becomes the normal mode giving rise to nonzero and controllable CRTs. The squeezed nature of the magnon further leads to an enhancement in the coupling strength, without the need for a nonequilibrium drive. Considering three spin qubits coupled to the same ferromagnet, we theoretically demonstrate the simultaneous and resonant excitation of the three qubits via a single squeezed-magnon. Thus, the system enables a robust means to generate the entangled 3-qubit GHZ and related states that underlie Shor's error correction code [22]. The magnon-spin qubit ensemble

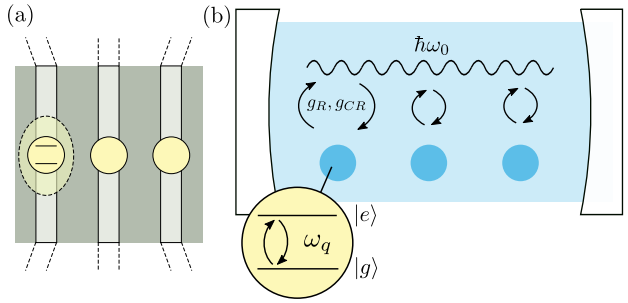

FIG. 1. Schematic depiction of 3 spin qubits exchange-coupled to 1 magnon mode. (a) Semiconducting wires hosting the localized electronic states that constitute the spin qubit are deposited on top of a thin insulating ferromagnet layer. A direct contact enables strong interfacial exchange coupling. (b) The corresponding anisotropic QRM. Three qubits interact with a single magnonic mode via controllably strong rotating (g_R) and counter-rotating (g_{CR}) terms [Eq. (9)].

offers an optimal platform for realizing the QRM with large coupling strengths and implementing fault-tolerant quantum computing protocols.

1 magnonic mode coupled to 1 qubit.—We consider a thin film of an insulating ferromagnet that acts as a magnonic cavity. Considering an applied magnetic field $H_0\hat{\boldsymbol{z}}$, the ferromagnetic Hamiltonian is expressed as [37]:

$$\tilde{H}_{\rm F} = -J\sum_{\langle i,j\rangle}\tilde{\boldsymbol{S}}_i\cdot\tilde{\boldsymbol{S}}_j + |\gamma|\mu_0 H_0\sum_i \tilde{S}_{iz}, \tag{1}$$

where J (>0) parametrizes ferromagnetic exchange between the nearest neighbors, γ (<0) is the gyromagnetic ratio, and $\tilde{\boldsymbol{S}}_i$ denotes the spin operator at position i. We set $\hbar = 1$ throughout and identify operators with an overhead tilde. A detailed derivation of the system Hamiltonian is presented in the Supplemental Material (SM) [38]. In its ground state, the ferromagnet has all its spins pointing along $-\hat{\boldsymbol{z}}$. Employing Holstein-Primakoff transformations [39] and switching to Fourier space, the ferromagnetic Hamiltonian is written in terms of spin-1 magnons [38]:

$$\tilde{H}_{\rm F} = \text{const.} + \sum_{\boldsymbol{k}}\left(\omega_0 + c_l JSa^2k^2\right)\tilde{a}^\dagger_{\boldsymbol{k}}\tilde{a}_{\boldsymbol{k}}, \tag{2}$$

where $\omega_0 \equiv |\gamma|\mu_0 H_0$ is the ferromagnetic resonance frequency ($\sim$ GHz) corresponding to the uniform ($\boldsymbol{k}=\boldsymbol{0}$) magnon mode, a is the lattice constant, S is the spin, c_l is a factor that depends on the considered lattice, $\tilde{a}_{\boldsymbol{k}}$ denotes the annihilation operator for a magnon with wavevector $\boldsymbol{k}$. The boundary conditions for small magnets result in a discrete magnon spectrum [40]. For typical values of J, spatial dimensions in the μm range result in the magnon energies differing by a few GHz. Hence, we consider only the $\boldsymbol{k}=\boldsymbol{0}$ mode henceforth, denoting $\tilde{a}_{\boldsymbol{0}}$ simply as $\tilde{a}$. We may disregard the higher modes as we exploit coherent resonant interactions in this study.

As depicted in Fig. 1(a), the confined electron gas that becomes a spin qubit is interfaced directly with the ferromagnet to enable exchange-coupling [41–44]:

$$\tilde{H}_{\rm int} = J_{\rm int}\sum_l \tilde{\boldsymbol{S}}_l\cdot\tilde{\boldsymbol{s}}_l, \tag{3}$$

where $J_{\rm int}$ parameterizes the interfacial exchange interaction, $\tilde{\boldsymbol{s}}_l$ denotes the spin operator of the spin qubit electronic state at site l, and l runs over the interfacial sites. In terms of the relevant eigenmodes, the interfacial interaction is simplified as [38]:

$$\tilde{H}_{\rm int} = g\left(\tilde{a}^\dagger\tilde{\sigma}_- + \tilde{a}\tilde{\sigma}_+\right), \tag{4}$$

where $g = J_{\rm int}N_{\rm int}|\psi|^2\sqrt{S/(2N_F)}$, with $N_{\rm int}$ the number of interfacial sites, $|\psi|^2$ the spin qubit electron probability averaged over the interface [38], and N_F the total number of sites in the ferromagnet. $\tilde{\sigma}_{+,-} = (\tilde{\sigma}_x \pm i\tilde{\sigma}_y)/2$ excite or relax the spin qubit that is further described via:

$$\tilde{H}_{\rm q} = \frac{\omega_q}{2}\tilde{\sigma}_z. \tag{5}$$

Thus, our total Hamiltonian becomes

$$\tilde{H}_1 = \tilde{H}_{\rm F} + \tilde{H}_{\rm q} + \tilde{H}_{\rm int}, \tag{6}$$

where $\tilde{H}_{\rm F} = \omega_0\tilde{a}^\dagger\tilde{a}$ and the other contributions are given by Eqs. (4) and (5).

Our system thus realizes the Jaynes-Cummings Hamiltonian [Eq. (6)] that conserves the total number of excitations. This is a direct consequence of spin conservation afforded by the exchange-coupling in our system. A spin-1 magnon can be absorbed by a spin qubit flipping the latter from its spin $-1/2$ to $+1/2$ state. The same transition in the spin qubit, however, cannot emit a magnon. This is in contrast with the case of dipolar coupling between the spin qubit and the ferromagnet [7, 37, 44–46], which does not necessarily conserve spin. Further, as numerically estimated below, on account of exchange being a much stronger interaction, the effective coupling g in our system can exceed the magnon frequency ω_0 thereby covering the full coupling range from weak to deep-strong [47–49]. Nonclassical behavior is typically manifested starting with ultrastrong couplings $g/\omega_0 > 0.1$ [47, 50, 51].

We have considered the ferromagnet to be isotropic thus far. However, such films manifest a strong shape anisotropy, in addition to potential magnetocrystalline anisotropies [37]. We now include such effects by adding the following term to the ferromagnet Hamiltonian:

$$\tilde{H}_{\rm an} = \sum_i K_x\left(\tilde{S}_{ix}\right)^2 + K_y\left(\tilde{S}_{iy}\right)^2 + K_z\left(\tilde{S}_{iz}\right)^2,$$

which results in the following magnon Hamiltonian, retaining only the uniform mode:

$$\tilde{H}_{\rm F} = A\tilde{a}^\dagger\tilde{a} + B\left(\tilde{a}^2 + \tilde{a}^{\dagger 2}\right), \tag{7}$$

with $A \equiv |\gamma|\mu_0 H_0 + K_x S + K_y S - 2K_z S$ and $B \equiv S(K_x - K_y)/2$. The ensuing Hamiltonian possesses the squeezing terms $\propto B$ which, unlike in the case of light, result from the magnet trying to minimize its ground state energy while respecting the Heisenberg uncertainty principle [31]. The new eigenmode, dubbed squeezed-magnon [30], is obtained via a Bogoliubov transform $\tilde{a} = \cosh r\tilde{\alpha} + \sinh r\tilde{\alpha}^\dagger$ resulting in

$$\tilde{H}_{\rm F} = \omega_0\tilde{\alpha}^\dagger\tilde{\alpha}, \tag{8}$$

where we continue to denote the eigenmode energy as ω_0, which now becomes $\omega_0 = \sqrt{A^2 - 4B^2}$. Further, the squeeze parameter r is governed by the relation $\sinh r = -2B/\sqrt{(A+\omega_0)^2 - 4B^2}$ [52]. In the new eigenbasis, we obtain:

$$\tilde{H}_{\rm int} = g_R\left(\tilde{\alpha}^\dagger\tilde{\sigma}_- + \tilde{\alpha}\tilde{\sigma}_+\right) + g_{CR}\left(\tilde{\alpha}^\dagger\tilde{\sigma}_+ + \tilde{\alpha}\tilde{\sigma}_-\right), \tag{9}$$

with $g_R = g\cosh r$ and $g_{CR} = g\sinh r$. The interaction now bears both rotating ($\propto g_R$) and counter-rotating ($\propto g_{CR}$) terms [Fig. 1(b)].

Our system can be analyzed in terms of two different bases: using spin-1 magnon (represented by $\tilde{a}$) or squeezed-magnon ($\tilde{\alpha}$). The latter is the eigenmode and is comprised of a superposition of odd magnon-number states [Fig. 2(a)] [30, 31, 53, 54]. Since a spin-1 magnon is associated with the physical spin-flip in the magnet [39], the interaction Eq. (4) is still comprised of absorption and emission of magnons ($\tilde{a}$) accompanied by transitions in the qubit. On the other hand, in the eigenbasis, the qubit is now interacting with a new bosonic eigenmode - the squeezed-magnon ($\tilde{\alpha}$) via an interaction bearing rotating and CRTs [Eq. (9)]. Therefore, in the eigenbasis, our system accomplishes an anisotropic QRM [4, 5] [Fig. 1(b)] - Eqs. (5), (6), (8), and (9). The squeeze parameter r, tunable via applied field and anisotropies [55], further enhances the coupling strength and controls the relative importance of the rotating and CRTs: $g_R = g\cosh r$ and $g_{CR} = g\sinh r$.

1 magnonic mode coupled to 3 qubits.—We now exploit the squeezed and composite nature of the magnonic eigenmode in generating useful entangled states [31]. As depicted in Fig. 2(a), the composite nature of the squeezed-magnon should enable joint excitation of an odd number of qubits. Considering the paramount importance of generating such 3-qubit GHZ states [25] for Shor's error correction code [22], we consider 3 qubits coupled to the same squeezed-magnon eigenmode:

$$\tilde{H}_3 = \tilde{H}_{\rm F} + \sum_{n=1,2,3}\left(\tilde{H}^n_{\rm q} + \tilde{H}^n_{\rm int}\right), \tag{10}$$

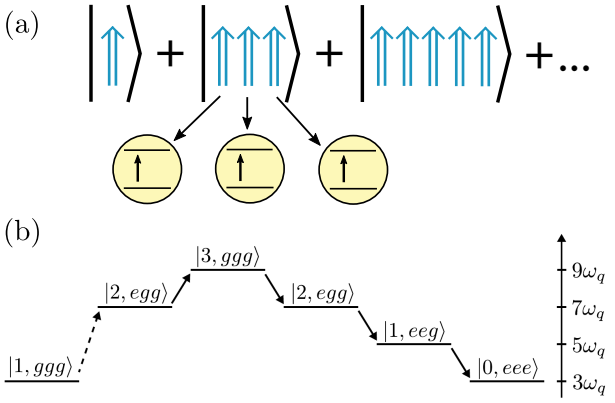

FIG. 2. Schematic depiction of the transition $|1,ggg\rangle \rightarrow |0,eee\rangle$. (a) The squeezed-magnon is comprised of a superposition of odd magnon-number states. This composite nature enables its absorption by an odd number of qubits. We focus on the case of 3. (b) An example pathway that takes the system from bearing 1 squeezed-magnon and 3 ground-state qubits ($|1,ggg\rangle$) to 0 squeezed-magnon and 3 excited qubits ($|0,eee\rangle$) via a series of virtual states. The first transition is effected by a CRT and is indicated via a dashed arrow. The right scale indicates the state energy, assuming $\omega_0 = 3\omega_q$.

with individual contributions expressed via Eqs. (5), (8), and (9). For simplicity, we assume the three qubits and their coupling with the magnet to be identical. The qualitative physics is unaffected by asymmetries among the 3 qubits, which are detailed in the SM [38]. Henceforth, we analyze the problem in its eigenbasis employing methodology consistent with previous investigation of joint photon absorption [56].

We are interested in jointly exciting the three qubits using a single squeezed-magnon eigenmode: a transition denoted as $|1,ggg\rangle \rightarrow |0,eee\rangle$. To gain physical insight, we first analyze this transition within the perturbation-theory framework detailed in the SM [38, 57]. While the transition is not possible via a direct process [first order in the interaction Eq. (9)], it can be accomplished via a series of virtual states. As the transition requires an increase of the total excitation number by 2, at least one of the virtual processes should be effected via the CRTs, thus requiring nonzero squeezing r in our system. The shortest path to effect the transition consists of three virtual processes, but its amplitude is canceled exactly by a complementary path [38]. Hence, the lowest nonvanishing order for accomplishing this transition is five with an example pathway depicted in Fig. 2(b) [58]. As detailed in the SM [38], several such paths contribute to the overall transition amplitude. The energy conservation requirement on the initial and final states necessitates $\omega_0 \approx 3\omega_q$.

Guided by intuition from the perturbative analysis, we now study the system [Eq. (10)] numerically using the

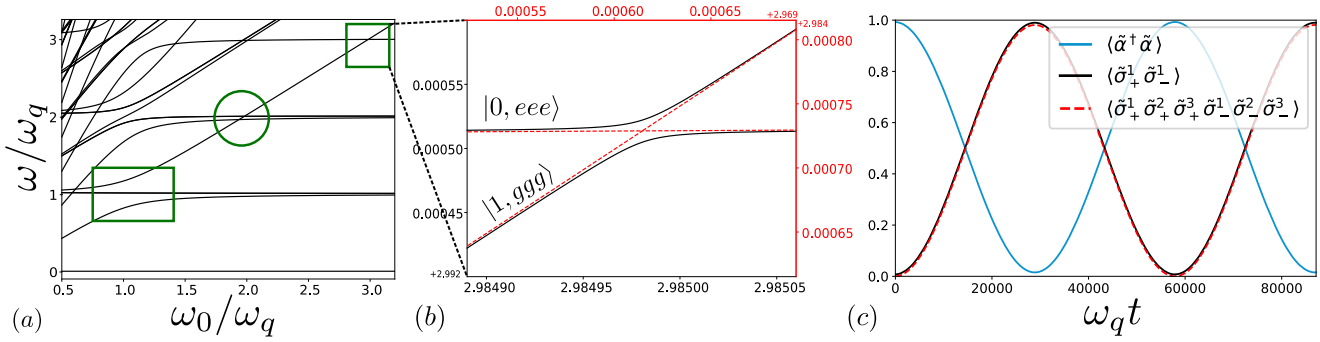

FIG. 3. Numerically evaluated spectrum and dynamics of 3 qubits coupled to 1 magnonic mode [Eq. (10)]. (a) Energy spectrum evaluated assuming $g_R = g_{CR} = 0.1\omega_q$. The green rectangle encloses the typical one-excitation anticrossing ($\omega_0 \approx \omega_q$). The circle highlights crossings around $\omega_0 \approx 2\omega_q$ as only odd number of qubits can be excited [Fig. 2(a)]. The square emphasizes the weaker three-excitation anticrossing around $\omega_0 \approx 3\omega_q$ that results from finite squeezing and the resulting CRTs. (b) A zoom-in on the three-excitation anticrossing that stems from the transition depicted in Fig. 2. The red dashed lines depict the spectrum evaluated assuming $g_{CR} = 0$ leaving the rest unchanged. (c) Zero-detuning system dynamics around $\omega_0 \approx 3\omega_q$ with the initial state $|1, ggg\rangle$. The squeezed-magnon occupation (blue solid) and single-qubit excitation (black solid) manifest the typical Rabi oscillations. A nearly perfect overlap between single-qubit and three-qubit (red dashed) correlations confirms the joint nature of the three-qubit excitation in these Rabi oscillations.

QuTiP package [59, 60]. Unless stated otherwise, we employ $g_R = g_{CR} = 0.1\omega_q$ in our analysis. A numerical diagonalization of the total Hamiltonian Eq. (10) yields the energy spectrum as depicted in Fig. 3(a). For zero qubit-magnon coupling, the spectrum should contain 8 (2^3) flat curves corresponding to the different excited qubits and zero squeezed-magnon occupation. Two triplets of these overlap resulting in 4 visually-distinct flat curves. The same 3-qubit spectrum combined with N squeezed-magnons yields the same 4 visually-distinct curves, now with a slope of N. For small but finite coupling considered in Fig. 3(a), we see the typical one-excitation Rabi splitting around $\omega_0 \approx \omega_q$ that results from a direct process. Around $\omega_0 \approx 2\omega_q$, we see crossings between different levels [61]. A coupling here is forbidden as only odd number of qubits can be excited by one squeezed-magnon [Fig. 2(a)]. An apparent crossing around $\omega_0 \approx 3\omega_q$ is in fact an anticrossing manifesting a small Rabi splitting between the states $|1, ggg\rangle$ and $|0, eee\rangle$ [see Fig. 3(b)]. This is the transition of our interest and the effective coupling responsible for it can be expressed as:

$$\tilde{H}_{\text{eff}} = g_{\text{eff}} \left(|1, ggg\rangle \langle 0, eee| + |0, eee\rangle \langle 1, ggg| \right), \qquad (11)$$

where $g_{\text{eff}}/\omega_q = 0.0001(g_{CR}/\omega_q) - 0.003(g_{CR}/\omega_q)^3$ has been obtained by fitting (perfectly) its g_{CR} dependence predicted by the perturbative analysis [38] to the Rabi splittings obtained via numerical diagonalization [62]. A comparison between squeezed-magnon occupation, single-qubit excitation, and three-qubit correlations plotted in Fig. 3(c) for Rabi oscillations around $\omega_0 \approx 3\omega_q$ confirms the joint nature of the three-qubit excitation.

Discussion.—Our system enables the transition $|1, ggg\rangle \rightarrow |0, eee\rangle$ with an effective coupling strength g_{eff} [Eq. (11)], or equivalently Rabi frequency, tunable via the magnon-squeezing: $g_{CR} = g \sinh r$. Bringing the system in resonance to enable Rabi oscillation for a fraction of the cycle can be exploited in generating 3-qubit GHZ and related entangled states: $(|ggg\rangle \pm |eee\rangle)/\sqrt{2}$. A convenient generation of these is central to Shor's error correction code [22] and thus, of great value in achieving fault tolerant quantum computing. Generating such 3-qubit entangled states using a series of two-qubit gate operations inevitably suffers from the challenge of synchronizing exact pulses, qubit asymmetries, decoherence and so on. In contrast, capitalizing on energy conservation, our proposed method is robust against any qubit asymmetries and perfectly synchronizes excitation of the 3 qubits.

Being a fifth-order process, g_{eff} was evaluated to be small for the parameters employed in our analysis above ($g_R = g_{CR} = 0.1\omega_q$). However, notwithstanding our choice of parameters motivated by a comparison with perturbation theory, the proposed system can achieve very high bare couplings g [Eq. (9)] ($g_R, g_{CR} > \omega_q$), such that the higher-order processes are not diminished and g_{eff} becomes large. Spin pumping experiments yield interfacial exchange couplings [Eq. (3)] of $J_{\text{int}} \approx 10$ meV between various (insulating) magnets and adjacent metals [63–65]. Assuming the qubit wavefunction to be localized in 5 monolayers below the equally thin ferromagnet and an interface comprised of 100 sites, we obtain the bare coupling rate [Eq. (4)] $g \approx 0.005 J_{\text{int}} \approx 80$ GHz, significantly larger than typical spin qubit and uniform magnon mode frequencies.

Our proposal of leveraging the intrinsic magnon-squeezing in generating entanglement via a coherent pro-

cess is complementary to previous incoherent interaction-based proposals [32, 44, 66, 67]. The latter typically necessitate diabatic decoupling of qubits from the magnet after achieving an entangled state. Our proposal thus uncovers an unexplored and experimentally-favorable avenue for exploiting the squeezing intrinsic to magnets.

Summary.—We have demonstrated the magnon|spin qubit ensemble to realize the anisotropic quantum Rabi model with coupling strengths feasible in the deep-strong regime. This system is shown to capitalize on various unique features of squeezed-magnons hosted by magnets. These include squeezing-mediated coupling enhancement, tunable anisotropy of the Rabi model, and a convenient synchronous entanglement of 3 qubits. Thus, the magnon|spin qubit ensemble provides a promising platform for investigating phenomena beyond the ultrastrong regime and implementing error correction codes.

We thank Wolfgang Belzig, Tim Ludwig, and Rembert Duine for valuable discussions. We acknowledge financial support from the Research Council of Norway through its Centers of Excellence funding scheme, project 262633, "QuSpin", and the Spanish Ministry for Science and Innovation – AEI Grant CEX2018-000805-M (through the "Maria de Maeztu" Programme for Units of Excellence in R&D).

* akashdeep.kamra@uam.es

[1] I. I. Rabi, "On the process of space quantization," Phys. Rev. **49**, 324–328 (1936).
[2] I. I. Rabi, "Space quantization in a gyrating magnetic field," Phys. Rev. **51**, 652–654 (1937).
[3] D. Braak, "Integrability of the rabi model," Phys. Rev. Lett. **107**, 100401 (2011).
[4] Qiong-Tao Xie, Shuai Cui, Jun-Peng Cao, Luigi Amico, and Heng Fan, "Anisotropic rabi model," Phys. Rev. X **4**, 021046 (2014).
[5] Qiongtao Xie, Honghua Zhong, Murray T Batchelor, and Chaohong Lee, "The quantum rabi model: solution and dynamics," Journal of Physics A: Mathematical and Theoretical **50**, 113001 (2017).
[6] Stephanie Wehner, David Elkouss, and Ronald Hanson, "Quantum internet: A vision for the road ahead," Science **362** (2018), 10.1126/science.aam9288.
[7] Masaya Fukami, Denis R. Candido, David D. Awschalom, and Michael E. Flatté, "Opportunities for long-range magnon-mediated entanglement of spin qubits via on- and off-resonant coupling," (2021), arXiv:2101.09220 [quant-ph].
[8] D. D. Awschalom, C. H. R. Du, R. He, F. J. Heremans, A. Hoffmann, J. T. Hou, H. Kurebayashi, Y. Li, L. Liu, V. Novosad, J. Sklenar, S. E. Sullivan, D. Sun, H. Tang, V. Tiberkevich, C. Trevillian, A. W. Tsen, L. R. Weiss, W. Zhang, X. Zhang, L. Zhao, and C. W. Zollitsch, "Quantum engineering with hybrid magnonics systems and materials," (2021), arXiv:2102.03222 [cond-mat.mes-hall].
[9] Guido Burkard, Michael J. Gullans, Xiao Mi, and Jason R. Petta, "Superconductor–semiconductor hybrid-circuit quantum electrodynamics," Nat. Rev. Phys. **2**, 129–140 (2020), 1905.01155.
[10] Arne Laucht, Frank Hohls, Niels Ubbelohde, M Fernando Gonzalez-Zalba, David J Reilly, Sren Stobbe, Tim Schrder, Pasquale Scarlino, Jonne V Koski, Andrew Dzurak, Chih-Hwan Yang, Jun Yoneda, Ferdinand Kuemmeth, Hendrik Bluhm, Jarryd Pla, Charles Hill, Joe Salfi, Akira Oiwa, Juha T Muhonen, Ewold Verhagen, M D LaHaye, Hyun Ho Kim, Adam W Tsen, Dimitrie Culcer, Attila Geresdi, Jan A Mol, Varun Mohan, Prashant K Jain, and Jonathan Baugh, "Roadmap on quantum nanotechnologies," Nanotechnology **32**, 162003 (2021), 2101.07882.
[11] C. Gerry and P. Knight, *Introductory Quantum Optics* (Cambridge University Press, 2004).
[12] D. F. Walls, "Squeezed states of light," Nature **306**, 141 (1983).
[13] Wei Qin, Adam Miranowicz, Peng-Bo Li, Xin-You Lü, J. Q. You, and Franco Nori, "Exponentially enhanced light-matter interaction, cooperativities, and steady-state entanglement using parametric amplification," Phys. Rev. Lett. **120**, 093601 (2018).
[14] C. Leroux, L. C. G. Govia, and A. A. Clerk, "Enhancing cavity quantum electrodynamics via antisqueezing: Synthetic ultrastrong coupling," Phys. Rev. Lett. **120**, 093602 (2018).
[15] Gangcheng Wang, Ruoqi Xiao, H. Z. Shen, Chunfang Sun, and Kang Xue, "Simulating anisotropic quantum rabi model via frequency modulation," Scientific Reports **9**, 4569 (2019).
[16] Carlos Sánchez Muñoz, Anton Frisk Kockum, Adam Miranowicz, and Franco Nori, "Simulating ultrastrong-coupling processes breaking parity conservation in jaynes-cummings systems," Phys. Rev. A **102**, 033716 (2020).
[17] Maximilian Russ and Guido Burkard, "Three-electron spin qubits," Journal of Physics: Condensed Matter **29**, 393001 (2017).
[18] Anasua Chatterjee, Paul Stevenson, Silvano De Franceschi, Andrea Morello, Nathalie P. de Leon, and Ferdinand Kuemmeth, "Semiconductor qubits in practice," Nature Reviews Physics **3**, 157–177 (2021), 2005.06564.
[19] Lieven M. K. Vandersypen and Mark A. Eriksson, "Quantum computing with semiconductor spins," Physics Today **72**, 38–45 (2019).
[20] Dany Lachance-Quirion, Yutaka Tabuchi, Arnaud Gloppe, Koji Usami, and Yasunobu Nakamura, "Hybrid quantum systems based on magnonics," Applied Physics Express **12**, 070101 (2019).
[21] Chetan Nayak, Steven H. Simon, Ady Stern, Michael Freedman, and Sankar Das Sarma, "Non-abelian anyons and topological quantum computation," Rev. Mod. Phys. **80**, 1083–1159 (2008).
[22] Peter W. Shor, "Scheme for reducing decoherence in quantum computer memory," Phys. Rev. A **52**, R2493–R2496 (1995).
[23] B M Terhal, J Conrad, and C Vuillot, "Towards scalable bosonic quantum error correction," Quantum Science and Technology **5**, 043001 (2020).
[24] Daniel Gottesman, Alexei Kitaev, and John Preskill, "Encoding a qubit in an oscillator," Physical Review A **64**, 012310 (2001).

[25] Daniel M. Greenberger, Michael A. Horne, and Anton Zeilinger, "Going beyond bell's theorem," (2007), arXiv:0712.0921 [quant-ph].

[26] Takao Aoki, Go Takahashi, Tadashi Kajiya, Jun-ichi Yoshikawa, Samuel L. Braunstein, Peter van Loock, and Akira Furusawa, "Quantum error correction beyond qubits," Nature Physics **5**, 541 (2009).

[27] Roman Schnabel, "Squeezed states of light and their applications in laser interferometers," Physics Reports **684**, 1 – 51 (2017).

[28] Z. Y. Ou, S. F. Pereira, H. J. Kimble, and K. C. Peng, "Realization of the einstein-podolsky-rosen paradox for continuous variables," Phys. Rev. Lett. **68**, 3663–3666 (1992).

[29] G. J. Milburn and Samuel L. Braunstein, "Quantum teleportation with squeezed vacuum states," Phys. Rev. A **60**, 937–942 (1999).

[30] Akashdeep Kamra and Wolfgang Belzig, "Superpoissonian shot noise of squeezed-magnon mediated spin transport," Phys. Rev. Lett. **116**, 146601 (2016).

[31] Akashdeep Kamra, Wolfgang Belzig, and Arne Brataas, "Magnon-squeezing as a niche of quantum magnonics," Applied Physics Letters **117**, 090501 (2020).

[32] Ji Zou, Se Kwon Kim, and Yaroslav Tserkovnyak, "Tuning entanglement by squeezing magnons in anisotropic magnets," Phys. Rev. B **101**, 014416 (2020).

[33] Sanchar Sharma, Victor A. S. V. Bittencourt, Alexy D. Karenowska, and Silvia Viola Kusminskiy, "Spin cat states in ferromagnetic insulators," Phys. Rev. B **103**, L100403 (2021).

[34] Yi-Pu Wang and Can-Ming Hu, "Dissipative couplings in cavity magnonics," Journal of Applied Physics **127**, 130901 (2020).

[35] Yutaka Tabuchi, Seiichiro Ishino, Atsushi Noguchi, Toyofumi Ishikawa, Rekishu Yamazaki, Koji Usami, and Yasunobu Nakamura, "Coherent coupling between a ferromagnetic magnon and a superconducting qubit," Science **349**, 405–408 (2015).

[36] Daniel Loss and David P. DiVincenzo, "Quantum computation with quantum dots," Phys. Rev. A **57**, 120–126 (1998).

[37] A.I. Akhiezer, V.G. Bar'iakhtar, and S.V. Peletminski, *Spin waves* (North-Holland Publishing Company, Amsterdam, 1968).

[38] See Supplemental Material for (i) a detailed derivation of the system Hamiltonian and (ii) a detailed perturbation-theory based analysis of the simultaneous three-qubit excitation including the various third-order and fifth-order virtual processes as well as the resilience of the phenomena against qubit-asymmetries.

[39] T. Holstein and H. Primakoff, "Field dependence of the intrinsic domain magnetization of a ferromagnet," Phys. Rev. **58**, 1098–1113 (1940).

[40] Daniel D. Stancil and Anil Prabhakar, *Spin Waves: Theory and Applications* (Springer US, 2009).

[41] S Takahashi, E Saitoh, and S Maekawa, "Spin current through a normal-metal/insulating-ferromagnet junction," Journal of Physics: Conference Series **200**, 062030 (2010).

[42] Scott A. Bender and Yaroslav Tserkovnyak, "Interfacial spin and heat transfer between metals and magnetic insulators," Phys. Rev. B **91**, 140402 (2015).

[43] Akashdeep Kamra and Wolfgang Belzig, "Magnon-mediated spin current noise in ferromagnet | nonmagnetic conductor hybrids," Phys. Rev. B **94**, 014419 (2016).

[44] Luka Trifunovic, Fabio L. Pedrocchi, and Daniel Loss, "Long-distance entanglement of spin qubits via ferromagnet," Phys. Rev. X **3**, 041023 (2013).

[45] B. Flebus and Y. Tserkovnyak, "Quantum-impurity relaxometry of magnetization dynamics," Phys. Rev. Lett. **121**, 187204 (2018).

[46] Chunhui Du, Toeno van der Sar, Tony X. Zhou, Pramey Upadhyaya, Francesco Casola, Huiliang Zhang, Mehmet C. Onbasli, Caroline A. Ross, Ronald L. Walsworth, Yaroslav Tserkovnyak, and Amir Yacoby, "Control and local measurement of the spin chemical potential in a magnetic insulator," Science **357**, 195–198 (2017).

[47] Anton Frisk Kockum, Adam Miranowicz, Vincenzo Macrì, Salvatore Savasta, and Franco Nori, "Deterministic quantum nonlinear optics with single atoms and virtual photons," Phys. Rev. A **95**, 063849 (2017).

[48] J. Casanova, G. Romero, I. Lizuain, J. J. García-Ripoll, and E. Solano, "Deep strong coupling regime of the jaynes-cummings model," Phys. Rev. Lett. **105**, 263603 (2010).

[49] T. Niemczyk, F. Deppe, H. Huebl, E. P. Menzel, F. Hocke, M. J. Schwarz, J. J. Garcia-Ripoll, D. Zueco, T. Hümmer, E. Solano, A. Marx, and R. Gross, "Circuit quantum electrodynamics in the ultrastrong-coupling regime," Nature Physics **6**, 772 (2010).

[50] P. Forn-Díaz, L. Lamata, E. Rico, J. Kono, and E. Solano, "Ultrastrong coupling regimes of light-matter interaction," Rev. Mod. Phys. **91**, 025005 (2019).

[51] S. Ashhab and Franco Nori, "Qubit-oscillator systems in the ultrastrong-coupling regime and their potential for preparing nonclassical states," Phys. Rev. A **81**, 042311 (2010).

[52] The ground state stability ensures $\omega_0 > 0$ and $(A+\omega_0)^2 > 4B^2$.

[53] Michael Martin Nieto, "Displaced and squeezed number states," Physics Letters A **229**, 135 – 143 (1997).

[54] P. Král, "Displaced and squeezed fock states," Journal of Modern Optics **37**, 889–917 (1990).

[55] The magnetocrystalline anisotropies can be tuned via strain, for example.

[56] Luigi Garziano, Vincenzo Macrì, Roberto Stassi, Omar Di Stefano, Franco Nori, and Salvatore Savasta, "One Photon Can Simultaneously Excite Two or More Atoms," Phys. Rev. Lett. **117**, 043601 (2016).

[57] W. R. Salzman, "Diagrammatical Derivation and Representation of Rayleigh–Schrödinger Perturbation Theory," The Journal of Chemical Physics **49**, 3035–3040 (1968).

[58] Since this path involves 4 rotating and 1 counter-rotating processes, its amplitude scales as $\sim g_{CR} g_R^4$.

[59] J.R. Johansson, P.D. Nation, and Franco Nori, "Qutip: An open-source python framework for the dynamics of open quantum systems," Computer Physics Communications **183**, 1760–1772 (2012).

[60] J.R. Johansson, P.D. Nation, and Franco Nori, "Qutip 2: A python framework for the dynamics of open quantum systems," Computer Physics Communications **184**, 1234–1240 (2013).

[61] The nature "crossing", as opposed to anticrossing, of these intersections has been verified carefully by evaluating the energy spectra around them with a very high precision.

[62] The reported g_{eff} has been obtained for $g_R = 0.1\omega_q$.

[63] Y. Kajiwara, K. Harii, S. Takahashi, J. Ohe, K. Uchida, M. Mizuguchi, H. Umezawa, H. Kawai, K. Ando, K. Takanashi, S. Maekawa, and E. Saitoh, "Transmission of electrical signals by spin-wave interconversion in a magnetic insulator," Nature **464**, 262–266 (2010).

[64] F. D. Czeschka, L. Dreher, M. S. Brandt, M. Weiler, M. Althammer, I.-M. Imort, G. Reiss, A. Thomas, W. Schoch, W. Limmer, H. Huebl, R. Gross, and S. T. B. Goennenwein, "Scaling behavior of the spin pumping effect in ferromagnet-platinum bilayers," Phys. Rev. Lett. **107**, 046601 (2011).

[65] Mathias Weiler, Matthias Althammer, Michael Schreier, Johannes Lotze, Matthias Pernpeintner, Sibylle Meyer, Hans Huebl, Rudolf Gross, Akashdeep Kamra, Jiang Xiao, Yan-Ting Chen, HuJun Jiao, Gerrit E. W. Bauer, and Sebastian T. B. Goennenwein, "Experimental test of the spin mixing interface conductivity concept," Phys. Rev. Lett. **111**, 176601 (2013).

[66] Akashdeep Kamra, Even Thingstad, Gianluca Rastelli, Rembert A. Duine, Arne Brataas, Wolfgang Belzig, and Asle Sudbø, "Antiferromagnetic magnons as highly squeezed fock states underlying quantum correlations," Phys. Rev. B **100**, 174407 (2019).

[67] H. Y. Yuan, Akashdeep Kamra, Dion M. F. Hartmann, and Rembert A. Duine, "Electrically switchable entanglement channel in van der waals magnets," (2021), arXiv:2103.15899 [cond-mat.mes-hall].

B

Supplemental Material accompanying the manuscript "Tunable anisotropic quantum Rabi model via magnon|spin-qubit ensemble"

Ida C. Skogvoll, Jonas Lidal, and Jeroen Danon
Center for Quantum Spintronics, Department of Physics,
Norwegian University of Science and Technology, NO-7491 Trondheim, Norway

Akashdeep Kamra*
Condensed Matter Physics Center (IFIMAC) and
Departamento de Física Teórica de la Materia Condensada,
Universidad Autónoma de Madrid, E-28049 Madrid, Spain and
Center for Quantum Spintronics, Department of Physics,
Norwegian University of Science and Technology, NO-7491 Trondheim, Norway

SYSTEM HAMILTONIAN

In this section, we derive the Hamiltonian describing our magnon/spin-qubit ensemble. First, starting with the ferromagnetic spin Hamiltonian, we obtain the description of the magnonic mode. Then, we specify the spin-qubit. Finally, we derive the interfacial exchange-mediated interaction between the two subsystems.

Magnonic mode

Taking into account Zeeman energy, ferromagnetic exchange, and a general anisotropy, the ferromagnet is described via the spin Hamiltonian:

$$\tilde{H}_{\mathrm{F}} = |\gamma|\mu_0 H_0 \sum_i \tilde{S}_{iz} - J \sum_{\langle i,j \rangle} \tilde{\boldsymbol{S}}_i \cdot \tilde{\boldsymbol{S}}_j + \sum_i \left[K_x \left(\tilde{S}_{ix} \right)^2 + K_y \left(\tilde{S}_{iy} \right)^2 + K_z \left(\tilde{S}_{iz} \right)^2 \right], \quad \text{(S1)}$$

where the applied magnetic field is $H_0 \hat{\boldsymbol{z}}$, γ (< 0) is the gyromagnetic ratio, J (> 0) is the exchange energy, $\langle i, j \rangle$ denotes sum over nearest neighbors, and $K_{x,y,z}$ parameterize the magnetic anisotropy. While the anisotropy may arise due to dipolar interactions or magnetocrystalline single-ion anisotropies, our assumed general form encompasses all such symmetry-allowed contributions that can contribute to determining the uniform $\boldsymbol{k} = \boldsymbol{0}$ magnon mode [1].

Assuming the Zeeman energy to dominate over anisotropy, we consider all spins to point along $-\hat{\boldsymbol{z}}$ in the magnetic ground state. We may express the spin Hamiltonian Eq. (S1) in terms of bosonic magnons via the Holstein-Primakoff transformation [2] corresponding to our spin ground state:

$$\tilde{S}_{j+} = \sqrt{2S}\ \tilde{a}_j^\dagger, \quad \text{(S2)}$$

$$\tilde{S}_{j-} = \sqrt{2S}\ \tilde{a}_j, \quad \text{(S3)}$$

$$\tilde{S}_{jz} = -S + \tilde{a}_j^\dagger \tilde{a}_j, \quad \text{(S4)}$$

where $\tilde{S}_{j\pm} \equiv \tilde{S}_{jx} \pm i\tilde{S}_{jy}$, $\tilde{a}_j$ is the magnon annihilation operator at position j, and S is the spin magnitude. In addition, we need the Fourier relations:

$$\tilde{a}_j = \frac{1}{\sqrt{N_F}} \sum_{\boldsymbol{k}} \tilde{a}_{\boldsymbol{k}}\ e^{-i\boldsymbol{k}\cdot\boldsymbol{r}_j}, \quad \text{(S5)}$$

$$\tilde{a}_{\boldsymbol{k}} = \frac{1}{\sqrt{N_F}} \sum_j \tilde{a}_j\ e^{i\boldsymbol{k}\cdot\boldsymbol{r}_j}, \quad \text{(S6)}$$

where N_F is the total number of sites in the ferromagnet and $\tilde{a}_{\boldsymbol{k}}$ is the annihilation operator for the magnon mode with wavevector $\boldsymbol{k}$. Employing these Holstein-Primakoff and Fourier transformations in Eq. (S1), we obtain the magnonic Hamiltonian:

$$\tilde{H}_{\mathrm{F}} = \text{const.} + \sum_{\boldsymbol{k}} \left[A_{\boldsymbol{k}} \tilde{a}^{\dagger}_{\boldsymbol{k}} \tilde{a}_{\boldsymbol{k}} + B_{\boldsymbol{k}} \left(\tilde{a}^{\dagger}_{\boldsymbol{k}} \tilde{a}^{\dagger}_{-\boldsymbol{k}} + \tilde{a}_{\boldsymbol{k}} \tilde{a}_{-\boldsymbol{k}} \right) \right], \tag{S7}$$

with $A_{\boldsymbol{k}} \equiv |\gamma| \mu_0 H_0 + K_x S + K_y S - 2K_z S + 4JS \left[3 - (\cos k_x a + \cos k_y a + \cos k_z a) \right]$ and $B_{\boldsymbol{k}} \equiv S(K_x - K_y)/2$. In obtaining the exchange contribution to $A_{\boldsymbol{k}}$, we have assumed a simple cubic lattice with lattice constant a. In the long wavelength limit i.e., $ak_{x,y,z} \ll 1$, the cosines can be approximated by parabolas.

As discussed in the main text, we retain only the uniform mode corresponding to $\boldsymbol{k} = \boldsymbol{0}$ in our consideration of the magnon/spin-qubit system. This is justifiable because for small dimensions of the magnet considered herein, the allowed wavevectors $\boldsymbol{k}$ correspond to magnon energies separated from the lowest uniform mode (with an energy of a few GHz) by at least several GHz. Thus, we may disregard such high-energy modes when considering coherent resonant interactions, as we do in this work. Further diagonalization of Eq. (S7), considering only the uniform mode, via Bogoliubov transformation has been described in the main text.

Spin-qubit

We consider our spin-qubit to be comprised by a confined electronic orbital that admits spin-up and -down states. Considering a lifting of the spin-degeneracy by, for example, an applied magnetic field, the spin-qubit Hamiltoniam may be expressed as:

$$\tilde{H}_{\mathrm{q}} = \text{const.} + \frac{\omega_q}{2} \left(\tilde{c}^{\dagger}_{\uparrow} \tilde{c}_{\uparrow} - \tilde{c}^{\dagger}_{\downarrow} \tilde{c}_{\downarrow} \right), \tag{S8}$$

where, considering a negative gyromagnetic ratio and applied magnetic field along $\hat{\boldsymbol{z}}$, ω_q (> 0) is the qubit splitting. We further introduce the notation:

$$\tilde{\sigma}_z \equiv \begin{pmatrix} \tilde{c}^{\dagger}_{\uparrow} & \tilde{c}^{\dagger}_{\downarrow} \end{pmatrix} \begin{pmatrix} 1 & 0 \\ 0 & -1 \end{pmatrix} \begin{pmatrix} \tilde{c}_{\uparrow} \\ \tilde{c}_{\downarrow} \end{pmatrix} \equiv \underline{\tilde{c}}^{\dagger} \, \underline{\sigma}_z \, \underline{\tilde{c}}, \tag{S9}$$

where an underline identifies a matrix. With this notation and dropping the spin-independent constant, the spin-qubit Hamiltonian is expressed as:

$$\tilde{H}_{\mathrm{q}} = \frac{\omega_q}{2} \tilde{\sigma}_z. \tag{S10}$$

With the notation defined by Eq. (S9), $\tilde{\sigma}_+ \equiv (\tilde{\sigma}_x + i\tilde{\sigma}_y)/2$ becomes the qubit excitation operator, while $\tilde{\sigma}_- \equiv (\tilde{\sigma}_x - i\tilde{\sigma}_y)/2$ is the qubit relaxation operator.

Exchange coupling

The magnon/spin-qubit are considered to be coupled via interfacial exchange interaction parameterized via J_{int} [1, 3, 4]:

$$\tilde{H}_{\text{int}} = J_{\text{int}} \sum_l \tilde{\boldsymbol{S}}_l \cdot \tilde{\boldsymbol{s}}_l, \tag{S11}$$

where l labels the interfacial sites, $\tilde{\boldsymbol{S}}$ denotes the ferromagnetic spin operator, and $\tilde{\boldsymbol{s}}$ represents the spin of the electronic states that comprise the qubit. We wish to express the interfacial Hamiltonian Eq. (S11) in terms of the magnon and qubit operators. To this end, $\tilde{\boldsymbol{S}}_l$ can be expressed via magnon operators using the Holstein-Primakoff and Fourier transforms [Eqs.(S2) - (S6)] already described above. We now discuss the representation of $\tilde{\boldsymbol{s}}_l$ in terms of the qubit operators $\tilde{\sigma}_{x,y,z}$ [Eq. (S9)].

Following quantum field theory notation for discrete sites, the spin operator at a given position $\boldsymbol{r}$ can be expressed in terms of ladder operators at the same position:

$$\tilde{\boldsymbol{s}}(\boldsymbol{r}) = \frac{1}{2} \sum_{s,s\prime=\uparrow,\downarrow} \tilde{\Psi}_s^\dagger(\boldsymbol{r}) \boldsymbol{\sigma}_{ss'} \tilde{\Psi}_{s'}(\boldsymbol{r}), \tag{S12}$$

where $\underline{\boldsymbol{\sigma}} = \underline{\sigma}_x \hat{\boldsymbol{x}} + \underline{\sigma}_y \hat{\boldsymbol{y}} + \underline{\sigma}_z \hat{\boldsymbol{z}}$ with $\underline{\sigma}_{x,y,z}$ the Pauli matrices. The local ladder operators can further be represented in terms of the complete set of eigenstates labeled via orbital index t:

$$\tilde{\Psi}_s(\boldsymbol{r}) = \sum_t \psi_t(\boldsymbol{r}) \tilde{c}_{ts}, \tag{S13}$$

where $\psi(\boldsymbol{r})$ is the spatial wavefunction of the different orbitals and $\tilde{c}_{ts}$ are the ladder operators for each spin-resolved orbital. Employing this relation, Eq. (S12) becomes:

$$\tilde{\boldsymbol{s}}(\boldsymbol{r}) = \frac{1}{2} \sum_{s,s\prime,t,t'} \psi_t^*(\boldsymbol{r}) \psi_{t'}(\boldsymbol{r}) \boldsymbol{\sigma}_{ss'} \tilde{c}_{ts}^\dagger \tilde{c}_{t's'}. \tag{S14}$$

Since for our spin-qubit we are interested in only one of the complete set of orbitals, we allow only 1 value of t and thus drop the index t in consistence with our previous considerations

Eq. (S8):

$$\tilde{\boldsymbol{s}}(\boldsymbol{r}) = \frac{1}{2}\sum_{s,s\prime} |\psi(\boldsymbol{r})|^2 \boldsymbol{\sigma}_{ss'} \tilde{c}_s^\dagger \tilde{c}_{s'}, \tag{S15}$$

$$= \frac{|\psi(\boldsymbol{r})|^2}{2}\ \underline{\tilde{c}}^\dagger\ \underline{\boldsymbol{\sigma}}\ \underline{\tilde{c}}, \tag{S16}$$

$$\implies \tilde{\boldsymbol{s}}_l = \frac{|\psi_l|^2}{2}\ \underline{\tilde{c}}^\dagger\ \underline{\boldsymbol{\sigma}}\ \underline{\tilde{c}}, \tag{S17}$$

where ψ_l is the wavefunction amplitude of the qubit orbital at position l.

The interfacial interaction Eq. (S11) is now simplified as:

$$\tilde{H}_{\text{int}} = J_{\text{int}} \sum_l \left[\tilde{S}_{lz}\tilde{s}_{lz} + \frac{1}{2}\left(\tilde{S}_{l+}\tilde{s}_{l-} + \tilde{S}_{l-}\tilde{s}_{l+} \right) \right], \tag{S18}$$

where $\tilde{S}_{l\pm} \equiv \tilde{S}_{lx} \pm i\tilde{S}_{ly}$ and $\tilde{s}_{l\pm} \equiv \tilde{s}_{lx} \pm i\tilde{s}_{ly}$. Employing Eq. (S17) together with Eqs.(S2) - (S6) and retaining only the uniform magnon mode, the interfacial Hamiltonian is simplified to include two contributions:

$$\tilde{H}_{\text{int}} = \tilde{H}_{\text{int1}} + \tilde{H}_{\text{int2}}. \tag{S19}$$

The first contribution is our desired magnon/spin-qubit exchange coupling:

$$\tilde{H}_{\text{int1}} = J_{\text{int}} N_{\text{int}} |\psi|^2 \sqrt{\frac{S}{2N_F}} \left(\tilde{a}^\dagger \tilde{\sigma}_- + \tilde{a}\tilde{\sigma}_+ \right), \tag{S20}$$

where N_{int} is the number of interfacial sites and $|\psi|^2 \equiv \left(\sum_l |\psi_l|^2\right)/N_{\text{int}}$ is the qubit electronic state wavefunction averaged over the interface. The second contribution:

$$\tilde{H}_{\text{int2}} = -\frac{S J_{\text{int}} N_{\text{int}} |\psi|^2}{2}\ \tilde{\sigma}_z \tag{S21}$$

renormalizes the spin-qubit energy and can be absorbed into ω_q [Eq. (S10)].

DERIVING AN EXPRESSION FOR THE EFFECTIVE COUPLING WITH PERTURBATION THEORY

Here we look at the Hamiltonian describing 3 qubits coupled to the same squeezed-magnon eigenmode, as described in the main text. We assume the interaction terms, $\tilde{H}^n_{\text{int}}$, to be small compared to the rest of the Hamiltonian, $\tilde{H}_0 = \omega_0 \tilde{\alpha}^\dagger \tilde{\alpha} + \sum_{n=1,2,3} \frac{\omega_{qn}}{2} \tilde{\sigma}^n_z$, and calculate the effective coupling g_{eff} between the two states $|1, ggg\rangle$ and $|0, eee\rangle$ using perturbation theory. The interaction term, $\tilde{H}^n_{\text{int}}$, is given by:

$$\tilde{H}^n_{\text{int}} = g_{Rn} \left(\tilde{\alpha}^\dagger \tilde{\sigma}^n_- + \tilde{\alpha} \tilde{\sigma}^n_+ \right) + g_{CRn} \left(\tilde{\alpha}^\dagger \tilde{\sigma}^n_+ + \tilde{\alpha} \tilde{\sigma}^n_- \right). \tag{S22}$$

The relevant virtual processes will be shown as paths from $|1, ggg\rangle$ (blue) to $|0, eee\rangle$ (red) on a grid of "number of magnon excitations" and "number of qubit excitations". The rotating term (drawn as a full line) will keep the number of total excitations constant while the counter-rotating term (drawn as a dotted line) will change the total number of excitations by two. The detailed expressions for each diagram will be calculated using the diagrammatic approach from Ref. [5].

Third-order perturbation theory

We start by applying perturbation theory to third order. The two third-order diagrams are shown in Figure S1. For general qubits, these two diagrams result in the effective coupling:

$$g^{(3)}_{\text{eff}} = \sum_{\substack{i,j,k \\ i \neq j \neq k \neq i}} \left[\frac{2 g_{CRi} g_{Rj} g_{Rk}}{(-\omega_0 - \omega_{qi})(-\omega_{qi} - \omega_{qj})} + \frac{g_{Ri} g_{CRj} g_{Rk}}{(\omega_0 - \omega_{qi})(-\omega_{qi} - \omega_{qj})} \right], \tag{S23}$$

where the sum is over all qubit permutations.

If we assume that the qubits are identical ($g_{CRi} = g_{CR}, g_{Ri} = g_R, \omega_{qi} = \omega_q$), all qubit permutations are equivalent and the sum can be carried out by counting qubit permutations:

$$g^{(3)}_{\text{eff}} = 3 {g_R}^2 g_{CR} \frac{3\omega_q - \omega_0}{\omega_q \left({\omega_0}^2 - {\omega_q}^2 \right)}. \tag{S24}$$

As we can see, the two paths cancel at resonance, $\omega_0 = 3\omega_q$. Moreover, it can be shown from equation (S23) that the third-order term cancels when $\omega_0 = \sum_i \omega_{qi}$. The pure third-order perturbation theory result is therefore zero.

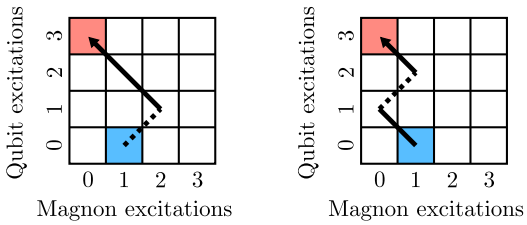

FIG. S1. Diagrams connecting $|1, ggg\rangle$ (blue) and $|0, eee\rangle$ (red) via virtual transitions to third order. Counter-rotating processes are represented by dashed lines.

Fifth-order perturbation theory

Since the third-order result is zero and there are no fourth-order paths, we move on to fifth order by drawing all fifth-order paths from the initial state $|1, ggg\rangle$ (blue) to the state $|0, eee\rangle$ (red). We use the result that the third-order term cancels at resonance to note that pairs of diagrams like the ones in Figure S2, i.e. the two third-order diagrams with an additional loop on a shared vertex that is not the initial vertex, also fully cancel at resonance.

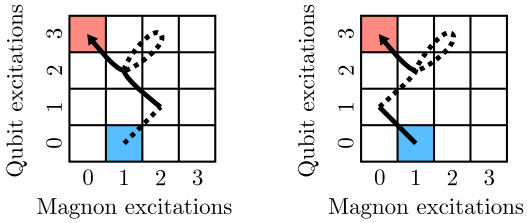

FIG. S2. Example of fifth-order diagrams which cancel if $\omega_0 = 3\omega_q$. Pairs of the two third-order diagrams with an additional loop on a shared vertex that is not the initial vertex fully cancel at resonance. Counter-rotating terms are represented by dashed lines.

All remaining diagrams are shown in Figure S3. Diagrams (a) and (c) cancel partially, but not fully and give the contribution:

$$g_{\text{eff}}^{(5a)} + g_{\text{eff}}^{(5c)} = \sum_{\substack{i,j,k,l \\ j\neq k\neq l\neq j}} \left[\left(\frac{2{g_{CRi}}^2}{(-\omega_0 - \omega_{qi})} \right) \left(\frac{2 g_{CRj} g_{Rk} g_{Rl}}{(-\omega_0 - \omega_{qi})^2 (-\omega_{qi} - \omega_{qj})} + \frac{g_{Rj} g_{CRk} g_{Rl}}{(\omega_0 - \omega_{qi})^2 (-\omega_{qi} - \omega_{qj})} \right) \right]. \tag{S25}$$

Similarly for (b) and (d):

$$g_{\text{eff}}^{(5b)}+g_{\text{eff}}^{(5d)} = \sum_{\substack{i,j,k,l \\ j\neq k\neq l\neq j}} \left[\left(\frac{{g_{Ri}}^2}{(\omega_0-\omega_{qi})}\right)\left(\frac{2g_{CRj}g_{Rk}g_{Rl}}{(-\omega_0-\omega_{qi})^2(-\omega_{qi}-\omega_{qj})}+\frac{g_{Rj}g_{CRk}g_{Rl}}{(\omega_0-\omega_{qi})^2(-\omega_{qi}-\omega_{qj})}\right)\right]. \tag{S26}$$

The contribution from diagram (e), (f) and (g):

$$g_{\text{eff}}^{(5e)} = \sum_{\substack{i,j,k,l \\ i\neq j\neq k\neq i}} \frac{6g_{CRi}g_{CRj}g_{Rk}g_{CRl}g_{Rl}}{(-\omega_0-\omega_{qi})(-2\omega_0-\omega_{qi}-\omega_{qj})(-\omega_0-\sum_n\omega_{qn})(\omega_{ql}-\sum_n\omega_{qn})}. \tag{S27}$$

$$g_{\text{eff}}^{(5f)} = \sum_{\substack{i,j,k,l,m,n \\ i\neq j\neq k\neq i \\ l=i,j \\ m=l,k \\ n\neq m \quad n=l,k}} \frac{6g_{CRi}g_{CRj}g_{CRl}g_{Rm}g_{Rn}}{(-\omega_0-\omega_{qi})(-2\omega_0-\omega_{qi}-\omega_{qj})(-\omega_0+\omega_{ql}+\omega_{qk}-\sum_p\omega_{qp})(\omega_{qn}-\sum_p\omega_{qp})}. \tag{S28}$$

$$g_{\text{eff}}^{(5g)} = \sum_{\substack{i,j,k,l \\ j\neq k\neq l\neq j}} \frac{6g_{CRi}g_{Ri}g_{Rj}g_{Rk}g_{Rl}}{(-\omega_0-\omega_{qi})(-2\omega_0)(-\omega_0-\omega_{qj})(-\omega_{qj}-\omega_{qk})}. \tag{S29}$$

If we now assume that we are at resonance and that the qubits are identical ($g_{CRi} = g_{CR}, g_{Ri} = g_R, \omega_{qi} = \omega_q$ and $\omega_0 = 3\omega_q$), the sums can again be carried out by counting qubit permutations. The total effective coupling to fifth order is then:

$$g_{\text{eff}}^{(5)} = -\frac{9\left(3{g_{CR}}^3{g_R}^2-8g_{CR}{g_R}^4\right)}{32{\omega_q}^4}. \tag{S30}$$

Additional corrections

As we have seen, the third-order contribution to the effective coupling is zero when $\omega_0 = 3\omega_q$. However, if we are interested in the details of the (anti-)crossing, there is an additional detail we need to consider. The perturbation causes the energy levels to shift, which causes the (anti-)crossing to take place a small shift away from $\omega_0 = 3\omega_q$.

By applying second order perturbation theory (at $\omega_0 = 3\omega_q$) to the energies of the two relevant states, we get that the crossing will take place at:

$$\omega_0 = 3\omega_q + \frac{3{g_{CR}}^2}{2\omega_q} - \frac{3{g_R}^2}{\omega_q}. \tag{S31}$$

Inserting this into the third-order effective coupling, Eq. (S24), and keeping terms of up to fifth order in $g_{CR/R}$, leaves us with: [6]

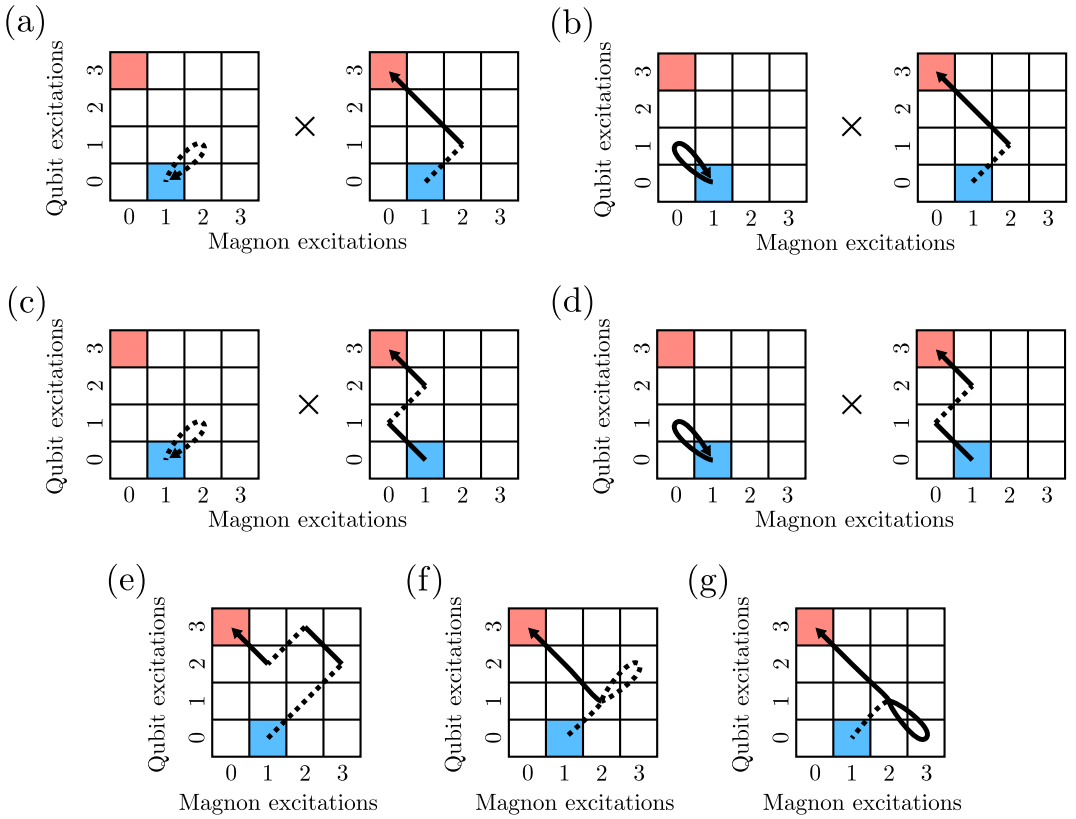

FIG. S3. Relevant diagrams that connect $|1, ggg\rangle$ (blue) and $|0, eee\rangle$ (red) via virtual transitions to fifth order. Counter-rotating terms are represented by dashed lines.

$$g_{\text{eff}}^{(3)\prime} = \frac{9\left({g_{CR}}^3 {g_R}^2 - 2 g_{CR} {g_R}^4\right)}{16 {\omega_q}^4}, \tag{S32}$$

where the prime indicates that the effective coupling is evaluated at the (anti-)crossing.

* akashdeep.kamra@uam.es

[1] Akashdeep Kamra and Wolfgang Belzig, "Magnon-mediated spin current noise in ferromagnet | nonmagnetic conductor hybrids," Phys. Rev. B **94**, 014419 (2016).

[2] T. Holstein and H. Primakoff, "Field dependence of the intrinsic domain magnetization of a ferromagnet," Phys. Rev. **58**, 1098–1113 (1940).

[3] S Takahashi, E Saitoh, and S Maekawa, "Spin current through a normal-metal/insulating-ferromagnet junction," Journal of Physics: Conference Series **200**, 062030 (2010).

[4] Scott A. Bender and Yaroslav Tserkovnyak, "Interfacial spin and heat transfer between metals and magnetic insulators," Phys. Rev. B **91**, 140402 (2015).

[5] W. R. Salzman, "Diagrammatical Derivation and Representation of Rayleigh–Schrödinger Perturbation Theory," The Journal of Chemical Physics **49**, 3035–3040 (1968).

[6] The effective coupling from Eq. (S30) and Eq. (S32) can be tuned to zero, both separately (at $g_{CR} = \pm\sqrt{\frac{8}{3}}g_R$ and $g_{CR} = \pm\sqrt{2}g_R$ respectively) as well as the sum of the two ($g_{CR} = \pm 2g_R$).

NTNU

Norwegian University of
Science and Technology